UNIVERSITAT POLITÈCNICA
DE CATALUNYA
BARCELONATECH

Influence of axial compression ratio in building columns

Sergio Villar Salinas

UNIVERSITAT POLITÈCNICA DE CATALUNYA
BARCELONATECH
Departament d'Enginyeria Civil i Ambiental

PROGRAMA DE DOCTORAT: Enginyeria Sísmica i Dinàmica Estructural

DOCTORAL THESIS

INFLUENCE OF AXIAL COMPRESSION RATIO IN BUILDING COLUMNS

Sergio Villar Salinas

DIRECTOR
Francesc López Almansa

Barcelona, December 2023

“A failed structure provides a counterexample to a hypothesis and shows us incontrovertibly what cannot be done, while a structure that stands without incident often conceals whatever lessons or caveats it might hold for the next generation of engineer”

Henry Petroski

Influence of axial compression ratio in building columns

Sergio Villar Salinas

To God, who has given me the most valued support every time I need it. My family, parents (Sergio and Mary Luz), siblings (Wilson and Melissa), wife (Natalie), and children (Sergio Elias, Elisa y Elena), and good friends.

CONTENTS

Acknowledgements

First, the author wants to express special thanks to his thesis supervisor, **Dr. Francesc López Almansa**, whose valuable guidance, support, patience, time, mentorship and encouragement, this thesis work would not have been accomplished. As well, the help of the following PhD holders is gratefully acknowledged. From whom, the author learned how to do research and fulfil scientific collaboration:

- Dr. Amit Kanvinde, for his gentleness, time for our discussions and reviews, patience, mentorship, for sharing raw data of some test results, and insightful comments into the study presented in chapter five.
- Dr. Julián Carrillo, for his friendly support during my PhD journey, time and detailed reviews of the work presented in chapter three.
- Dr. Carlos Graciano, for his scientific collaboration with the study shown in chapter four.
- Dr. Andrés Guzmán, for his kind help during the writing of the first draft of the research proposal, and encouragement along the way.

Thanks to the people who accompanied the author, offered their help in different ways on the road and offered their hands. This author gratitude to all friends, Sebastián Pacheco, Beny Zúñiga, Vinod Kumar and Carlos Mario Piscal.

The author greatly appreciates the financial support by Fundación Carolina and Universidad Tecnológica de Bolívar, during his PhD studies. Besides, the help of PCEM SAS with the drafting of some figures is thankfully acknowledged.

Last but foremost, the author wholeheartedly wishes to thank his parents, Sergio Villar Villa and Mary Luz Salinas Salas, brother Wilson, sister Melissa, wife Natalie Morales Londoño, and children Sergio Elías, Elisa and Elena, for their years of help and support.

Resumen

Las fuerzas internas axiales en columnas de pórticos-resistentes a momento (MRF, por sus siglas en inglés) tienen un rol fundamental en el desempeño sísmico de estos sistemas estructurales. No obstante, existen brechas significativas en la literatura relacionadas con la influencia de estas fuerzas en el desempeño sísmico de estos pórticos. Algunas de estas brechas son: (i) Existen columnas en edificios de concreto reforzado (RC, por sus siglas en inglés) diseñadas deficientemente, de tal forma que su demanda excede su capacidad, incluso para combinaciones de cargas gravitacionales de servicio; esta deficiencia normalmente conduce a una resistencia sísmica insuficiente. A pesar de esto, muchos códigos de diseño sísmico no especifican límites para la relación de fuerzas axiales (ACR, por sus siglas en inglés), (ii) Las filosofías de diseño existentes para el diseño de platinas de base expuestas (ECBP, por sus siglas en inglés), fallan en predecir de forma precisa los modos de falla de estas conexiones columnas-base; además, estas filosofías no consideran la interacción momento-carga axial para cada componente de dichas conexiones, (iii) Hacen falta modelos predictivos confiables para los parámetros de modelación de ECBP sometidas a momento y carga axial. Con el fin de investigar estos problemas, los objetivos de la presente tesis son: (i) investigar preliminarmente la relación existente entre la ACR y algunos indicadores de desempeño sísmico (por ejemplo, las derivas de piso y las relaciones demanda-capacidad). Tres edificios de 6 y 11 pisos, de MRF de RC son analizados; estos edificios tienen columnas con ACR excesivo, de acuerdo con los estándares. Los edificios prototipo originales son modificados a través de tres métodos diferentes para reducir el ACR; entonces, análisis modales y *pushover* se realizaron sobre los edificios originales y reforzados; la viabilidad de los otros edificios modificados se verificó a través de análisis modales únicamente. (ii) presentar un nuevo enfoque para la interacción "momento uniaxial-cargas axiales" en la dirección fuerte de las columnas de edificios bajos de MRF en acero. El enfoque derivado se aplica a tres especímenes diseñados conforme a las regulaciones europeas y americanas; tales especímenes representan secciones pequeñas, medianas y grandes. Estos resultados analíticos son comparados satisfactoriamente con los resultados de un análisis por el "método de los elementos finitos"; esta comparación respalda la precisión de la formulación propuesta. (iii) proveer ecuaciones para predecir los parámetros para definir la respuesta no-lineal de ECBP; su eficacia es examinada contra datos de experimentales. Una base de datos y una herramienta en base web fue desarrollada para caracterizar los parámetros de modelación de ECBP sometidas a momento y fuerza axial de compresión. Un modelo tri-lineal fue adoptado para representar todas las fases de la respuesta no-lineal de las conexiones.

Summary

Axial forces in columns of moment-resisting frames (MRF) have a paramount role for the seismic performance of these structural systems. Nonetheless, there are significant gaps in the literature entailing the influence of these forces in the seismic performance of MRF. Some of these gaps are: (i) there are poorly designed Reinforced Concrete (RC) columns of actual MRF buildings which can undergo Axial Compression Ratios (ACR) so high as their demand exceeds their capacity, even for only serviceability gravity load combinations; this lack commonly leads to insufficient seismic strength. Nonetheless, many seismic design codes do not specify limits for ACR, (ii) Existing design philosophies for the design of Exposed Column Base Plates (ECBP), fail to accurately predict the failure modes of these column-base connections; besides, these philosophies does not account for the moment-axial loads interaction in the components of these connections, (iii) there is a lack of reliable predictive models for the modelling parameters of ECBP subjected to moment and axial loads. In order to investigate these problems, this research aims to: (i) preliminary investigate relationships between the ACR and seismic performance indicators (e.g., inter-story drifts and demand-capacity ratios of columns in MRF). Three prototype 6 and 11-story RC MRF buildings are analyzed; these buildings have columns undergoing excessive ACR, according to the limits prescribed by standards. The original prototype buildings are modified through three different methods to reduce the ACR; then, code-type and pushover analyses are performed on the original and retrofitted buildings; the suitability of the other modified buildings is checked by code-type analyses only. (ii) present a new approach for the uniaxial moment-axial force interaction in the strong direction of columns of low-rise MRF. The derived approach is applied to three specimens designed according the American and European documents; such specimens represent small, medium and large sections. These analytical results are satisfactorily compared with a finite element analysis; this endorses the accuracy of the proposed formulation. (iii) provide predictive equations to estimate the various parameters defining nonlinear response of ECBP; their efficacy is examined against test data. A database and an associated tool were developed to characterize the modelling parameters of ECBP subjected to flexure and axial compression. A trilinear model was adopted to represent various phases of nonlinear response.

List of Figures

List of Tables

List of symbols

Latin alphabet. Lower case

a_{max}: Peak ground acceleration
b: Base of a rectangular reinforced-concrete element
b_f: Width of the flanges of a steel column section
b_{eff}: Effective width of a T-stub area
c: Damping coefficient. Horizontal distance of the side of a column web or flange to the border of the related T-stub (in European regulations)
d: Overall depth of the steel profile
e, e_{crit}: Load eccentricity, critical eccentricity
e_p: Critical eccentricity that causes the yielding of the plate (= min {$e1$, $e2$})
$e1$, $e2$: Eccentricity designation for low and high eccentricity loads, respectively
f: Distance from the centroid of the anchor bolts group to the centroid of the column
f_b, f_p: Required bearing stress in the concrete surface for low and high eccentricity loads, respectively
f'_c, f_{max}: Specified concrete compressive strength, nominal concrete bearing strength
f_{cd}: Design uniaxial concrete compressive strength according to EN 1998-1 (2004) ($\approx f'_c$ / 1.5)
$f_{c,GB}$: Design uniaxial concrete compressive strength according to GB 50011 (2010) ($\approx f'_c$ / 1.78)
f_{jd}: Design concrete bearing strength (Eurocode 3)
f_{yst}: Yield strength of reinforcing bars
g: Acceleration of gravity. Distance from the center of a corner bolt hole to the edge of the base plate
h: Base of a rectangular reinforced-concrete element
k: Stiffness coefficient. Number of folds for cross-validation process
l: Critical cantilever distance (= Max {m, n, $\lambda n'$})
l_{eff}, $l_{eff,1}$, $l_{eff,2}$: Effective length of a T-stub area, effective length for failure mode 1 (complete yielding of the flange) and 2 (bolt failure with yielding of the flange), respectively
m: Mass coefficient. Cantilever-distance from the edge of the steel plate to the assumed bending lines for the strong direction of the column
n: Number of years. Cantilever-distance from the edge of the steel plate to the assumed bending lines for the weak direction of the column
n': Distance that refers to the yield line theory
p_n: Probability of exceedance of the determined seismic action in n years
q, q_{max}: Uniformly distributed bearing-load for low and high eccentricity loads, respectively
r: number of modes to be included in the analysis
s: Corner radius ($s = r_c$ per AISC)
x: Relative displacement between the mass and the base (degree-of-freedom)
x_g: Horizontal ground displacement
$\dot{x}$: Relative velocity
$\ddot{x}$: Absolute acceleration ($= \ddot{y} - \ddot{z}_g$)
t_f, t_p, t_w: Thicknesses of the flanges, plate and web, respectively
$t_{mín}^{LS1}$, t_{min}^{LS2}, $t_{mín}^{LS3}$: Minimum thickness of plate for zero eccentricity, small eccentricity, and high eccentricity load scenarios, respectively

Latin alphabet. Upper case

ACI: American Concrete Institute
ACR: Axial Compression Ratio; also Axial Load Ratio (ALR) or Normalized Axial Force (NAF)
ACR_{max}: Maximum Axial Capacity Ratio in the columns of a story
ACR_{mean}: Average Axial Capacity Ratio in the columns of a story

AISC: American Institute for Steel Construction
AO: Original building A
AR: Retrofitted building A
A, A_b: Cross-sectional area of a steel column, and, one anchor bolt, respectively
A_g: Gross sectional area of a reinforced-concrete column
A_{rod}: Cross sectional area of the group of anchor bolts in the tensile side of the connection
A_{st}: Steel reinforcement area
B: Width of the steel plate (along the weak direction of the column)
B_{eff}: Effective damping factor
BO: Original Building B
BOL: Anchor bolt
BR: Retrofitted Building B
C: Constant used in proposed predictive equations
C_0, C_1, C_2, C_3: Coefficients to calculate the target displacement (according to (FEMA 356, 2000)
C_m: Equivalent modal mass participation factor of the first mode
C_M, C_θ: Coefficients for strength and deformation post-peak-deterioration, respectively
CO: Original Building C
COL: Column
CP: Collapse Prevention performance level (according to American standards).
CQC: Complete Quadratic Combination
CR: Retrofitted Building C
CV: Cross Validation for out-of-sample prediction
D: Displacement of the upper floor of the building relative to the ground
D_b: Diameter of anchor rods
DC: Damage Control performance level (according to American standards)
DCR: Demand-Capacity Ratio
DCR_{max}: Maximum Demand-Capacity Ratio per story
DCR_{mean}: Average Demand-Capacity Ratio of the columns of a story
DG1: Design Guide One by AISC
E_c, E_g, E_s: Modulus of elasticity of concrete, grout, and steel elements (= 200 GPa), respectively
$E_{col:}$ Modulus of elasticity of the column
E_{sh}: Hardening tangent modulus
EC3: Eurocode 3
ECBP: Exposed Column Base Plate
FEA: Finite Element Analysis
FEM: Finite Element Method
F: Base shear
$F_{C,l,Rd}$, $F_{C,r,Rd}$: Compressive resistant force of the left and right side of the base plate (= min $\{F_{c,Rd}$, $F_{c,fc,Rd}\}$), respectively
$F_{c,Rd}$, $F_{c,fc,Rd}$: Resistant force of the concrete under an individual T-stub in compression, resistant force of the steel column flange for a T-stub in compression
F_{Rdu}: Compressive resistance force of the T-stub area under the column flange ($F_{Rdu} = f_{jd}\ b_{eff}\ l_{eff}$ where f_{jd} is re-calculated by iteration)
$F_{T,l,Rd}$, $F_{t,w,Rd}$: Resistant tensile force of the connection ($F_{T,l,Rd}$ = min $\{F_{t,w,Rd}$, $F_{t,pl,Rd}\}$), resistant yielding force of the column flange in the traction side of the connection
$F_{t,pl,Rd}$, $F_{t,Rd}$, $F_{T,1\text{-}2,Rd}$: Resistant force associated with the flexural yielding of the plate in the traction side of the connection (considering the T-stub formed with associated bolts), resistant tensile force of a bolt, alternative resistant force of one group of anchor bolts
F_{yb}, F_{yp}, F_{yc}: Yielding stress of the anchor bolts, plate, and column, respectively
F_{ub}: Ultimate stress of the anchor bolts
HE: High Eccentricity
I_{col}: Moment of inertia of columns
IO: Immediate Occupancy performance level (according to American standards)
K_i: Lateral stiffness
K_e: Effective lateral stiffness

K_0^{bp} : Initial rotational stiffnesses of ECBP

K_1^{bp} : Pre-capping stiffness parameter

L_b, L_{col}; L_e: Total length of anchor bolts and column; embedment of anchor bolts, respectively

LD: Limited Damage limit state (according to European regulations)

LRFD: Load and Resistance Factor Design

LS: Life Safety performance level (according to American standards)

$M_{b,Rd}$: Design flexural strength of the connection associated with the fracture of anchor bolts (according to European standards); this variable is represented by M_{nb} in American standards

$M_{el,Rd}$, M_{Ed}: Maximum elastic resistance to bending moments, Factored internal bending-moment (according to European standards); M_{Ed} is represented by M_u in American standards

$M_{j,Rd}$: Magnitude of the flexural strength of the base-plate connection (in European regulations); this variable is represented by M_n^{bp} in American standards

M_{max}^{bp} : Ultimate strength of the ECBP (in moment units)

M_{nb}, $M_{nc,}$ M_{np}: Flexural strength of the connection associated with the fracture of anchor bolts (M_{nb} = $M_{b,Rd}$, Eurocode), yielding of the column (M_{nc} = $M_{N,Rd}$, Eurocode) and yielding of the steel plate (M_{np} = $M_{p,Rd}$, Eurocode), respectively

M_n^{bp} : Predicted (nominal) strength of the ECBP (minimum value between the fracture of anchor bolts, and, yielding of plate or column) in American standards; this variable is represented by $M_{j,Rd}$ in European regulations

$M_{N,Rd}$: Design flexural strength of the connection associated with the yielding of the column ($M_{N,Rd}$ = M_{nc} by AISC)

M_{pl}: Calculated bending moment at the steel plate due to the cantilever action

$M_{pl,1,Rd}$, $M_{pl,2,Rd}$: Moment associated with the failure modes 1 and 2, required to calculate $F_{t,pl,Rd}$

$M_{p,Rd}$: Design flexural strength of the connection associated with the yielding of the steel plate (according to European standards); this variables is represented by M_{np} in American standards

M_y^{bp} : Yielding strength of the ECBP (in moment units)

M_y^{col} : Yielding flexural strength of the column (in moment units)

M_u: Factored internal bending-moment at the column base (according to American standards); this variable is represented by M_{Ed} in European regulations

M-P: Moment-Axial loads interaction

M-θ: Moment-rotation relationship for ECBP

MPA: Modal Pushover Analysis

MRF: Moment Resisting Frame

MRSA: Modal Response Spectrum Analysis

N: Required axial strength according to HKBD (2013). Length of the steel plate (along the strong direction)

N_b: Total number of bolts in the connection

NC: Near Collapse limit state (according to European regulations)

NC: Number of Columns with DCR_{max} greater than 1 for the seismic combinations

$N_{C,C}$: Factored axial load for the column according to GB 50011 (2010)

N_{Ed}: Factored internal axial-force per European regulations (= P_u in American standards)

$N_{j,Rd}$: Axial capacity force of the connection for only-axially loaded columns

$N_{pl,Rd}$: Plastic resistance force of the gross cross-section

N_s: Number of stories of a building

N_{SPT}: Number of blows in the standard-penetration-test

$N_{n,max}$: Axial capacity force of the column according to NZS 3101-1 (1995)

N_0^*: Acting axial force in columns according to NZS 3101-1 (1995)

LD: Limited Damage limit state (according to European regulations)

P: Axial force in columns

P_{max}, P_{nc}, P_u: Nominal concrete bearing-capacity force, resistant axial force of the column, factored internal axial-force at the column base (P_u = N_{Ed}, Eurocode)

PLA: Plate

R: Response modification factor (in the regulations from United States). This factor is represented by different symbols in each standard; in the case of Spain (NCSE-02, 2002) it is termed μ, in the European standard (EN-1998, 2004) it is named q

R^2: Correlation coefficient

RC: Reinforced Concrete

$RMSE$: Root Mean Square Error of a Sample

RSB: Rectangular Stress Block

S: Soil coefficient. Standard deviation of a sample

S_a: Acceleration response spectrum (absolute)

S_d: Displacement response spectrum (relative)

S_v: Velocity response spectrum (relative)

S_x: Elastic section modulus in the strong direction of the column ($S_x = W_{el,min}$, Eurocode)

S1, S2, S3: Specimens 1 (light section), 2 (medium section), 3 (deep section)

SD: Significant Damage limit state (according to European regulations)

SE: Small Eccentricity

SEL: Seismic Loads

SMRF: Steel Moment Resisting Frame

SRSS: Square Root of the Sum of the Squares

T: Natural (fundamental) vibration period of the structure ($T = 2\pi/\omega_0$). Return period of an event. Resistant tensile force of the anchor bolts group ($T = \Sigma F_{t,Rd}$ per Eurocode)

T_A, T_B: Vibration periods used at the design spectrum of the Spanish code

T_e: Equivalent vibration period

T_{eff}: Effective vibration period

T_i: Natural vibration period of the i-th mode

T_0/T_C: Left/right corner vibration periods of the plateau in design spectrum of the NSR-98 design code

T_0/T_S: Left/right corner vibration periods of the plateau in design spectrum of the ASCE/SEI 7-10 2010

T_L: lower bound for very long vibration periods of the NSR-98 design code

V: Earthquake force (base shear).

V_u: Factored internal shear-force at the column base

V_y: Yield strength of the building obtained from the idealized capacity curve

VFL: Vertical Factored Loads

VSL: Vertical Service Loads

W: Weight of the building

X: Mathematical simplification to calculate the critical cantilever-distance of the steel plate. Mean value of a sample

$Y1$, $Y2$: Length designation of the bearing area for a low and high eccentricity scenario, respectively (along the strong direction of the column)

$Z_{C,l}$, $Z_{C,r}$: Distance from the centroid of the column to the centroid of the left and right flange in compression, respectively

ZE: Zero Eccentricity

$Z_{T,l}$, $Z_{T,r}$: Distance from the centroid of the column to the centroid of the left and right group of anchor bolts (in traction), respectively

Greek alphabet. Lower case

α: Ratio of post-yield stiffness to the effective elastic rigidity

α_1: Whitney stress-intensity factor (= 0.85)

β_j: Coefficient for the concrete of the pedestal, which may be taken as 2/3

β_0 to β_9: Regression coefficients for the proposed predictive equations

δ_t: Target displacement

ε_{ys}: Yielding strain of steel components

ζ: Critical damping factor

ζ_{eq}: Equivalent viscous damping

ϕ: Concrete rebar diameter
ϕ_a: Strength reduction factor for axial capacity
γ_c: Concrete unit weight
γ_{M0}: Partial safety factor for the material strength per Eurocode 3
θ_y^{bp} , θ_{max}^{bp} : Yielding and maximum rotations of the ECBP
θ^{bp} : Rotation of ECBP
θ_1^{bp} : Pre-capping rotational parameter, associated with the start of the plastic plateau
λ: Coefficient that refers to the yield line theory. It is used to calculate the critical cantilever distance of the steel plate
λ_f, λ_w: Slenderness ratio for the flanges and web, respectively
μ: Ductility factor (= *R*)
ρ: Importance factor
ρ_{prov}: Provided steel reinforcing ratio
ρ_{req}: Required steel reinforcing ratio
ν: Poisson's ratio
σ_1, σ_3: Maximum and minimum principal stresses (tensile and compressive, respectively)
ω: Reduction factor to allow for the interaction with shear in the column web
ω_d: Damped natural frequency
ω_0: Undamped natural frequency of the system

Greek alphabet. Upper case

Δ: Displacement. Lateral displacement
Δ^{col}, $\Delta^{cantiliver}$: Horizontal displacement at the top due to the column and, measured horizontal displacement, respectively

1 INTRODUCTION

1.1 Background and motivation

With regards to **Reinforced Concrete (RC) Moment Resisting Frame (MRF) buildings**, most of the design codes do not limit Axial Compression ratio (*ACR*), but only Demand Capacity ratio (*DCR*). However, suggesting bounds for *ACR* could prove useful in early design stages, by saving time, effort and money. In order to encompass the importance of limiting the *ACR* in RC MRF, the following analysis shall be referred: as explained by Yuen et al. (2016), the implicit limits to *ACR* by ACI 318-14 (2014) and NZS-95 (1995) are between 0.5 and 0.9. An assessment of an existing six-story building located in a low seismicity zone was made by this researcher (see Villar-Salinas et al. (2021)), shows that the *ACR* of two columns on the first story are close to 0.59 due to service loads and; the *DCR* of these columns is excessive for both vertical and seismic loads (Villar-Salinas et al., 2021). Hence, the building shows an inappropriate structural safety for low seismicity effects and yet for vertical loads and the *ACR* limits by ACI 318-14 and NZS-95 might be inadequate for RC columns of MRF with high *ACR* to comply with all the code limit-states. Overall, there is an opportunity of research on the influence of the columns-*ACR* on the global strength and ductility of RC MRF buildings, considering the bi-directional effects of earthquakes and the whole code load-combinations, which is normally difficult to reproduce in the laboratory tests. Subsection 3.1 discusses this issue more deeply.

Regarding **steel MRF buildings with Exposed Column Base Plates (ECBP)**, although the classical approaches for the strength design of ECBP, according to either American or European standards, are conservative to predict the flexural strength of these connections from a deterministic standpoint, there are some research opportunities suggested by other researchers, which motivated the present study: i) the combined effects of the axial force *P* and moment resistance *M* are not discriminated for each component of the connection (Gomez et al., 2010; Kavoura et al., 2018a; Latour et al., 2014; Torres Rodas et al., 2016) and hence, the failure mode of these joints cannot be accurately predicted, ii) the overall check of the M-P interaction capacity of the components may be more consistent with probabilistic modern approaches (Song et al., 2021). In addition to this, there is a significant gap is in the area of guidance for simulating the nonlinear flexural behavior of these connections, within the context of modern performance assessment frameworks (Zareian and Kanvinde (2013), and, Latour and Rizzano (2019)). Further discussion on these research gaps on the strength and simulation of ECBP are presented in subsections 4.1 and 5.1, respectively.

The concern of this researcher for this subject arises from his former teaching and consultancy activities in Colombia; looking for improving his research skills, this student started his PhD studies in October 2020, under the supervision of Prof. Francisco López Almansa. As discussed in the previous paragraph, this work focuses on the influence of *ACR* on the seismic performance of MRF buildings. The conducted research can be broadly classified into **three parts**.

In the **first part** of this research, three existing MRF buildings with RC columns exhibiting high *DCR* in columns under vertical loads, are analyzed. One low-rise building and two mid-rise

buildings which are located in a low seismic hazard zone. Three types of alterations are performed: retrofitting the abovementioned overloaded columns by steel jacketing, increasing the concrete strength, and reducing the number of stories. Code-type and pushover analyses are performed on the original and retrofitted buildings; the suitability of the other modified buildings is checked by code-type analyses only. Then, the results are used to evaluate the influence of the *ACR* on the global seismic response of the buildings.

The **second part** of this work examines the influence of the M-P interaction on the strength and failure modes of ECBP and suggests a design methodology. Additionally, the variability of the thickness of plate for different values of *ACR* is analyzed following the classical design approaches.

In the **third part** of this thesis, a database of experimental results was compiled, and then, a related web-based tool was developed to characterize the moment-rotation properties of ECBP subjected to flexure and axial compression, adopting a trilinear model to represent the full range of their nonlinear response. Predictive equations for the various parameters defining the selected model are presented, and their accuracy was examined against test data.

1.2 Objectives

1.2.1 Main objective

The main goal of this study is **TO SHOW THAT *ACR* IS A RATHER RELIABLE INDICATOR OF THE SEISMIC PERFORMANCE OF TWO MRF BUILDING SYSTEMS, NAMELY RC MRF AND STEEL EXPOSED COLUMN-BASE PLATES**; if this hypothesis is confirmed, the convenience of establishing bounds for *ACR* and including this indicator into strength and stiffness predictive models will be apparent. As well, it is expected that the obtained conclusions might be incorporated into the design codes.

1.2.2 Specific objectives

To reach the aforementioned main goal, these specific targets are pursued:

- To select prototype RC MRF buildings with excessive *ACR* in columns according to the limits prescribed by standards. Then, to overcome this issue, three types of alterations are studied.
- To perform code-type Modal Response Spectrum Analyses on prototype buildings to establish relationships between *ACR*, *DCR* and story drift.
- To carry out Modal Pushover Analyses on the original and retrofitted prototype buildings in order to corroborate and deepen the conclusions from the Modal Response Spectrum Analyses.

- To present an approach for obtaining the uniaxial moment-axial loads (M-P) interaction diagrams of ECBP components, along the strong direction of the column. Then, to apply this approach to code-type specimens of ECBP.
- To perform Finite Element Analysis (FEA) on the specimens to reproduce their failure modes and stress distributions, validating against previous experimental investigations. Then, to compare the FEA results with the analytical ones.
- To analyze the variability of the thickness of plate as *ACR* increments, when the classical design approaches are followed.

- To propose an approach to define the full rotational response of ECBP connections through a trilinear backbone curve.
- To assemble a publicly available database of published test results of ECBP, performed in the United States, Europe and Asia during the last thirty years; this aims to facilitate convenient estimation of the rotational response of ECBP.
- To provide predictive equations for the parameters defining nonlinear response of ECBP, evaluating *ACR* as a potential predictor variable.

This list is organized according to the aforementioned three parts this work is divided in.

1.3 Methodology

This section describes in more detail the investigation carried out to achieve each of the above specific objectives.

Selection of the prototype buildings. Three actual prototype buildings have been selected to represent RC MRF buildings with excessive *ACR* in columns according to the limits specified by standards; these are one low-rise (6 stories) and two mid-rise (11 story) buildings. The low-rise building has one-way solid slabs, while the mid-rise buildings have two-way solid ones. All the buildings have rectangular cast-in-situ columns and beams. The buildings are located in Cartagena de Indias (Colombia); this location is a low seismic hazard zone, which was conveniently accepted to show that *ACR* significantly influences the seismic performance of R MRF buildings, even in low seismicity scenarios. To fulfil the abovementioned limits for *ACR*, three types of alterations of the original buildings were investigated: retrofitting the overloaded columns, increasing the concrete strength, and reducing the number of stories. Then, there are 12 prototype buildings in total.

Code-type Modal Response Spectrum Analyses on prototype buildings. The Modal Response Spectrum Analysis is the method selected herein for the calculation of the story drifts, *ACR* and *DCR* of all the prototype buildings, original and modified ones. The design spectrum for the structural analysis of the buildings was defined for the performance level named Life Safety (LS), according to the Colombian code NSR-10 (2010). Bidirectional seismic-loading effects were considered as 100% in one direction and 30% in the orthogonal one. The maximum *DCR* and story drifts of each story of the prototype buildings were plotted against the correspondent *ACR*. Finally, suggested values of *ACR* to fulfil the code limits for both, *DCR* and story drifts, were determined graphically.

Modal Pushover Analyses on original and retrofitted buildings. The Modal Pushover Analysis method was selected to assess the non-lineal response of individual elements and the global system of the original and retrofitted buildings; the plastic hinges for the columns and the capacity curves for the global systems, were obtained. This method was not applied to the buildings modified by "increasing the strength of the concrete", and "reducing the number of stories"; for the former modified-buildings, similar analysis and conclusions were included in a previous work of the author (Villar-Salinas et al., 2021); for the second modified-buildings, their non-lineal responses are not useful to deepen the conclusions from the Modal Response Spectrum Analyses. The performance levels considered for both the hinge properties of the columns and the global structure are the conventional Immediate Occupancy (IO), LS and Collapse Prevention (CP).

New approach for the uniaxial M-P interaction diagrams of ECBP. This approach consists in generalizing the current American and European formulations by determining the stress distribution that corresponds to any point of the moment-axial force interaction diagram. The derived approach was applied to three code-conforming specimens designed according the American and European documents. 180 configurations of ECBP were analyzed to represent light, medium and deep sections. The whole range of M-P load pairs was contemplated and grouped into three load scenarios: Zero Eccentricity, Small Eccentricity and High Eccentricity. To be consistent with non-seismic low-rise MRF, the column sections selected are HEA200, HEA300 and HEA400 profiles, respectively.

Finite Element Analysis of code-type specimens of ECBP. The meshing of the finite element models is composed with hexahedral elements for steel components (column flanges and web, and the steel plate). Tetrahedral-refined elements were used for the surface surrounding anchor bolts and, the volume of the concrete footing. For the sake of validation of the simulation methodology, one calibration model was analyzed using the same properties of the test # 1 conducted by Gómez et al. (2010) and then, the simulated and the experimental responses were

compared. Then, the results of the FEA of the specimens were compared with the results of the application of the proposed approach.

Variability of the thickness of plate as *ACR* increments. The thickness of plate is an important design variable of ECBP, according to either American or European standards. Hence, this variable was selected as the response variable to investigate its variability due to M-P combinations according to the classical approach of the mentioned standards, while the other design variables of specimens remain constant. Then, the minimum thickness of plate required for a whole range of M-P pairs is calculated, representing the three loads scenarios previously defined.

Trilinear model to define the rotational response of ECBP. A trilinear model for the backbone of moment-rotation curves was used to idealize the response of these curves in a parametric way. Such a model is sufficient to represent the ductility, stiffness and strength degradation of the connections.

Public database of experimental tests on ECBP. A systematic assemblage of experimental data was developed and made publicly available. The database contains information from 84 tests aimed at obtaining individual parameters or the full range of the moment-rotation curves of ECBP with shallow column sections.

Predictive equations for modelling parameters of the rotational response of ECBP. Predictive equations are provided to estimate the various parameters defining nonlinear response of ECBP. The approach is based on a combination of behavioral insights and regression, which are estimated from the dataset of experiments on ECBP. The approach is accompanied by a tool to facilitate convenient computation.

Conclusions. Both overall and particular conclusions are issued.

Further research. Taking profit of the results of this research, new research needs are identified and discussed.

1.4 Organization of this document

This document is organized into six chapters and one appendix, where the first chapter is this introduction. The second chapter contains the state-of-the-art, which comprises a review of the seismic design methodologies and the most relevant strength models for ECBP. The third chapter describes the analyses performed on prototype RC MRF buildings to determinate the influence of *ACR* on their seismic response. The fourth chapter presents a numerical analysis of the moment-axial interaction of ECBP. Chapter 5 shows an approach to estimate the rotational parameters for the performance-based assessment of ECBP. Chapter 6 depicts the overall conclusions of the research and the future intended investigation. A list of the consulted bibliography is included after the sixth chapter. describes fundamental issues of axial pressure waves. Appendix A lists the publications generated during this research.

2 STATE OF THE ART

2.1 Earthquake-Resistant Design Methods

This section presents a brief introduction and a concise review of earthquake-resistant design methods of structures. Although this study has a general context, it is especially applicable for the buildings subjected to horizontal seismic inputs. Formulations for other situations (e.g. vertical inputs or structures other than buildings) are basically similar.

The so-called *Earthquake Analysis Methods Based on Resistance* appeared for the first time in the year 1923 (Kharazian, 2017), within the Japan seismic regulations (first such requirement in the world) (Hasegawa, 2013). These procedures were intended to provide buildings with lateral (horizontal) resistance; it was believed that if the structure of the building had enough lateral resistance it should be capable of surviving the design earthquake. This resistance is guaranteed by designing the structure to be able to withstand horizontal forces applied at each floor level and in each direction of the building (usually two orthogonal directions). Figure 2-1 illustrates this concept.

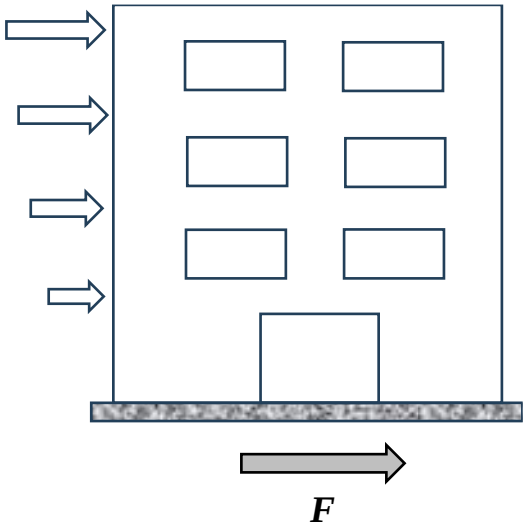

Figure 2-1. Lateral forces that are equivalent to a seismic input

In Figure 2-1, F is the sum of the forces acting at each floor level; in other words, the horizontal interaction force between the ground and the building. F is also known as base shear. Obviously, the value of F quantifies the severity of the earthquake effect on the building.

In the firstly developed earthquake-resistant design methods, the horizontal forces represented in Figure 2-1 were obtained by multiplying the weight of each floor by a constant coefficient. This ratio between the horizontal and vertical forces was called seismic coefficient and in the first 1923 Japanese seismic code (Ohashi, 1993) it was estimated as 0.1. This value gradually increased as it was experienced that structures designed with this resistance value failed when an earthquake

stronger than expected occurred. This ratio took to the values of 0.10, 0.15, and 0.20 until, thanks to the development of computers and by having more and more seismic experiences, it was concluded that structures that had been designed with a certain lateral resistance, did not reach collapse but could suffer damage in the case of a larger earthquake. After that, resistance was not the primary goal, and everybody started paying more attention to ductility; it can be roughly defined as the ability of a given structure to resist after the onset of damage. The ductility of a given building can be estimated from observed damages or by numerical simulation. The regulations began to introduce the concept of ductility by quantifying it with a *response reduction factor*, which reduces the equivalent lateral forces (Figure 2-1); it was mentioned in the 1957 American design code (Housner, 1990). Thus, this approach has been incorporated into the current worldwide regulations. In summary, most of the earthquake-resistant regulations require providing buildings with a certain level of lateral resistance. This resistance is obtained by dividing the resistance that a given building should have to remain in the elastic range under the design input by the response reduction factor. This factor should obviously be equal to or greater than unity. This coefficient is represented by different symbols in each standard; in the case of Spain (NCSE-02, 2002) it is termed μ, in the European standard (EN-1998, 2004) it is named q, and in the United States (IBC, 2000) it is known as R. It is remarkable that, in fact, this ratio does not consider only the ductile behavior of the structure but also includes the over-resistance of the building due to the conservative considerations that are regularly considered (safety factors, among others) and the increase of the material resistance under dynamic inputs (strain rate effect).

In any case, it should be kept in mind that in these methods the effect of the earthquake on the structure is characterized by means of equivalent static forces (Figure 2-1); they are determined as those that generate a lateral displacement equal to the maximum one that would occur along the duration of the earthquake. However, another possible strategy is to represent the seismic action in a much more direct way: as input accelerograms. In this case, the dynamic analysis must be performed to determine the time-history responses; then, the maximum values will be selected, they would represent the design demands. This formulation is often referred to as *earthquake-resistant design based on dynamic calculations*. This strategy seems appropriate and has apparently shown to be quite capable of simulating the actual seismic behavior of structures with great accuracy and reliability; however, there are some drawbacks that hinder the use of such formulations: (1) the information about the earthquakes that may occur in a particular structure during its lifetime is limited, which severely impairs the accuracy of the study, (2) for economic reasons, structures are designed to behave nonlinearly during the design earthquake (the most severe earthquake expected with a reasonable probability) and, hence, nonlinear dynamic analyses are a must. Dynamic analyses in the nonlinear regime are much more complex than the already complex, dynamic linear calculations. Currently, the most common way of characterizing the dynamic effect of earthquakes is by equivalent static forces (or other non-dynamic quantities, e.g., not forming part of a dynamic calculation) obtained from elastic response spectra. Next subsection explains how to determine these values using response spectra.

2.1.1 Earthquake-resistant design based on spectra

In general terms, these methods are based on estimating the equivalent static forces (which characterize the effect of the seismic action) in terms of the fundamental period of the structure. This is done by using response spectra; they are plots whose ordinates are certain response magnitudes and whose abscissas are the natural periods of SDOF systems that represent the structure. Up to date, three types of spectra have been basically proposed: absolute acceleration, relative displacement, and energy spectra. In the absolute acceleration spectra, the ordinates are the ratio between the maximum absolute acceleration in the top of the building and the maximum input acceleration in the base of the building. In the relative displacement spectra, the ordinates are the ratio between the maximum relative displacement between the top and the base of the building and the maximum input relative displacement. In the energy spectra, the ordinates are the input energy introduced by the seismic input in the building. These three types of spectra are described next in this subsection; applications to earthquake-resistant design are described in the

three following subsections, respectively. It is noteworthy that each of these three spectra considers a meaningful response magnitude: the relative displacement is an indicator of the apparent structural damage level (i.e. not cumulative), the absolute acceleration is related the human perception of the motion and the damage to the facilities (and, more generally, to all the non-structural elements), and the energy reports on the accumulated structural damage.

The energy spectra are usually expressed in terms of equivalent velocity, which is the square root of the ratio between the double of the input energy and the mass.

Linear spectra plot the ratio between the maximum values of the response of an elastic single-degree-of-freedom system and of the input acceleration. Figure 2-2 shows an elastic model of a single-degree-of-freedom system undergoing a horizontal ground motion x_g; Figure 2-2.a displays a single-story building (highly suited to be represented with a SDOF model) and Figure 2-2.b presents its mechanical model.

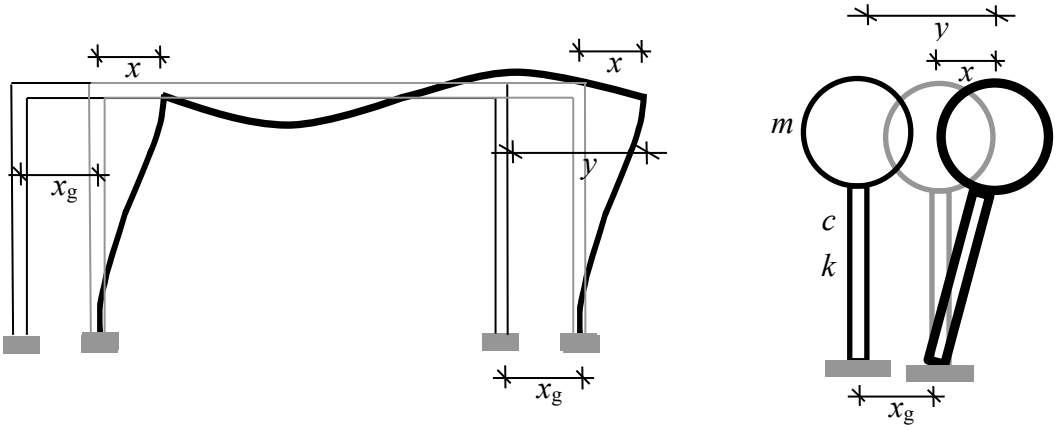

(a) Single-story building (b) Mechanical model

Figure 2-2. Elastic single-degree-of-freedom system

In Figure 2-2, *m*, *c*, and *k* are the mass, damping, and stiffness coefficients, respectively, *x* is the relative displacement between the mass and the base (degree-of-freedom) and x_g is the displacement of the ground. Yet this formulation is commonly applied to horizontal motion, can be also considered for vertical vibrations.

The equation of motion of the system described in Figure 2-2 can be written in any of these forms:

$$m\,\ddot{y} + c\,\dot{x} + k\,x = 0 \qquad\qquad m\,\ddot{x} + c\,\dot{x} + k\,x = -m\,\ddot{x}_g \tag{2-1}$$

By dividing both sides by *m*, relation (2-1) becomes

$$\ddot{x} + 2\,\zeta\,\omega_0\,\dot{x} + \omega_0^2\,x = -\ddot{x}_g \tag{2-2}$$

In this relationship, ω_0 is the undamped natural frequency of the system and ζ is the critical damping factor. These coefficients are given by

$$\omega_0 = \sqrt{\frac{k}{m}} \qquad\qquad \zeta = \frac{c}{2m\omega_0} \tag{2-3}$$

The damped natural frequency ω_d is related to ω_0 and to ζ by

$$\omega_d = \omega_0 \sqrt{1 - \zeta^2} \tag{2-4}$$

It is remarkable that, unless the damping ζ takes extremely high values, ω_0 and ω_d are nearly coincident.

The acceleration, velocity, and displacement spectra are obtained, for each input $x_g(t)$, as the maximum values of the absolute acceleration $\ddot{y}$ (where $\ddot{x} = \ddot{y} - \ddot{z}_g$), relative velocity $\dot{x}$ and relative displacement x. They depend on the natural period T ($T = 2\,\pi/\,\omega_0$) and on the damping factor ζ. These quantities are obtained by the following linear relationships (Chopra, 2007; Clough & Penzien, 1993; García Reyes, 1998):

$$x = -\frac{1}{\omega_d} \int_0^t \ddot{x}_g(\tau) \sin \omega_d (t - \tau)\, e^{-\zeta\, \omega_0\, (t-\tau)}\, d\tau \tag{2-5}$$

$$\dot{x} = -\int_0^t \ddot{x}_g\,(\tau) \cos \omega_d (t - \tau)\, e^{-\zeta\, \omega_0\, (t-\tau)}\, d\tau + \frac{\zeta}{\left(1 - \zeta^2\right)^{½}} \int_0^t \ddot{x}_g\,(\tau) \sin \omega_d (t - \tau)\, e^{-\zeta\, \omega_0\, (t-\tau)}\, d\tau \tag{2-6}$$

$$\ddot{y} = -2\,\zeta\,\omega_0\,\dot{x} - \omega_0^2\,x = 2\,\zeta\,\omega_0 \int_0^t \ddot{x}_g\,(\tau) \cos \omega_d (t - \tau)\, e^{-\zeta\, \omega_0\, (t-\tau)}\, d\tau + \frac{1 - 2\,\zeta^2}{\left(1 - \zeta^2\right)^{½}} \omega_0 \int_0^t \ddot{x}_g \sin \omega_d (t - \tau)\, e^{-\zeta\, \omega_0\, (t-\tau)}\, d\tau \tag{2-7}$$

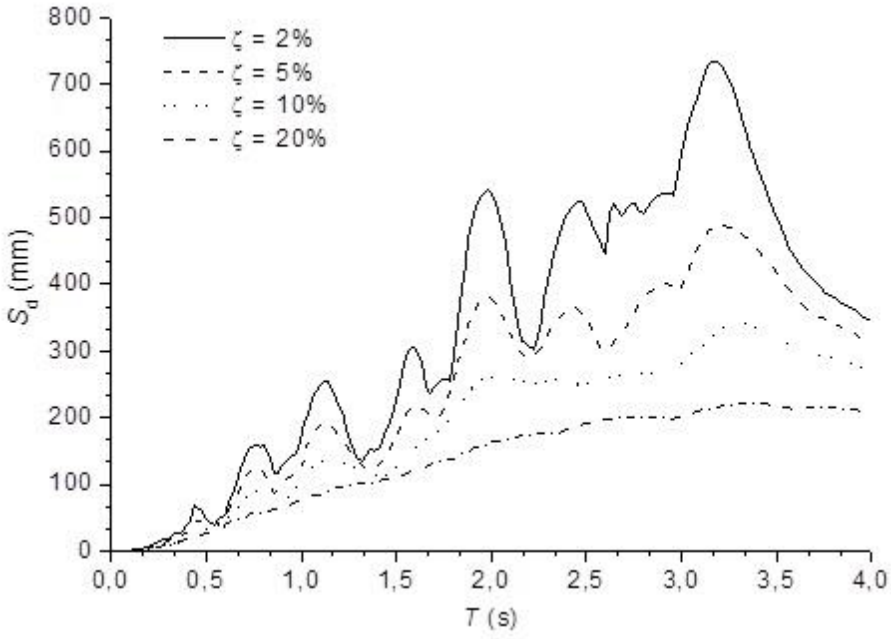

Figure 2-3. Relative displacement spectra

Figure 2-3, Figure 2-4, and Figure 2-5 show relative displacement, relative velocity, and absolute acceleration spectra, respectively. Such spectra correspond to the accelerogram registered in the ICA2 station (E-W component) during the Pisco earthquake, 15 August 2007.

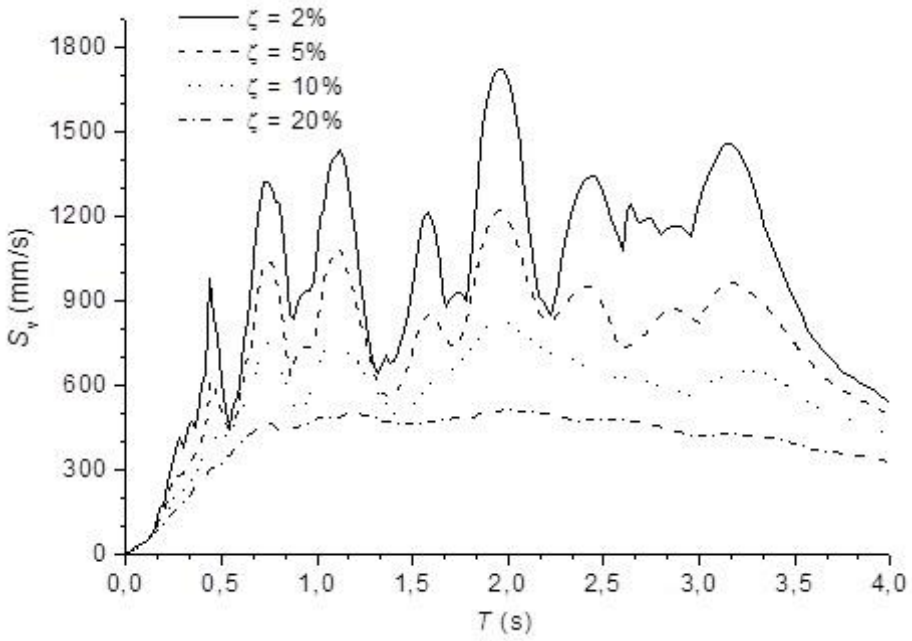

Figure 2-4. Relative velocity spectra

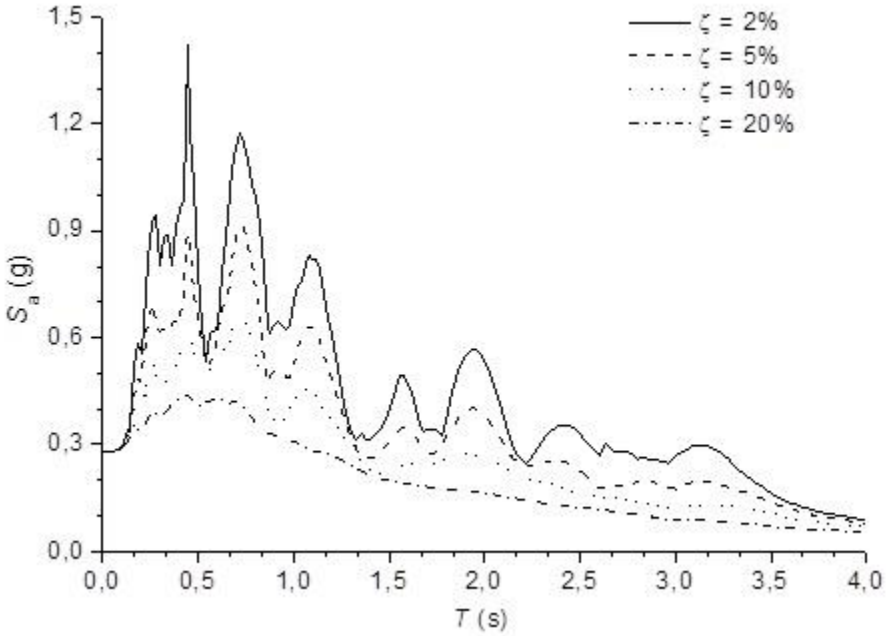

Figure 2-5. Absolute acceleration spectra

Figure 2-3, Figure 2-4, and Figure 2-5 show that the spectral ordinates decrease with the increasing damping ratio; this shows that damping has a beneficial effect since it contributes reducing relevant response magnitudes (relative displacement, relative velocity, and absolute acceleration). Moreover, the spectrum corresponding to zero damping exhibits sharper peaks than the spectra for non-zero damping; it means damping contributes to smoothen the spectra, e.g. making it less sensitive to small period changes.

It has been demonstrated by Chopra (2007) that for small values of damping and not too long periods (under 10 seconds), the velocity spectra are obtained by multiplying the acceleration spectra by $T / 2\pi$ and that the displacement spectra are obtained in the same way from the velocity ones:

$$S_v = S_a \ (T / 2\,\pi) \qquad S_d = S_v \ (T / 2\,\pi) = S_a \ (T / 2\,\pi)^2 \tag{2-8}$$

These relationships among the three types of spectra allow an easy shifting among them. At this point it should be clarified that, in fact, in order to satisfy these relationships, it is necessary to modify slightly the spectra of velocity and acceleration; hence, they should be termed in a correct way pseudo-velocity and pseudo-acceleration spectra (Chopra, 2007; Clough & Penzien, 1993; García Reyes, 1998). In this thesis, we will usually replace these names by velocity and acceleration spectra.

Figure 2-3, Figure 2-4, and Figure 2-5 correspond to the spectrum of a single input and consequently are not applicable for the earthquake-resistant design of a particular structure as it would not be reasonable to design it only to support that single input. In fact, different accelerograms should be considered and then the spectrum envelope should be taken. The earthquake-resistant design standards propose different spectra whose shape is similar to those of Figure 2-3, Figure 2-4, and Figure 2-5, although they are significantly smoother. As an example, the spectrum of the Spanish code (NCSE-02, 2002) is shown in Figure 2-6.

2.1.2 Absolute acceleration response spectra

As discussed in the previous subsection, the absolute acceleration response spectra are curves that represent, in ordinates, the ratio between the maximum values of the absolute acceleration of the SDOF system that represents the dynamic behavior of the structure in each vibration mode and the ground acceleration. The design spectra are smoothed envelopes obtained from several individual records.

Figure 2-6 shows, the design spectrum of the Spanish regulation (NCSE-02, 2002).

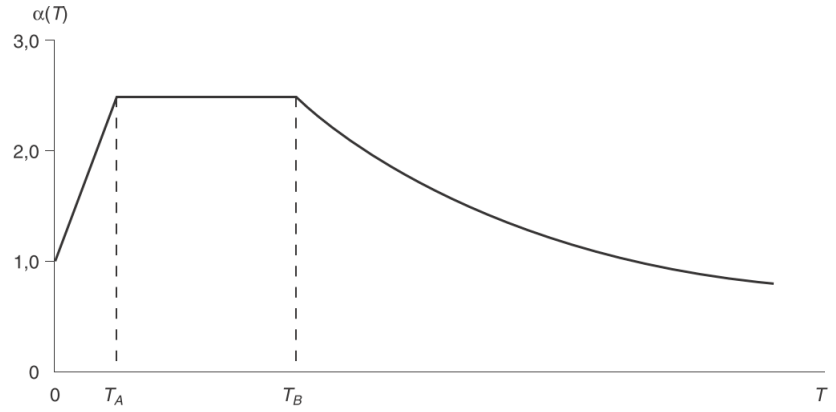

Figure 2-6. Design acceleration spectrum (NCSE-02, 2002)

The spectrum is shown in Figure 2-6 consists of three branches: a linearly increasing one (e.g. with exponent 1), a constant one (e.g. with exponent 0), and a hyperbolically decreasing one (e.g. with an exponent −1). Periods T_A and T_B depend on the characteristics of the soil, being higher as it has less stiffness; in some codes, the spectral ordinate (e.g. the height of spectrum) also grows as the flexibility of the soil does. The interpretation of each of these branches in terms of the effect of the earthquake on the structure is quite clear: (1) short-period structures are very rigid (usually they are low-rise) and tend to behave as the surrounding soil, but its motion is amplified as its rigidity decreases, (2) in the medium period range, the ground motion reaches its highest

amplification inside the building, and (3) in the long periods range, structures are flexible enough so that its stiffness is not capable of overcoming the high inertia forces. This interpretation helps us to understand the influence of the soil stiffness in T_A and T_B: for stiff soil, the range of building periods whose motion is highly amplified (in between T_A and T_B) is narrow, while this range widens and encompasses higher rise buildings as the soil becomes less stiff.

This spectrum is commonly presented in dimensionless form (the ordinates S_a are dimensionless); in this way the base shear is determined as the product of the weight of the building (W), the soil coefficient (S), the importance factor (ρ), and the peak ground acceleration (a_{max}) divided by the ductility factor R:

$$F = S_a(T)\ W\ S\ \rho\ a_{max} / R \tag{2-9}$$

In this relation W is the weight of the building; obviously, it depends on the percentage of live load that is simultaneous with the design earthquake, each code specifies this percentage in terms of the use of the building. S is the soil coefficient; for hard soil (rock and stiff soil) its value is usually 1 and it takes higher values for softer soils (S rarely reaches values greater than 1.50, except on very soft soils). The importance factor ρ is a coefficient that quantifies the severity of the consequences of the collapse of the building; in buildings of normal importance (such as residential constructions) is $\rho = 1$ and for more important buildings is $\rho > 1$. a_{max} is the design peak ground acceleration expressed in "g". The values of a_{max} are specified by the seismic design codes; usually, each country is divided into distinct zones, each of them with its own value of a_{max}. In the Spanish seismic regulations, the values of a_{max} range from 0.04 g (minimum considered value) and 0.25 g (for some municipalities in the province of Granada). The Spanish regulations quantify a_{max} as the expected seismic acceleration on stiff soil (not rock) for an earthquake with 500 years return period. It is remarkable that this criterion does not coincide with those considered in most countries; normally it is considered as the expected seismic acceleration in rock for a return period of 475 years. Finally, the response reduction factor R (*ductility* behavior factor) represents the ability of the structure to undergo plastic deformation until failure; in other words, it represents the safety margin of the structure after the onset of plastification. The current design standards estimate the values of R in a rather empirical way; these values basically depend on the type of structure and of the structural detailing, especially the connections among members. In the Spanish code (NCSE-02, 2002), this coefficient is denoted by μ and four situations are considered: $\mu = 1$ (no ductility), $\mu = 2$ (low ductility), $\mu = 3$ (high ductility), and $\mu = 4$ (very high ductility); other codes often consider higher values for this coefficient. Figure 2-6 shows that $S_a(0) = 1$; replacing this result in equation (2-9)) we conclude that for structures of high horizontal stiffness when $S = \rho = 1$, the equivalent static force is equal to $a_{max}\ W / R$. Consequently, since the acceleration in the base and the top of this type of structures should be virtually alike regardless of ductility, it follows that R should tend to 1 when T approaches zero.

In multi-story buildings, F represents the sum of the forces acting on each floor; in other words, it is the horizontal interaction force between the ground and the building (Figure 2-1). This force has to be distributed among the floors proportion to their masses and modal amplitudes (for the considered vibration mode of the building). The forces acting at each level represent the equivalent seismic effect; hence, they can be used to obtain the lateral resistance to be provided to the building.

In single-degree-of-freedom systems (typically, used to describe single-story buildings), the interpretation of the abscissa of the spectrum is very clear, as it represents the natural period of the system. In actual structures (typically multi-story buildings), multi-degree-of-freedom models should be considered. In this case, the application of this method is carried out usually in modal coordinates; in each *i-th* mode, its natural period T_i is considered. The structure should be decomposed in different vibration modes, the maximum response for each mode is calculated and then such responses are combined by using empirical rules (SRSS "Square Root of the Sum of

the Squares", CQC "Complete Quadratic Combination" (NCSE-02, 2002), among others). Typically, the combinations are set in terms of the shear forces on each floor, in other words, the sum of shear forces on the columns and walls of each floor. For each mode, the situation is similar to that described in Figure 2-1; the main difference is that the interaction force F has to be distributed among the different floors in proportion to their masses and modal amplitudes corresponding to the considered mode. The regulations usually specify the number r of modes to be included in the calculation, two types of criteria are generally provided: empirical ones and criteria that are more complex and are based on the distribution of equivalent modal masses (Chopra, 2007; Clough & Penzien, 1993; García Reyes, 1998). The empirical criteria often link the value of r with the fundamental period of the building and its plan symmetry; r generally ranges from 1 (for symmetrical buildings of small to medium height) and 4 (for high-rise buildings asymmetric). The criteria based on the equivalent mass of each mode often recommends a value of r such that the sum of the equivalent masses of the modes included in the combinations reach at least 90% of the total mass of the building, in some cases (EN-1998, 2004) also reports that should include all modes whose equivalent modal mass exceed 5% of the total mass of the building.

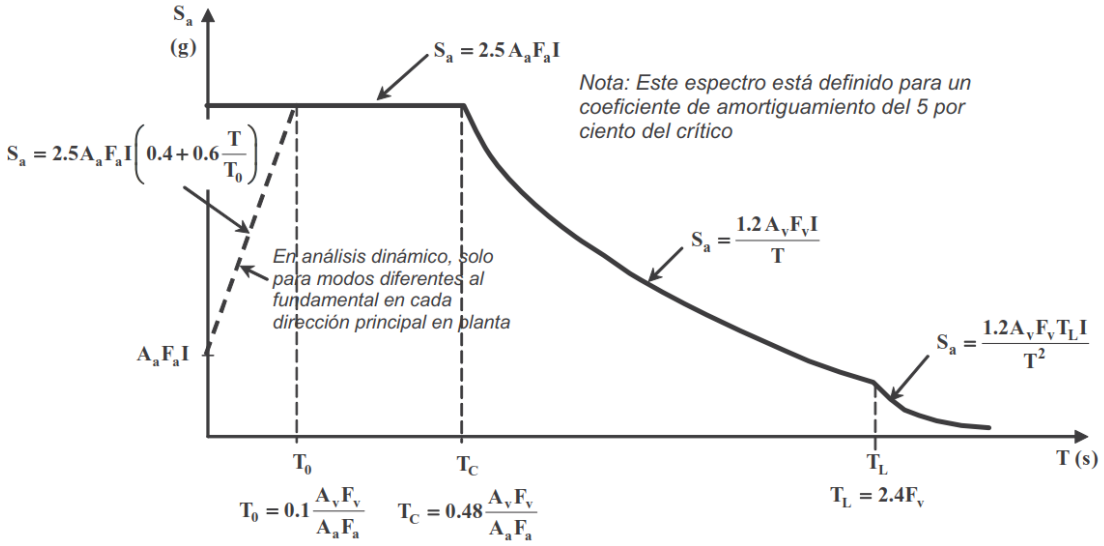

Figure 2-7. Design acceleration response spectrum (NSR-10 (2010))

It should be emphasized that equation (2-9) represents, with minor modifications, the approach suggested by almost all the current earthquake-resistant regulations.

Figure 2-7 shows another example of design acceleration spectrum, obtained from the Colombian standard (NSR-10 (2010)). Figure 2-7 shows, similarly to Figure 2-6, a typical absolute acceleration spectrum, which is divided into four segments: (1) short periods ($T < T_0$), the spectrum presents a linearly increasing branch, (2) medium periods ($T_0 < T < T_C$), the spectrum shows a horizontal branch (commonly known as plateau), (3) long periods ($T_C < T < T_L$), the spectrum usually decreases hyperbolically (with exponent -1), and (4) very long periods ($T_L < T$), the spectrum is again horizontal but with lower height than the medium periods plateau. Similarly to what happens in Figure 2-6 with periods T_A and T_B, the values of the periods T_0, T_C and T_L depend on the characteristics of the soil, being higher as the soil is more flexible. In the very long periods, the reduction of the spectral ordinate is interrupted not to minimize in excess the effect on tall buildings.

The spectral ordinates grow as the damping of the structure decreases; this is consistent with Figure 2-3, Figure 2-4, and Figure 2-5 with the interpretation that damping reduces the response

of the structure. The spectra proposed by the codes correspond generally to damping 5% since most of the buildings correspond to this level of damping.

The codes consider the ductility by reducing the force *F*, it is divided by the ductility coefficient (response reduction factor). In some cases, this operation is carried out of the spectrum, as shown in equation (2-9), but often it is incorporated into the spectrum by dividing their ordinates by that coefficient. In that way, there are two types of spectra, those in which the ordinates are not divided by any factor and those in which they have been divided by it. The first types are termed linear (or elastic) spectra and the second spectra are termed nonlinear. Obviously, the spectra shown in Figure 2-3 to Figure 2-7 are linear.

It should be noted that the absolute response acceleration spectra characterise the dynamic effect of a group of earthquakes in terms of forces (as represented in Figure 2-6 to Figure 2-7). This involves several drawbacks, first of all (and possibly one of the most important) the quantification of the severity of an earthquake in terms of the force *F* is only meaningful when the structure is maintained in elastic regime, since the more severe the earthquake, the greater the response acceleration and the internal forces; therefore, this is directly related to the resistance that must be provided to the structure. However, when the structure yields, the lateral force *F* is maintained essentially constant, hence, the internal forces are kept constant; therefore, the force ceases to be a valid parameter to characterise the dynamic effect of the earthquake. For example, even if the peak ground acceleration and/or the duration of a given input accelerogram is several times larger and/or longer than another one, if both earthquakes are severe enough to induce an inelastic response of the structure, both will produce approximately the same lateral force on the structure, while the response in terms of maximum displacements and damage can be completely different. The more severe the earthquake, the higher the structural damage and the maximum displacements; therefore, the damage cannot be characterised in terms of forces. In other words, there is a more direct correlation between damage and displacement comparing to the existing correlation between damage and force. The approaches "Relative displacement response spectra" and "Input energy response Spectra" are more suitable to high seismic risk zones and, can avoid this drawback. Since these zones are not within the scope of this research, these approaches are not included in this thesis.

2.1.3 Performance-based earthquake-resistant design

The objective of the current seismic design codes is to prepare the structure to resist the design seismic input only under ultimate limit state; in other words, the structure is intended to resist the design earthquake with an acceptable level of serious damage but without collapse (in other words, avoiding at all costs the loss of human lives). Remarkably, that approach does not include any requirement about the behavior under seismic actions with lower or higher level of severity; this contrasts with the usual strategy against another type of actions (gravity, for example) where two types of limit states (ultimate and service) are considered. This approach is broadly valid and has been used for decades but was in shortage especially after the Northridge earthquake in 1994 and Kobe in 1995; after these highly severe earthquakes it was found that some structures, even those relatively new and that had been designed to the latest seismic standards, did not collapse (and in them there were no human casualties), but the damage to buildings (both structural and non-structural) was very serious. In the Kobe earthquake, some hospitals had been so intensely reinforced that effectively its structure did not collapse but absolute accelerations in the building were so high that it damaged the installations and were unusable at the time of greatest need (a few hours after the earthquake). After these events, earthquake engineering was directed not only to prevent loss of human lives but also to quantify, reduce, and prevent the damage. Depending on the damage, we can accept when an earthquake occurs, different solutions can be proposed. This strategy is commonly known as "Performance Based Design"; it is mainly described in these references (FEMA 350, 2013; SEAOC, 1995; FEMA 356, 2000; FEMA 349, 2000; FEMA P58, 2018; Bertero et al., 1996). These documents present different seismic design methodologies oriented to control and to quantify the level of structural damage due to seismic actions and to design structures that do not exceed each of the corresponding levels.

Based on the structural and non-structural damage the following four levels of performance ("Performance States") (SEAOC, 1995) are defined:

- **Fully Operational**. Uninterrupted service. Negligible structural and non-structural damage.
- **Operational**. Most of the activities can be resumed immediately. The structure is safe and can be inhabited. The essential activities are maintained while the non-essential ones are interrupted. Repairs are necessary to resume the non-essential activities. Slight damage.
- **Life Safe**. Moderate damage, the structure remains safe. Some elements or components of the building may be protected to avoid damage. The risk of loss of life is low. The building may need to be evacuated after the earthquake. The repair is possible but can be economically unfeasible.
- **Near Collapse**. Severe damage, but without risk of collapse. Possible fall of non-structural elements.

More recently, another similar classification is considered (ATC 40, 1996; FEMA 349, 2000; FEMA 350, 2013; FEMA 356, 2000; FEMA 389, 2004; FEMA P58, 2018):

- **Immediate Occupancy**. Occupants' safety. Important services are not uninterrupted. Negligible structural damage. The global damage is minor. The period of lack of functionality ("down time") is about 14 hours.
- **Damage Control**. Slight structural damage. Achievable occupants' safety. The essential activities are repairable. Moderate overall damage. The period of lack of functionality ("down time") is about 2 or 3 weeks.
- **Life Safety**. Probable structural damage but no collapse. No risk from falling non-structural elements. The evacuation of the occupants can be done without risk. The possibility of the irreparable building.
- **Collapse Prevention**. Severe structural damage, with the risk of collapse. Likely fall of non-structural elements. The evacuation of the occupants may involve risk. Building likely irreparable.

These four levels are often represented by their initials: IO, DC, LS, and CP. The three levels IO, LS, and CP are the most used for seismic design; Figure 2-8 presents, in a graphical and easily understandable way, the practical significance of these levels and their relationship with the percentage of damage. The case "operational" in this case refers to a building without any damage. The European regulation (EN-1998, 2004) proposes a similar classification; the considered levels (are termed as limit states) are **Limited Damage** (LD), **Significant Damage** (SD) and **Near Collapse** (NC). The provided definitions show that LD, SD and NC correspond to IO, DC, LS and CP, respectively. In the Eurocode 8 (EN-1998, 2004), the correspondence between Limit States and return periods is: DL corresponds to 225 years, SD to 475 years, and NC to 2475 years. This consideration can be also extended to the American regulations; in other words, IO, LS and CP correspond to seismic events with 20%, 10% and 2% probability to be exceeded in 50 years, respectively. The document FEMA 356 (2000) contains a deeper description; three objectives are stated: Basic Safety, Enhanced and Limited. The Basic Safety Objective cares only for LS (475 years) and CP (2475 years). The Enhanced Objectives care for LS (475 years), CP (2475 years) and FO and IO (72, 225 or 475 years); also FO, IO or LS alone (2475 years). The Limited Objectives care for LS (475 years) or CP (2475 years); LS (72 or 225 years) and CP (72, 225 or 475 years).

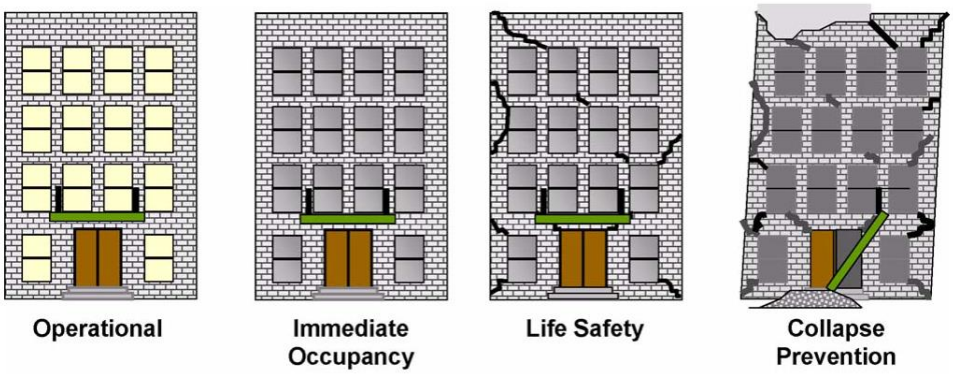

Figure 2-8. Damage levels (FEMA 389, 2004)

More specifically, for each structural type (i.e. moment-resistant concrete or steel frames, structural walls, concentrically braced concrete or steel frames, eccentrically braced steel frames, dual systems, inverted pendulum, etc.) more precise definitions of these levels have been developed depending on the type of experienced structural damage.

Regarding the seismic action, four levels of severity are defined as specified in Table 2-1.

Table 2-1 Severity levels of the seismic inputs

Design Earthquake	**Return Period (years)**	**Probability of Occurrence**
Frequent	43	50% in 30 years
Occasional	72	50% in 50 years
Rare	475	10% in 50 years
Very rare	970	10% in 100 years

Table 2-1 shows that the severity of the earthquakes is quantified in terms of their return period; it is understood as the average of the elapsed time among earthquakes with the same magnitude. In some cases, seismic actions more severe than those contained in Table 2-1 are considered; the so-called MCE ("Maximum Considered Earthquake") [Malhotra 2006] corresponds to a return period of about 2475 years (even 4975 years is considered in some singular cases). The relationship between the return period T and the probability p_n of being exceeded n years is given by the expression $T = -n/\ln(1 - p_n)$; it is often used to indicate the severity of an earthquake by the probability p_{50} to be exceeded in 50 years, for example, in the case of MCE is $p_{50} = 1 - e^{-\frac{50}{2475}} = 0.02$ and in the case of an earthquake "Rare" is $p_{50} = 1 - e^{-\frac{50}{475}} = 0.10$. Using the expression $T = 1 / (1 - (1 - p_n)^{1/n})$, similar results are obtained. The percentages stated in Table 2-1 have been obtained with these equations. As well, for $n = 1$ year, $1 / T = -\ln(1 - p_1) = p_1 + p_1^2 / 2 + p_1^3 / 3 + \ldots$; therefore, if the return period is sufficiently large, T is approximately equal to the inverse of the probability that a certain earthquake occurs in one year. If the alternative expression $(1 / T = 1 - (1 - p_n)^{1/n})$ is used, the identification is still more clear, since for $n = 1$, $1 / T = p$ is obtained. This property is commonly provided as an alternative definition of the return period of any event (not necessarily seismic). Table 2-2 displays the demand levels regarding each of the performance levels previously described (SEAOC, 1995) for the earthquakes that have the probability of occurrence specified in Table 2-1.

Table 2-2 Required levels of protection for each severity level of the seismic action (SEAOC, 1995)

Levels of the expected earthquake	**Level of required behavior**			
	Full Functionality	Functionality	Life Safety	Near Collapse
Frequent (43 years)			Unacceptable Behavior	
Occasional (72 years)				
Rare (475 years)				
Very Rare (970 years)				

Table 2-2 shows three levels of protection (expressed by the three represented diagonals): less intense for systems of moderate importance ("Basic Facilities"), more intense for major facilities ("Essential / Hazardous Facilities"), and even more intense for crucial facilities ("Safety Critical Facilities"). For example, in "Essential / Hazardous Facilities" (diagonal terms) it is required that for an earthquake of return period of 75 years the building remains fully operational, for an earthquake of return period of 475 years the building keeps operating in its major functions and for a return period of 970 years the building is able to preserve the lives of its occupants.

2.1.4 Nonlinear static analyses ("push-over")

2.1.4.1 Capacity curves

The method of earthquake-resistant design based on nonlinear static analyses consists basically of comparing the capacity of the structure, characterized by a **capacity curve** representing its behavior under pushing incremental forces, with the effect of the design earthquake, characterized by a **demanding spectrum**. The intersection between both curves is termed as "**target drift**" (or target displacement) or "performance point"; in other words, that point indicates the effect produced by the earthquake on the structure (ATC 40, 1996). The capacity curve is usually expressed by representing on the vertical axis (ordinates) the interaction force *F* between the building and the base (base shear, Figure 2-1) and on the horizontal axis (abscissae) the displacement of the top floor (Kircher et al., 1997; Krawinkler & Seneviratna, 1998) relative to the base. The analysis that generates this curve is static, monotonic, and obviously nonlinear, being commonly known as push-over. Figure 2-9 shows a capacity curve from a push-over analysis.

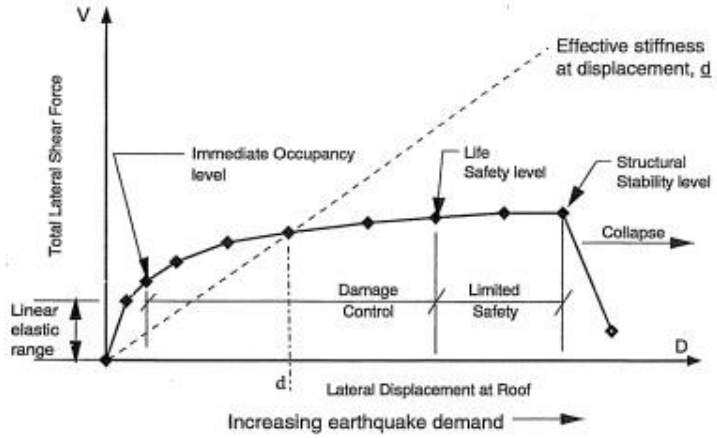

Figure 2-9. Capacity curve obtained from push-over analyses (ATC 40, 1996)

In Figure 2-9, *V* represents the interaction force between the building and the ground (base shear force) and *D* is the displacement of the upper floor. The correspondence between the values of *D* and the performance levels (IO, LS, CP) is also indicated.

In the push-over analyses, the base shear force is distributed along the floors according to certain patterns; the most used are the first modal shape, uniform or linear ("triangular") distributions. The push-over analyses are made incrementally, in other words, the lateral forces are increased progressively. For small values of *F*, the behavior of the structure is linear and as *F* increases, the structure becomes gradually more damaged; the stiffness of the structure decreases and its capacity curve becomes flatter. The smallest slope of the capacity curve with the increasing displacement clearly illustrates the elongation of the natural period of the structure.

Some researchers (Bracci et al., 1997; Fajfar & Fischinger, 1988; Gupta & Kunnath, 2000) have proposed techniques to modify the distribution of the lateral forces among the floors to consider the variation of the modal properties (mainly the first mode modal vector) by the increasing degradation of the structure. Other studies have proposed techniques to account for the contribution of the higher modes (Gupta & Kunnath, 2000; Paret et al., 1996), also (Birzhandi & Mirzakhani, 2023; Chopra & Goel, 2002; Goel & Chopra, 2005; Mao et al., 2008) have proposed a new formulation known as Modal Push-Over Analysis.

2.1.4.2 Target displacement

The demand is characterized by the design spectrum for the considered level of seismic action (Table 2-1); to be able to intersect it with the capacity curve, it is represented as the absolute acceleration spectrum S_a (vertical axis) vs. the relative displacement spectrum S_d (horizontal axis). This type of representation is commonly known as "Acceleration-Displacement Response Spectra" (SARD). Figure 2-10 shows some spectra plotted using different damping ratios; four radial lines are shown, representing four different fundamental periods (one line per each building).

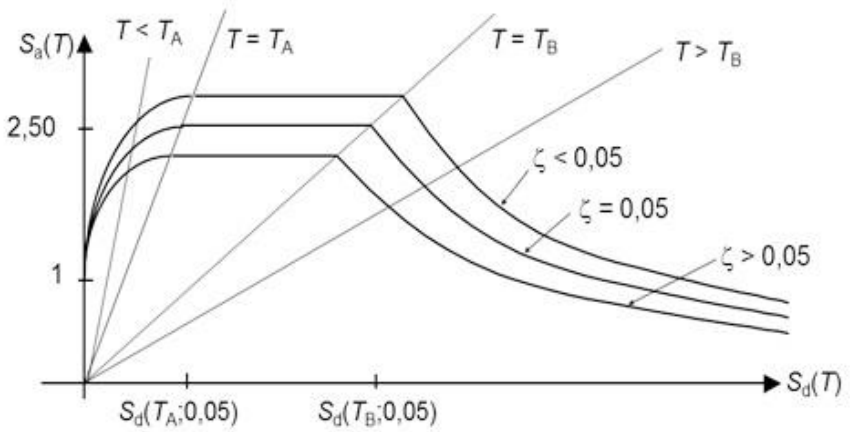

Figure 2-10. Acceleration spectra vs. displacement spectra

The methods mostly used to obtain the target displacements are:

- Capacity spectrum method (ATC 40, 1996).
- Displacement coefficient method (FEMA 356, 2000).
- Equivalent linearization method (FEMA 440 (ATC-55), 2005).
- Modified displacement coefficient method (FEMA 440 (ATC-55), 2005).
- Modified capacity spectrum (ATC 40, 1996).

Capacity Spectrum Method

In order to intersect the curves as shown in Figure 2-8 and Figure 2-9, they must be represented in the same coordinates. In this strategy (ATC 40, 1996), the capacity curve is modified as (Figure 2-8): the ordinate is divided by the part of the building mass that corresponds to its first mode (in other words, the equivalent modal mass divided by the total mass) [Clough, Penzien 1993; García Reyes 1998; Chopra 2012] and the abscissa is multiplied by the modal participation factor of the first mode [Clough, Penzien 1993; García Reyes 1998; Chopra 2012]. The capacity curve expressed in these coordinates is usually termed as a capacity spectrum. Obtaining a target displacement for each level of damage (characterised by design displacement, the horizontal axis of the spectrum of Figure 2-10) is performed in an iterative way according to the following process:

- To select the desired value for the design displacement and to find the corresponding acceleration determined by the spectrum in Figure 2-10.
- To determine, from the capacity curve, the horizontal force (on the vertical axis) that corresponds to the selected displacement. An equivalent bilinear plot will replace the curve between the origin and this point. The first branch of this plot coincides with the linear part of the capacity curve (from the origin) but extends beyond it. The second branch of this plot is similar to the actual capacity curve; it is selected with the provision that the areas bounded by the bilinear plot and the actual capacity curve (until the design displacement) are equal. Figure 2-11 shows an example of this process. Once the bilinear plot is generated, the equivalent viscous damping ζ_{eq} is determined; ζ_{eq} is selected (as usual, [Clough, Penzien 1993; García Reyes 1998; Chopra 2012]) by equalling the areas of the hysteresis loops for the bilinear plot and with viscous damping. This damping is added to the inherent damping in the structure, whose value is usually 5%.
- The acceleration-displacement spectrum is corrected to fit the value of ζ_{eq} obtained in the previous stage. The intersection between the corrected spectrum and the capacity curve (in the coordinates according to the formulation given in (ATC 40, 1996)) is determined. If the abscissa of this intersection is close to the selected displacement (with a predetermined

tolerance), the point corresponds to the target displacement. Otherwise, the process has to be repeated iteratively until a sufficient approximation is reached.

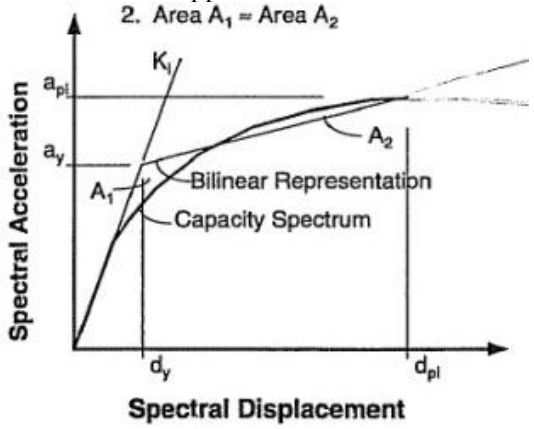

Figure 2-11. Bilinear approximation of the capacity curve (ATC 40, 1996)

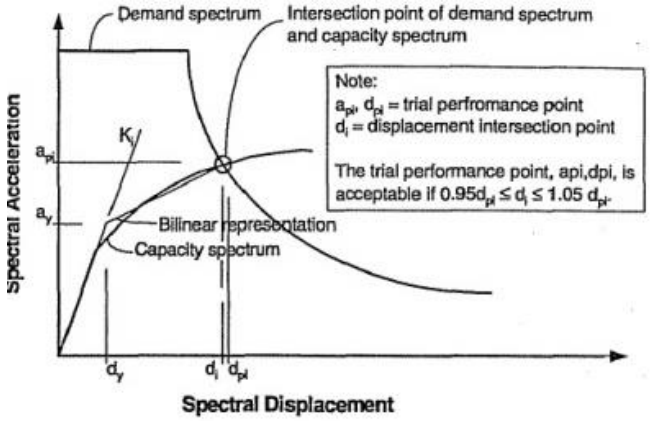

Figure 2-12. Obtaining the target displacement (ATC 40, 1996)

Figure 2-12 describes the iterative process for obtaining the target displacement.

Displacement Coefficient Method

This method uses the following empirical formula for calculating the target displacement:

$$\delta_t = C_0 C_1 C_2 C_3 S_a \frac{T_e^2}{4\pi^2} g \tag{2-10}$$

T_e is the effective fundamental period of the equivalent SDOF system, calculated using the bilinear approximation of the capacity curve (Figure 2-13):

$$T_e = T_i \sqrt{\frac{K_i}{K_e}} \tag{2-11}$$

T_i is the fundamental period calculated by an elastic dynamic analysis and K_i is the lateral stiffness. K_e is the effective lateral stiffness that is taken as the secant stiffness corresponding to a base shear force equal to 60% of the effective yield strength of the structure.

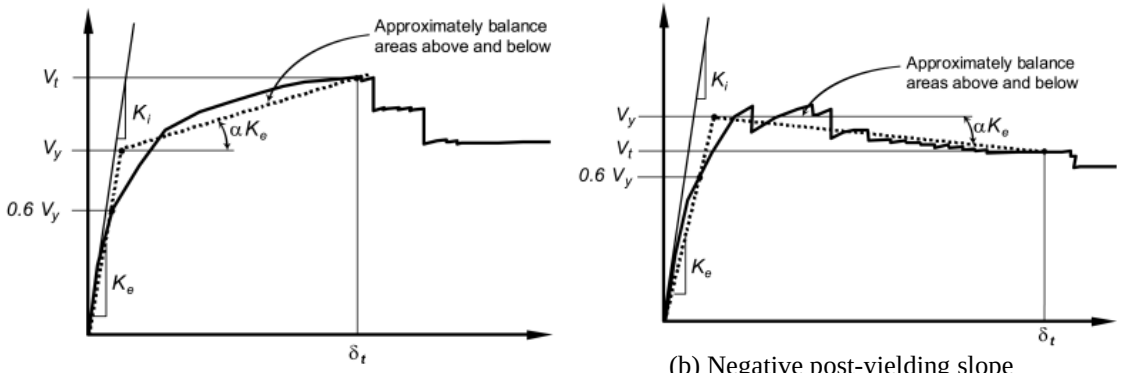

(a) Positive post-yielding slope

(b) Negative post-yielding slope

Figure 2-13. Idealized force-displacement curves (FEMA 356, 2000)

C_0 is a coefficient that relates the displacement of an equivalent single-degree-of-freedom system with the displacement on the roof of the building. Table 2-3 presents a way to obtain the values of C_0 (FEMA 356, 2000) as a function of the number of stories of the structure, the building type, and variation of the forces through the height obtained from the push-over analysis.

Table 2-3 Values for the modification factor C_0 (FEMA 356, 2000)

	Shear Buildings[2]		Other Buildings
Number of Stories	**Triangular Load Pattern (1.1, 1.2, 1.3)**	**Uniform Load Pattern (2.1)**	**Any Load Pattern**
1	1.0	1.0	1.0
2	1.2	1.15	1.2
3	1.2	1.2	1.3
5	1.3	1.2	1.4
10+	1.3	1.2	1.5

1. Linear interpolation shall be used to calculate intermediate values.
2. Buildings in which, for all stories, interstory drift decreases with increasing height.

In equation (2-10) C_1 is a modification factor that relates the expected inelastic displacements with those calculated for the linear elastic response: for $T_e \geq T_s$ is $C_1 = 1$ and for $T_e \geq T_s$ is $C_1 = [1 + (R - 1)T_S / T_e] / R$. T_s is the characteristic period of the response spectrum (transition between the branches of constant acceleration and constant velocity) and R is the ratio between the elastic and inelastic demands calculated by $R = [S_a / (V_y / W) / C_m]$ where V_y is the yield strength obtained from the idealized capacity curve, W is the weight of the building, and C_m is the equivalent modal mass participation factor of the first mode; alternately (FEMA 356, 2000) proposes a table ("Table 3.1") with approximate values

In equation (2-10) C_2 is a modification factor representing the effect of the shape of the hysteresis loops. Table 2-4 presents the values of C_2 (FEMA 356, 2000) depending on the level of damage, the type of frame, and the fundamental period of the building.

Table 2-4 Values for the modification factor C_2 (FEMA 356, 2000)

Structural Performance Level	$T \leq 0.1$ second[3]		$T \geq T_S$ second[3]	
	Framing Type 1[1]	Framing Type 2[2]	Framing Type 1[1]	Framing Type 2[2]
Immediate Occupancy	1.0	1.0	1.0	1.0
Life Safety	1.3	1.0	1.1	1.0
Collapse Prevention	1.5	1.0	1.2	1.0

1. Structures in which more than 30% of the story shear at any level is resisted by any combination of the following components, elements, or frames: ordinary moment-resisting frames, concentrically-braced frames, frames with partially-restrained connections, tension-only braces, unreinforced masonry walls, shear-critical, piers, and spandrels of reinforced concrete or masonry.
2. All frames not assigned to Framing Type 1.
3. Linear interpolation shall be used for intermediate values of T.

In equation (2-10) C_3 is a modification factor that represents the increment of displacement due to the second order effects. For buildings with positive post-yield stiffness (Figure 2-13(a)), C_3 is equal to 1 and for buildings with negative post-yield stiffness (Figure 2-13 (b)) C_3 is calculated as $C_3 = 1 + [|\alpha| (R - 1)^{3/2}] / T_e$. α is the ratio of post-yield stiffness to the effective elastic rigidity, with the relation of force-displacement (capacity curve) represented by a bilinear approximation (Figure 2-13). These operations must be carried out iteratively:

- Estimate a (Δ) value for the displacement. Make a bilinear approximation. Get K_e, T_e, and the ductility factor μ.
- Check the response spectra S_a (for a damping factor 5%) with the period T_e.
- From S_a obtain $H(m, S_a)$ and the displacement Δ.
- Get factors C_1, C_2, and C_3 and the scaled displacement $\Delta\ C_1\ C_2\ C_3$.
- Compare the scaled displacement Δ with its initial value, the iteration should continue until both are equal (with a prescribed tolerance).

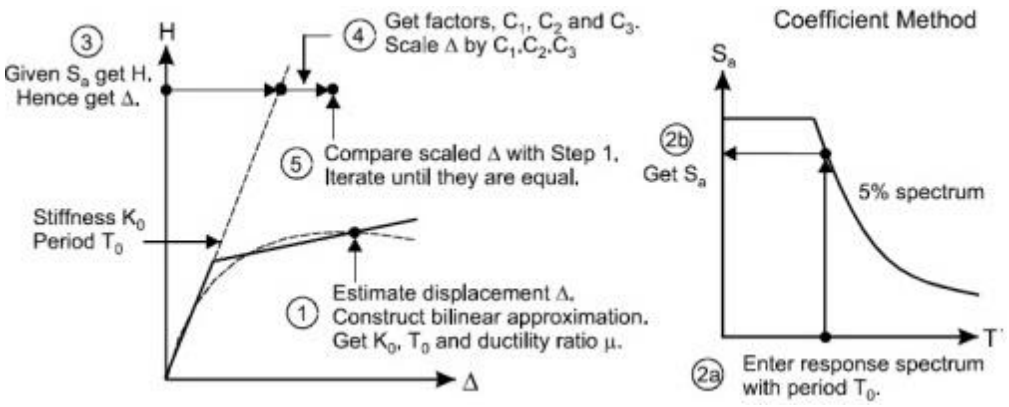

Figure 2-14. Iterative operations in the displacement coefficient method

Figure 2-14 describes the iterative process in the displacement coefficient method.

Linearization Method

The following operations should be performed iteratively (Figure 2-15):

- Estimate an initial value (Δ) for the displacement. Make a bilinear approximation. Get K_e, K_h, T_e, and the ductility factor μ.
- From K_e, K_h, T_e, and μ obtain the effective stiffness K_{eff}, the effective period T_{eff}, and the damping factor B_{eff}.
- Obtain the S_a ordinate of the response spectrum with the period T_e and the damping B_{eff}.
- From S_a obtain H (m S_a) and displacement Δ.
- Compare the scaled displacement Δ to the initial value; the iteration should continue until both are equal (with a prescribed tolerance).

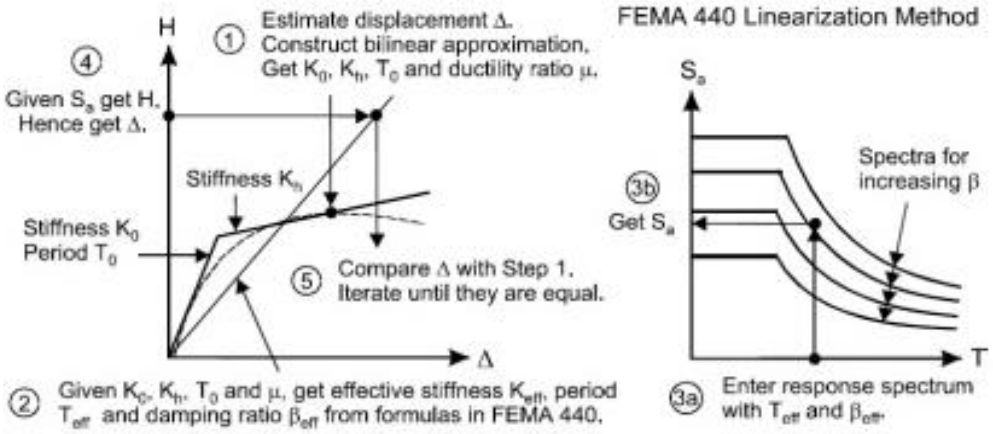

Figure 2-15. Iterative operations in the method of linearization

Figure 2-15 describes the iterative process in the linearization method.

Modified Displacement Coefficient Method

In modification of the displacement coefficient method (FEMA 440 (ATC-55), 2005), new expressions are proposed for the coefficients C_1 and C_2 and the coefficient C_3 is eliminated and replaced with a limitation of the maximum value of the resistance to avoid dynamic instability.

Modified Capacity Spectrum

The improved capacity spectrum method (ATC 40, 1996) determines the equivalent linear parameters, effective period T_{eff} and effective damping B_{eff}, by a statistical analysis that minimizes the extreme differences among the maximum response of an actual single-degree-of-freedom inelastic system and their equivalent linear counterpart (Guyader & Iwan, 2006).

2.2 Design philosophies and specifications for ECBP

EC3 and DG1 approach the strength design of ECBP similarly. The flexural and axial capacity of the ECBP subsystem is determined by the minimum between the following limit states: i) crushing of concrete or grout, ii) fracture of anchor-bolts, and iii) yielding of the plate; EC3 considers an additional limit state, the yielding of a portion of the column-flanges and web, termed "T-stub". Furthermore, the estimation of the resistance of the ECBP subsystem according to DG1 and EC3 is based on pre-assumed distributions of stress. While AISC contemplates either constant (rectangular, called RSB) or linear (triangular) stress-block under the compression zone of the steel plate, Eurocode contemplates a uniform stress-block just under the T-stub zone in compression. Both, the European and the American specifications, assume that tensile stress under the steel plates are concentrated in the anchor bolts.

2.2.1 American documents

This study focusses on the main procedure proposed by DG1, the RSB method. Figure 2-16 shows the three load scenarios for this stress distribution, as previously defined in the introduction: a) ZE, b) SM and c) HE. The crushing of concrete is characterized by Eq. (2-12), extracted from ACI 318 (2014).

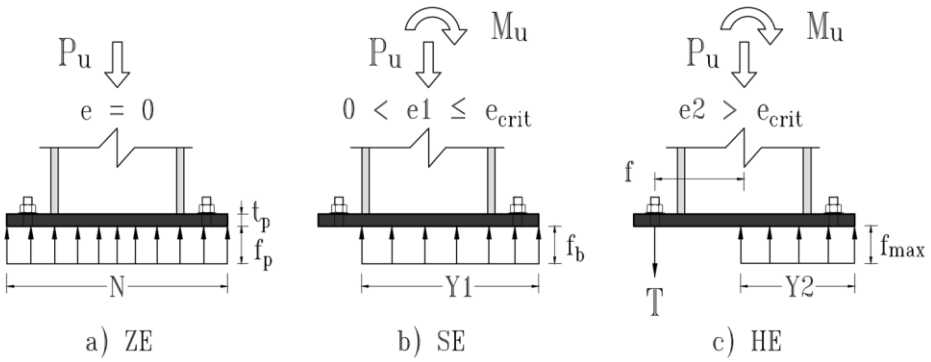

Figure 2-16. AISC stress distribution. RSB method

$$f_p < f_{max} \begin{cases} f_{max} = 0.85\, f'_c \\ f_p = \dfrac{P_u}{B\, N} \end{cases} \tag{2-12}$$

where f_p is the acting bearing stress in the concrete surface for ZE, f_{max} is the nominal concrete bearing strength, f'_c is the concrete compressive strength, P_u is the acting axial force, and B and N are the length and width of the steel plate projection. Regarding Figure 2-16a, the eccentricity e is calculated with Eq. (2-13).

$$e = M_u / P_u \begin{cases} \text{when } e \geq e_{crit},\ f_b = f_{max} \\ e_{crit} = \dfrac{N}{2} - \dfrac{P_u}{2\, B\, f_{max}} \end{cases} \tag{2-13}$$

where e_{crit} is the frontier between SE (Figure 2-16b) and HE (Figure 2-16c) behaviors, f_b is the acting bearing stress for SE and, M_u is the acting moment. The dimensions B and N are defined to avoid the crushing of concrete and the yielding of the steel plate. For ZE (Figure 2-16a), the bending moment in the steel plate M_{pl} can be calculated with Eq. (2-14).

$$M_{pl} = f_p \frac{l^2}{2} \tag{2-14}$$

$$l = \text{Max}\left[m = \frac{N - 0.95\, d}{2};\ n = \frac{B - 0.8\, b_f}{2};\ \lambda\, n' = \lambda \frac{\sqrt{d\ b_f}}{4} \right] \tag{2-15}$$

where l is defined in Eq. (2-15); m, d, n and b_f are graphically defined in Figure 2-17; λ is defined in Eq. (2-16); and; n' is defined as the cantilever-distance from the column web or column flange to the edge of the steel plate, according to the yield line theory.

$$\lambda = \frac{2\sqrt{X}}{1 + \sqrt{1 - X}};\ X = \left[\frac{4\, d\ b_f}{(d + b_f)^2} \right] \frac{P_u}{\phi_b\ P_{max}} \tag{2-16}$$

where P_{max} is the nominal concrete bearing-capacity force and ϕ_b is the strength reduction factor for bearing, using the Load and Resistance Factor Design (LRFD) method. This factor is equal to 0.65 per ACI 318 (2014). ϕ_b is considered as equal to 1 in this research, to compare the ECBP strength per ACI 318 (2014) results with the FEA results. The minimum thickness of plate for ZE $t_{mín}^{LS1}$ (Figure 2-16a) is described by Eq. (2-17).

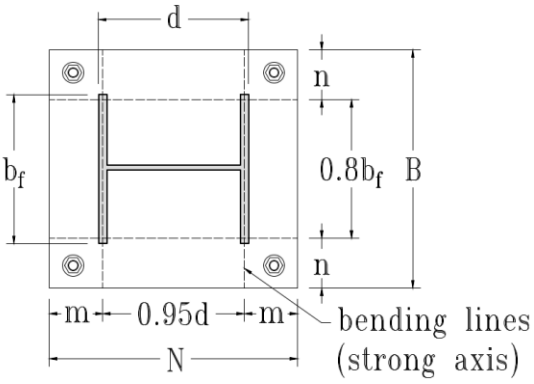

Figure 2-17. AISC assumed bending lines

$$t_{\text{mín}}^{\text{LS1}} = l\sqrt{\frac{2\,P_u}{\phi_f\;F_{yp}\;B\;N}} \tag{2-17}$$

where ϕ_f is the strength reduction factor for flexion and F_{yp} is the yielding stress of the plate. For SE (Figure 2-16b), the acting axial force and moment are only resisted by the uniformly distributed bearing load q (= f_b B). The resisting force for SE (Figure 2-16b) acts at the centroid of the bearing area. This is, at $Y1$ / 2 from the edge of the plate, thus $e1$ is given by Eq. (2-18). $Y1$ is the length of the bearing area for SE.

$$e1 = \frac{N}{2} - \frac{Y1}{2} \rightarrow Y1 = N - 2\;e1 \tag{2-18}$$

The critical eccentricity e_{crit} (Eq. (2-13)) can be re-written in terms of q, as shown in Eq. (2-19).

$$e_{crit} = \frac{N}{2} - \frac{P_u}{2\;q_{max}} \tag{2-19}$$

For SE (Figure 2-16b), f_b is calculated per Eq. (2-20).

$$f_b = \frac{P_u}{B\left(N - 2\;e1\right)} \tag{2-20}$$

Considering the principles of the mechanic of materials, the minimum thickness of plate for SE t_{min}^{LS2} is described by Eqs. (2-21) and (2-22).

$$t_{min}^{LS2} = 1.5\;m\sqrt{\frac{f_b}{F_{yp}}} \text{ for } Y1 \geq m \tag{2-21}$$

$$t_{min}^{LS2} = 2.11\sqrt{\frac{f_b\;Y1\left(m - \frac{Y1}{2}\right)}{F_{yp}}} \text{ for } Y1 < m \tag{2-22}$$

The acting force and moment for HE (Figure 2-16c) are resisted by combined action of bearing and tensile force in the bolts T. The force T is given by Eq. (2-23).

$$T = q_{max}\;Y2 - P_u \tag{2-23}$$

q_{max} (= B f_{max}) is the maximum value of q. The resultant bearing force for HE (Figure 2-16c) acts at the midpoint of bearing area. This is, at $Y2$ / 2 from the edge of the plate, with $Y2$ given by Eq. (2-24).

$$Y2 = \left(f + \frac{N}{2}\right) \pm \sqrt{\left(f + \frac{N}{2}\right)^2 - \frac{2\,P_u(e2 + f)}{q_{max}}} \tag{2-24}$$

where f is the distance from the centroid of a bolts group to the centerline of the column. $e2$ is the eccentricity for HE (Figure 2-16c). The minimum thickness of plate for HE $t_{mín}^{LS3}$ is given by Eq. (2-25).

$$t_{\text{mín}}^{\text{LS3}} = 2.11\sqrt{\frac{T\ x}{B\ F_{\text{yp}}}};\ x = f - \frac{d}{2} + \frac{t_{\text{f}}}{2} \tag{2-25}$$

where t_f is the thickness of the column flange. Alternatively, a triangular-stress-block distribution is allowed by DG1 (Fisher & Kloiber, 2006), which is not in the scope of this study. The results of Gómez *et al*. (Gomez et al., 2010) indicate that the RSB and triangular-stress-block methods predict similarly the strength of ECBP.

2.2.2 European standards

In EC3, for ZE, the T-stub area is the hatched area in Figure 2-18. $Z_{t,l}$ and $Z_{t,r}$ are the distances from the centerline of the column to the centroid of the left-group of anchor bolts, and to the centroid of the right-group of anchor bolts, respectively. Notice that there is a left T-stub formed in the left flange of the column, a Web T-stub and a right-flange T-stub. The axial capacity force of the ECBP $N_{j,rd}$ is determined by the sum of the resistances of all three individual T-stubs. $F_{c,Rd}$ is the resistance force of the concrete under an individual T-stub in compression (Eq. (2-26)).

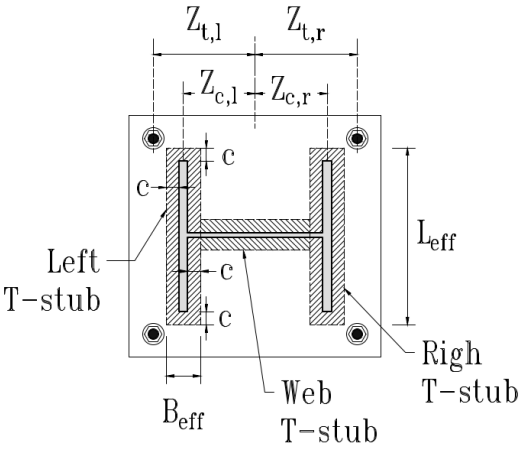

Figure 2-18. Definition of T-Stubs for ZE according to Eurocode

$$c = t_{\text{p}}\left(\frac{F_{\text{yp}}}{3\,f_{\text{jd}}\ \gamma_{\text{M0}}}\right)^{\frac{1}{2}};\ F_{\text{c,Rd}} = f_{\text{jd}}\ b_{\text{eff}}\ l_{\text{eff}} \tag{2-26}$$

where c, b_{eff} and l_{eff} are graphically defined in Figure 2-18. f_{jd} is the concrete bearing strength, which needs to be defined prior to the calculation of c (Eq. (2-26)) and thereupon, to be re-calculated by iteration. γ_{M0} is the partial safety factor for the material strength, which is considered as 1.0 in this research. Once $F_{c,Rd}$ is known, f_{jd} is re-calculated following Eq. (2-27).

$$f_{\text{jd}} = \beta_{\text{j}}\ F_{\text{Rdu}} \big/ \left(b_{\text{eff}}\ l_{\text{eff}}\right) \tag{2-27}$$

where β_j is a coefficient for the concrete of the pedestal, which may be taken as 2/3. F_{Rdu} is the Compressive resistance force of the T-stub area under the column flange, calculated as $f'_c\, b_{eff}\, l_{eff}$. For SE, all the area under the T-stub is under compression (Figure 2-19a and b). The magnitude of the flexural strength of the ECBP connection, $M_{j,Rd}$, for SE may be calculated with Eq. (2-28).

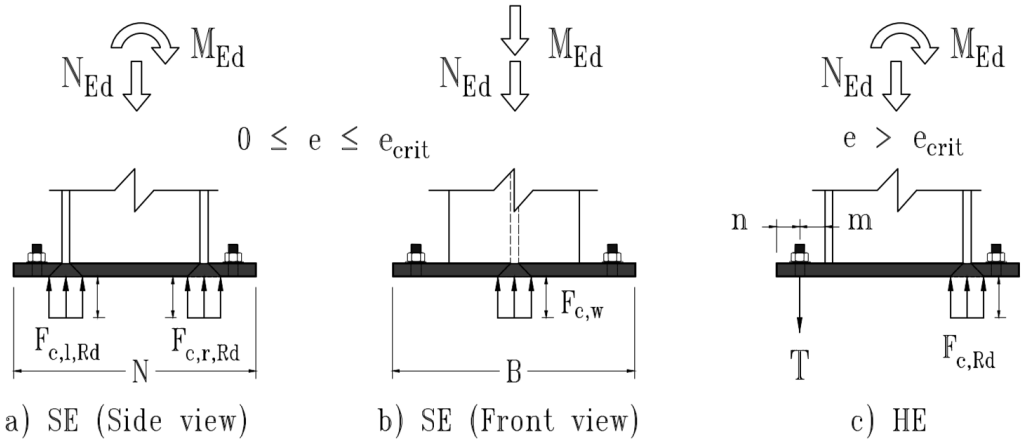

Figure 2-19. EC3 stress distribution. T-Stub method

$$M_{\mathrm{j,Rd}} = \mathrm{Min}\left[\frac{F_{\mathrm{C,l,Rd}}\ z}{\frac{z_{\mathrm{C,r}}}{e}+1};\ \frac{F_{\mathrm{C,r,Rd}}\ z}{\frac{z_{\mathrm{T,l}}}{e}-1}\right];\ z = z_{\mathrm{T,l}} + z_{\mathrm{C,r}} \tag{2-28}$$

where $F_{\mathrm{C,l,Rd}}$ and $F_{\mathrm{C,r,Rd}}$ are the compressive-resistance force of the left and the right side of the ECBP, in that order. These resistances shall be taken as the smallest value between the resistant force of the concrete in compression $F_{\mathrm{c,Rd}}$ (Eq. (2-26)) and the column T-stub in compression $F_{\mathrm{c,fc,Rd}}$ (Eq. (2-29)). $Z_{\mathrm{C,r}}$ and $Z_{\mathrm{T,l}}$ are graphically defined in Figure 2-18 and, represent the critical eccentricity e_{crit} that divides SE and HE.

$$F_{\mathrm{c,fc,Rd}} = M_{\mathrm{c,Rd}} \big/ \left(d - t_{\mathrm{f}}\right) \tag{2-29}$$

where $M_{\mathrm{c,Rd}}$ is the resisting-moment of the column, reduced to allow for shear interaction if necessary. The magnitude of $M_{\mathrm{j,Rd}}$ for HE (Figure 2-19c), may be calculated with Eq. (2-30).

$$M_{\mathrm{j,rd}} = \mathrm{Min}\left[\frac{F_{\mathrm{T,l,Rd}}\ z}{\frac{z_{\mathrm{C,r}}}{e}+1};\ \frac{F_{\mathrm{C,r,Rd}}\ z}{\frac{z_{\mathrm{T,l}}}{e}-1}\right] \tag{2-30}$$

where $F_{\mathrm{T,l,Rd}}$ is the resistant tensile force of the connection and, may be taken as the smallest value between the tensile strength of the left column T-stub $F_{\mathrm{t,wc,Rd}}$ (Eq. (2-31)) and the resistant force associated with the flexural yielding of the plate in the traction side of the connection $F_{\mathrm{t,pl,Rd}}$.

$$F_{\mathrm{t,w,Rd}} = \frac{\omega\ b_{\mathrm{eff,t,w}}\ t_{\mathrm{w}}\ F_{\mathrm{yc}}}{\gamma_{\mathrm{M0}}};\ b_{\mathrm{eff,t,w}} = t_{\mathrm{f}} + 2\sqrt{2}\ a_{\mathrm{b}} + 5\left(t_{\mathrm{f}} + s\right) \tag{2-31}$$

where ω is a reduction factor to allow for the interaction with shear in the column web, taken as 1.0 in this work; s is the corner radius of rolled steel sections; t_{w} is the thickness of the column web; F_{yc} is the yielding stress of the column; a_{b} is effective throat thickness of weld between the column and plate; $F_{\mathrm{t,pl,Rd}}$ may be calculated per Eq. (2-32).

$$F_{\mathrm{t,pl,Rd}} = \mathrm{Min}\left[\frac{4\ M_{\mathrm{pl,1,R_d}}}{m};\ \frac{2\ M_{\mathrm{pl,2,R_d}} + n\ \Sigma F_{\mathrm{t,Rd}}}{m+n};\ \Sigma F_{\mathrm{t,Rd}}\right] \tag{2-32}$$

where $F_{\mathrm{t,pl,Rd}}$ is calculated as the minimum of three modes of failure (Eq. (2-32). In the same order, mode 1 is the total yielding of the flange, mode 2 is the failure of bolts with yielding of the flange, and mode 3 is the bolts failure. $M_{\mathrm{pl,1,Rd}}$ and $M_{\mathrm{pl,2,Rd}}$ are given by Eq. (2-33). $F_{\mathrm{t,Rd}}$ is the resistant tensile force of a bolt, taken as its cross-area A_{b} multiplied by its ultimate stress F_{ub}. $l_{\mathrm{eff,1}}$ and $l_{\mathrm{eff,2}}$ are the effective lengths of the T-stubs for the failure modes 1 (complete yielding of the flange) and 2 (bolt failure with yielding of the flange), respectively; let these lengths be equal to B for practical purposes, based on experimental observations.

$$M_{\mathrm{pl,1,R_d}} = 0.25 \sum l_{\mathrm{eff,1}} \cdot t_{\mathrm{f}}^2 \; F_{\mathrm{yc}} \big/ \gamma_{\mathrm{M0}} \; ; \; M_{\mathrm{pl,2,R_d}} = 0.25 \sum l_{\mathrm{eff,2}} \; t_{\mathrm{f}}^2 \; F_{\mathrm{yc}} \big/ \gamma_{\mathrm{M0}} \tag{2-33}$$

3 INFLUENCE OF AXIAL COMPRESSION RATIOS IN RC COLUMNS ON THE SEISMIC RESPONSE OF MRF BUILDINGS

3.1 Introduction to this section

The Axial Compression Ratio (*ACR*) in Reinforced Concrete (RC) columns is defined in this thesis as the ratio between the nominal (i.e., unfactored) demanding axial force P caused by gravity forces only and the nominal axial capacity of concrete $f'_c A_g$; where f'_c is the concrete compressive strength and A_g is the gross sectional area. The Demand Capacity Ratio (*DCR*) is defined worldwide as the ratio between all the demanding factored (combination) internal forces (axial, shear, bending and torque) and the design sectional strength. *DCR* is a much more reliable and realistic index of structural strength, as the demand accounts for all the loads (gravity, wind, earthquake, etc.) and their combinations, and involves all the internal forces; regarding the sectional strength, it considers the steel reinforcement, the ϕ factor (or the material safety factors in the European regulations), and the interaction between the different internal forces. Noticeably, the difference between the information conveyed by *ACR* and *DCR* is higher when there is important seismicity. Consequently, many of the design codes do not limit *ACR*, but only *DCR*. Nevertheless, recommending bounds for *ACR* could save time, effort and money in early design stages. A more in-depth discussion of this topic is presented in the following paragraphs.

The breach of actual seismic codes and standards by several existing buildings has been noticed and studied by some authors worldwide (Abou-Elfath et al., 2017; Domínguez et al., 2016; Falcone et al., 2019; López-Almansa et al., 2013; Miano et al., 2022; Quintana Gallo et al., 2022; Requena-Garcia-Cruz et al., 2022; Tena-Colunga et al., 2022), and accordingly, the collapse risk of these buildings against earthquake occurrence (Aboutaha et al., 1999; Alfarah et al., 2020; Pampanin & Akguzel, 2011; Ricci et al., 2011; Singh Rawat, 2017) has also been noticed. Furthermore, there are RC columns in Moment-Resisting Frame (MRF) buildings having such high *ACR* values that undergo excessive *DCR*, still for vertical loads, as reported by a recent study (Villar-Salinas et al., 2021). Notwithstanding the collapse of either existing or new buildings with high *ACR* in columns is more probable than the collapse of non-earthquake-resistant buildings, a few codes do not specify explicit limits to *ACR* in RC columns of MRF. For instance, the American ACI 318-14 (2014), the New Zealander NZS 3101-1 (1995, 2006) and the Colombian NSR-10 (AIS, 2010); the following abbreviations ACI 318-14, NZS-95 and NSR-10 are respectively used henceforth for these codes. Some codes have recently limited the *ACR* in RC columns, mainly oriented to attain certain ductility-displacement capacities, in accordance with some experimental tests and numerical studies on individual subassemblies (Acun & Sucuoğlu, 2010; Elwood & Moehle, 2008; Y. Li & Yang, n.d.; R. Park, 1989; Rafaa Mahmood & Akram Gulam, 2017; Yao et al., 2019). For instance, the European EN 1998-1:2004 (EN-1998, 2004), the Chinese GB 50011-2010 (China Architecture & Building Press, 2010) and the Hong Konger HKBD-13 (2013) (hereinafter abbreviated as EC 8-04, GB-10 and HKB-13; respectively).

The *ACR* is called also Axial Load Ratio (ALR) or Normalized Axial Force (NAF). The *ACR* is a term widely used as indicatory of the modified flexural or shear-strength of columns (Villar-Salinas et al., 2021). Experimental tests on individual specimens and subassemblies show that high *ACR* in columns and walls, notably influence the inelastic seismic behavior of these elements

(Al-Osta et al., 2018; T. Chen et al., 2018; Su & Wong, 2007; Yang et al., 2022). Ductility and flexural strength of columns and walls with relative high *ACR* are reduced, due to the interaction of the axial load with bending moments (Z. Y. Chen et al., 2016; Y. J. Li & Liu, 2012; Yuen et al., 2016) and the increment of P-delta effects. Besides, it has been noticed that ductility of columns with high *ACR* is not increased, even if the spacing of confinement transversal reinforcement is reduced (Yuen et al., 2016).

For the purpose of retrofitting, the RC columns in MRF buildings with excessive *DCR* under service loads shall be provided with additional compressive strength as a priority, avoiding eventual demolitions and deformations of the existing structures during retrofitting, to secure the structural integrity and safety (Villar-Salinas et al., 2021). There are diverse retrofitting techniques like the addition of steel bracings (Nateghi-A, 1995), the adding of infill walls (Willam et al., 2010), jacketing with fiber reinforced polymers (FRP) (Abdelkerim et al., 2019; Al-Mahaidi & Kalfat, 2018; Azarm et al., 2017) or steel jacketing (Aboutaha et al., 1999; Islam & Hoque, 2015; Singh Rawat, 2017). However, some methods require axial deformation of columns to fully activate the confinement action (for instance, the jacketing with FRP) or require the construction of additional foundation or space availability, which are not feasible in most of the cases. The compressive, shear and the monotonic or hysteretic deformation (González Cuevas et al., 2007; Singh Rawat, 2017; Torabi & Maheri, 2017) capacity of individual retrofitted RC columns and isolated structures have been studied in the last decades. The retrofitting scheme for columns and joints proposed by Villar-Salinas et al. (2021) is described in subsection 3.3.2. It is feasible to reduce the *ACR* of RC columns in MRF, given its composite action that increment the compressive strength of columns by roughly 187%, and the flexural strength by 261%.

In this work, three existing MRF buildings with RC columns exhibiting high *DCR* in columns under vertical loads, are analyzed. One low-rise building and two mid-rise buildings located in a low seismic hazard zone. The columns with high *DCR* for each building, are retrofitted. Then, the original and the retrofitted-prototype buildings are subjected to Modal Response Spectrum Analysis (MRSA) and Modal Pushover Analysis (MPA), to evaluate the influence of the *ACR* on the global seismic response of the buildings.

3.2 Research methodology

The research approach begins with the selection of three actual 6 and 11-story RC MRF prototype buildings with high *DCR* in columns under service loads; these buildings are named as "original" and are described in subsection 3.3.1. Then, the columns with excessive *DCR* are retrofitted with steel jacketing; the buildings with these columns are named as "retrofitted" and are described in subsection 3.3.2. Once the original and retrofitted buildings have been defined, code-type MRSA are performed on them (subsection 3.4); these analyses correspond to low seismicity conditions and soil type D (according to the American regulations). The objective of the MRSAs on the original buildings is not to find out its seismic capacity (the *DCR* of some columns is exceeded even without seismic effects), but to establish relationships between *ACR*, *DCR* and story drift; this purpose also applies for the retrofitted buildings. Modal Pushover Analyses are performed on the original and retrofitted prototype buildings in order to corroborate and deepen the conclusions form the MRSAs; such studies are presented in subsection 3.5. Finally, subsections 3.6 and 3.7 contain seismic analyses of modified versions of the original prototype buildings; in subsection 3.6, the modifications consist in increasing the concrete strength, and in section 3.7, in reducing the number of stories N_s (until the *ACR* limits are fulfilled). Subsection 6.2 presents the conclusions of this study.

3.3 Prototype buildings (A, B, C)

3.3.1 Original buildings (AO, BO, CO)

Three original buildings were identified as buildings with high DCR in columns under service loads and selected as structural prototypes. The buildings are characterized with the following

properties. One six-story building was part of a recent study (Villar-Salinas et al., 2021), herein after referred to as building AO. Another two eleven-story buildings were selected as prototype buildings, named buildings BO and CO. The typical plans of the buildings are shown in Figure 3-1. Table 3-1 summarizes the reinforcement details and the cross-sectional dimensions of RC columns. The rebar diameter, area, ratio, spacing and confinement length of longitudinal and transversal reinforcement are provided in the table. In the table, "100/200" indicate that the transverse reinforcement is spaced at 100 mm in the confinement length and 200 mm in the unconfined one.

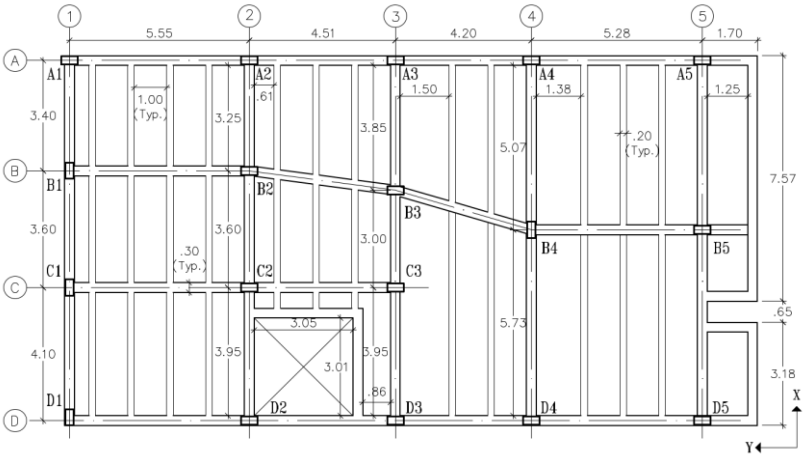

(a) AO

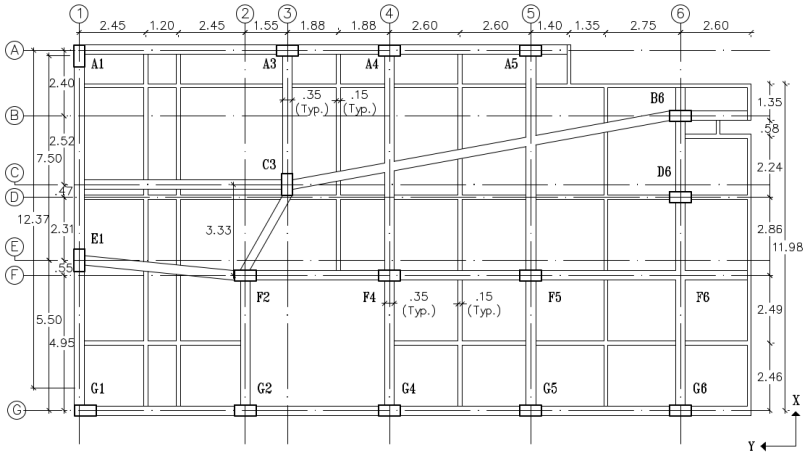

(b) BO

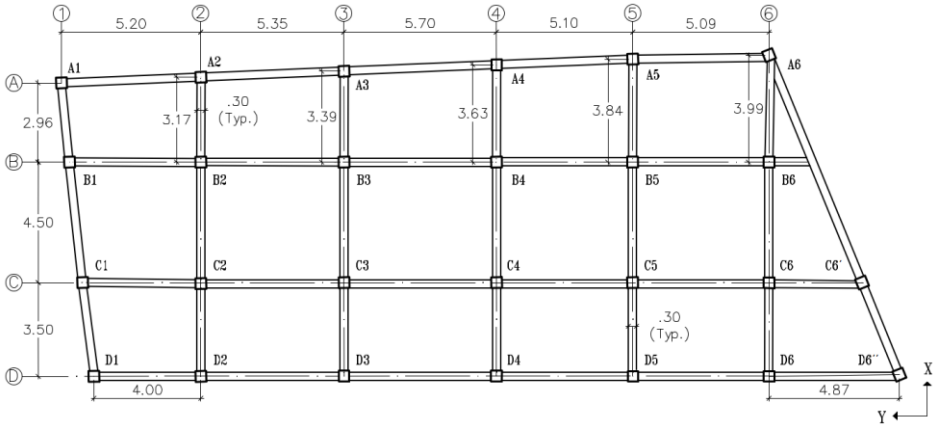

(c) CO

Figure 3-1. Typical story plan views of the original prototype buildings

Table 3-1 Dimensions and reinforcement details of RC columns, beams and joists of the original prototype buildings								
Building	Element Dimensions (mm)	Reinforcement						
		Longitudinal			Transverse			
		Rebar	Area (mm^2)	Ratio (%)	Rebar	Area (mm^2)	Spacing (mm)	Confinement length (mm)
Columns								
A	250 × 500	8ϕ19	2272	1.8	2ϕ9	142	100/200	500
B	400 × 800	16ϕ19	4544	1.4	3ϕ9	213	100/200	500
C	300 × 500	10ϕ19	2840	1.9	2ϕ9	142	100/200	500
Beams and joists								
A	300 × 300 (Beam)	2ϕ19 (Top) 2ϕ19 (Bot.)	567 567	0.63 0.63	2ϕ9	142	200	0
	200 × 300 (Joist)	2ϕ16 (Top) 2ϕ16 (Bot.)	402 402	0.66 0.66	2ϕ9	142	200	0
B	350 × 600 (Beam)	2ϕ25 (Top) 2ϕ25 (Bot.)	982 982	0.49 0.49	2ϕ9	142	200	0
	150 × 250 (Joist)	2ϕ19 (Top) 2ϕ19 (Bot.)	567 567	1.51 1.51	2ϕ9	142	200	0
C	300 × 400 (Beam)	2ϕ19 (Top) 2ϕ19 (Bot.)	567 567	0.47 0.47	2ϕ9	142	200	0

The elastic properties of materials were unified for the three prototype buildings. For the concrete, the unit weight (γ_c) is 24 kN/m^3, f'_c is 21 MPa and the Poisson ratio is 0.2. The properties of the reinforcing steel are in accordance with ASTM A615. The yield strength of reinforcing bars (f_{yst}) is 420 MPa and the modulus of elasticity of steel (E) is 200 GPa. The inelastic properties of materials are presented in subsection 3.5, which were taken into account in the stress-strain curves, modelled using the software SAP2000v19 (Computer and Structures Inc, 2016, 2017). The curve of the concrete was developed according to a non-linear uniaxial unconfined model (Benmokrane et al., 2000; Mander et al., 1988; Martínez-Rueda & Elnashai, 1997) for considering sub-standard construction practices. The curve of the longitudinal and transversal reinforcing steel was obtained with a simplified model of Ramberg-Osgood (Mander et al., 1988; Martínez-Rueda & Elnashai, 1997). Figure 3-2 shows the strain-stress curves of materials used.

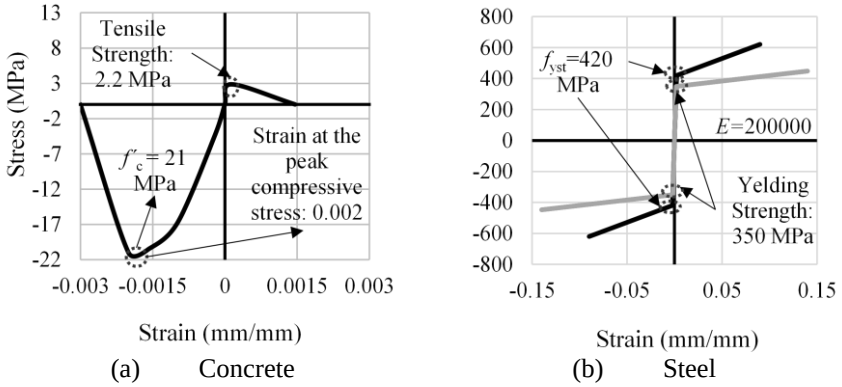

(a) Concrete (b) Steel

Figure 3-2. Material constitutive laws (stress-strain curves)

The dead load was set as 4.6 kPa, including the weight of story finishing and partitioning masonry walls. The self-weight load of frames and slabs were computed automatically by the software (Computer and Structures Inc, 2016, 2017); the thickness of slabs is 120 mm. The live loads were

defined as 1.8 kPa for living room areas, 5.0 kPa for balconies and 3.0 kPa for stairs. The lateral seismic loads are defined in subsections 3.4 and 3.5.

3.3.2 Retrofitted buildings (AR, BR, CR)

The retrofitting scheme proposed by Villar-Salinas et al. (2021) (Figure 3-3) showed good results in reducing the seismic story drifts and *DCR* values. Besides, the retrofitting improved the global ductility, the lateral strength, and in general, the seismic performance.

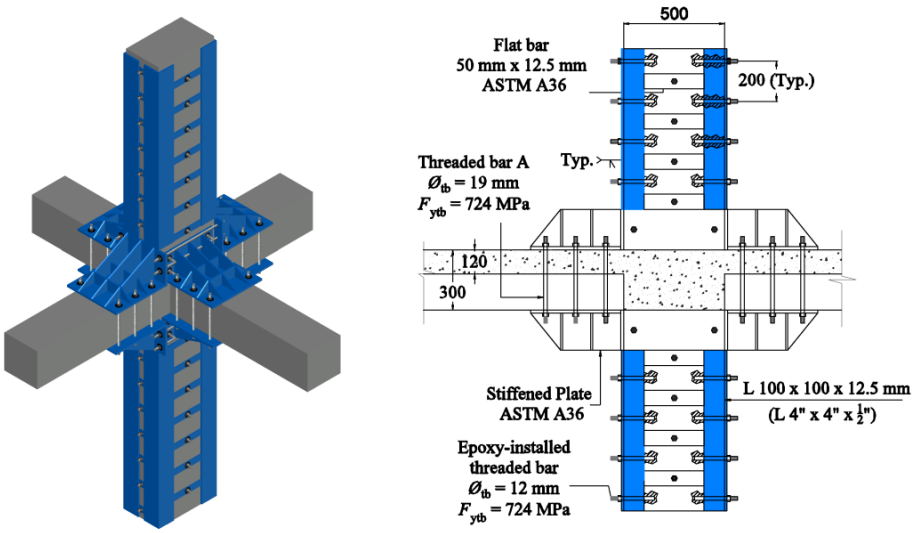

Figure 3-3. Retrofitting of columns with steel jacketing

The steel angles *type* ASTM A36 with cross section equal to 100 × 100 × 12.5 mm are located at the corners of the columns. Angles are welded along with 50 × 12.5 mm flat bars spaced at 200 mm center to center. The flat bars are epoxy anchored to the RC column along the long dimension of columns and drilled anchored in the short dimension. Additionally, stiffener steel plates are anchored to the column-beam joint zone, which are welded to the angles for continuity (Figure 3-3). The axial and flexural strengths of the columns were numerically obtained following the same procedure as detailed by Villar-Salinas et al. (2021). Namely, the axial strength of original columns and retrofitted columns were calculated with the analytical equations proposed by ACI 318-14 (2014) and NSR-10 (AIS, 2010) (equivalent to AISC 360-16 (2016)), respectively. On the other hand, the flexural strengths of these columns were modelled using a fiber section into the section builder tool of the software SAP 2000. It shall be noticed that the confining pressure of the steel jacketing was neglected to consider that an axial strain is needed to active this pressure, which is not safe for columns with high *ACR*. For further details and discussion, refer to (Villar-Salinas et al., 2021). The computed strengths denote a marked increment in the axial strength. Table 3-2 summarizes the increment in the axial and flexural strength of columns for buildings A, B and C.

Table 3-2. Increment in the axial and the flexural strength of columns with retrofitting

Building	Axial / Flexural strength of original columns (kN / kN-m)	Axial / Flexural strength of retrofitted columns (kN / kN-m)	Increment (%)
A	1533 / 153	4411 / 552	187 / 261
B	3675 / 426	7286 / 1018	98 / 138
C	1862 / 172	4792 / 557	157 / 223

3.4 Modal Response Spectrum Analysis of the original and retrofitted prototype buildings

3.4.1 General considerations

The MRSA is the method selected herein for the calculation of the story drifts, *ACR* and *DCR*. The 3D models for the structural analysis of the original and retrofitted buildings were developed with the software SAP2000v19 (Computer and Structures Inc, 2016, 2017), which applies the finite element method (FEM). The ground acceleration was considered as 0.1 g, related to a 10% probability of exceedance in 50 years, to represent a low seismic hazard ground motion according to NSR-10 (AIS, 2010). A "D" soil type was encompassed, which is featured by shear wave velocity varying between 180 m/s and 360 m/s, and SPT number N_{SPT} between 15 and 50. The design spectrum for the MRSA of the buildings is defined for the performance level named Life Safety (LS). In addition, for the MPA, the spectra for additional performance levels (Collapse Prevention, CP, and Immediate Occupancy, IO) are entailed, as detailed in subsection 3.5. Figure 3-4 summarizes the design spectra for MRSA and MPA, for brevity. The response modification factor (*R*) of prototype buildings A, B and C was reduced from 5.0 to 4.5 due to the structural irregularities defined in subsection 3.3. The seismic mass matches the dead load. The Eigen Vectors Method [41] was selected to determinate the fundamental vibration modes. The Square Root of the Sum of the Squares (SRSS) method [41] was chosen for the combination of vibration modes. Bidirectional seismic-loading effects were considered as 100% in one direction and 30% in the orthogonal one, as specified by most modern seismic codes. The P-delta effects were neglected, as the results for first and second order analyses are rather similar (Villar-Salinas et al., 2021).

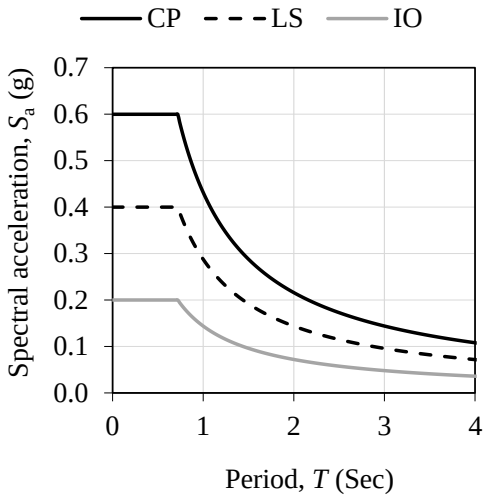

Figure 3-4. Design spectra for the analysis of the original and retrofitted buildings

The contribution of the first 12 modes have been considered, with more than the 93% of the total mass participating along each orthogonal direction. Table 3-3 summarizes the combined fundamental period (*T*) and the accumulated mass-participation-factors for each of the prototype buildings. The values for the first five (5) modes and the mode twelve (12) only are shown in the table for practical purposes.

Table 3-3. Accumulated mass-participation-factors for prototype buildings in X-Y axes (%)							
Building	*T* (sec.)	Mode					
		1	2	3	4	5	12
AO	1.56	66.6/0.1	66.8/80.8	82.5/80.9	90.8/80.9	90.8/81.3	98.3/95.5
AR	1.37	65.1/0.0	65.1/77.1	79.0/77.4	88.4/77.4	88.4/88.7	96.9/93.5
BO	1.67	77.9/1.3	80.2/54.5	80.2/79.2	90.4/79.5	90.7/86.5	96.5/94.7
BR	1.60	77.4/1.0	78.5/55.3	78.6/77.9	89.4/78.1	89.6/85.4	95.6/93.8
CO	1.92	75.9/3.6	78.5/68.0	79.7/79.3	89.0/79.6	89.2/88.6	94.6/94.9
CR	1.77	73.5/2.9	75.5/65.2	76.6/76.1	87.0/76.4	87.2/86.3	93.1/93.2

Figure 3-5 summarizes the modes shapes of the retrofitted and original buildings in the main orthogonal directions to indicate the influence of the retrofitting on the vibration modes.

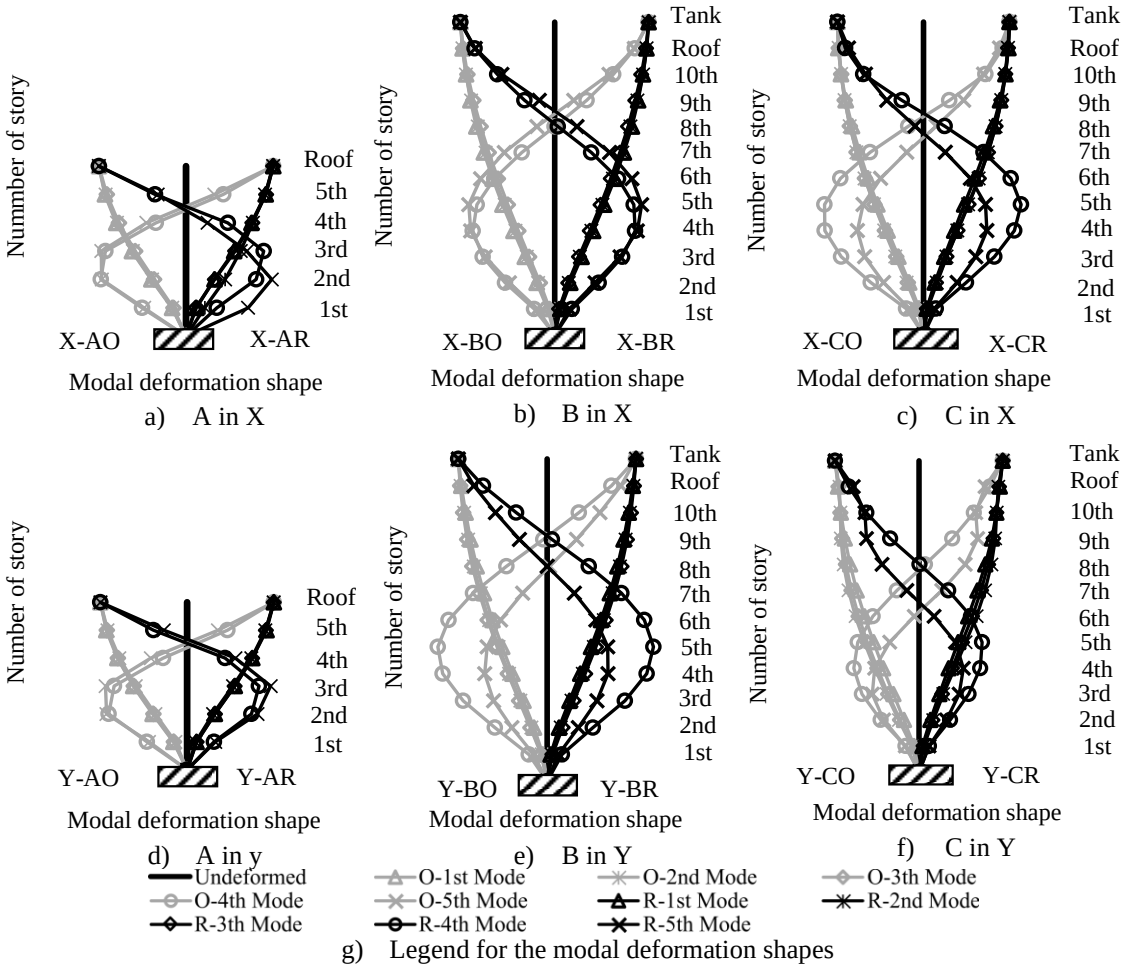

Figure 3-5. Mode shapes of the original and retrofitted buildings, normalized to the top displacement

3.4.2 MRSA of the original buildings

The beams and columns in the RC MRF of the prototype buildings were modelled by means of "frame type" elements, rigidly connected at joints and rigid diaphragm. The geometry and the elastic properties of materials were considered. Figure 3-6 shows the models of the original buildings AO, BO and CO.

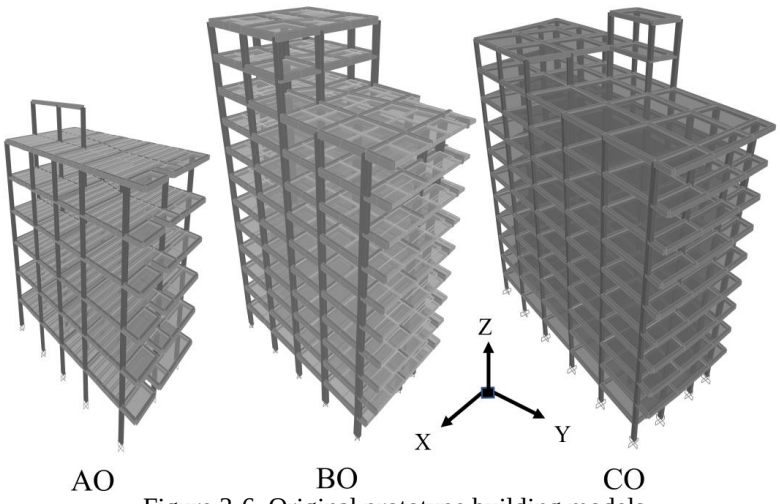

Figure 3-6. Original prototype building models

3.4.2.1 Story drifts

The inter-story drifts are calculated as a percentage, along the two main orthogonal directions X and Y; for AO, BO and CO. The limit on the story drifts prescribed by NSR-10 (AIS, 2010) is 1% for gross cross-sectional areas and shown in Figure 3-7. The series DRI-X-AO, DRI-X-BO and DRI-X-CO refer to drifts of AO, BO and CO along X respectively; and series DRI-Y-AO, DRI-Y-BO and DRI-Y-CO correspond to the drifts of the original buildings in Y. The drifts shown in Figure 3-7 for AO, BO and CO corresponds to the columns D5, B6 and D6'' (as defined in Figure 3-1), respectively, which have the critical values.

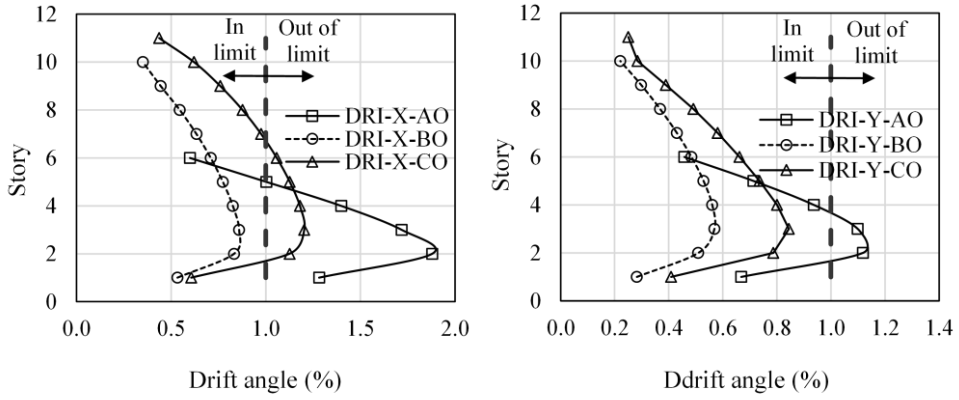

a) Direction X b) Direction Y

Figure 3-7. Maximum story drifts of the original buildings

It can be noticed in Figure 3-7 that, although AO is the low-rise building and drifts are commonly proportional to the height; it has the biggest drift along X (1.9%). It can be noted in Figure 3-1c that CO shows the most regular columns distribution in plan. In consequence, the irregularity in plan influences notably the seismic lateral drifts of the buildings. Building B is the only one that meets the limit on the drifts specified by NSR-10 (AIS, 2010) along both directions. It shall be considered also that the beams of building B (350 mm × 600 mm) are considerably stronger than the beams of buildings A (300 mm × 300 mm) and C (300 mm × 400 mm). Thereby, the stiffness of the beams also influences notably the story drifts of the prototype buildings.

3.4.2.2 ACR and DCR

The *DCR* is defined as the ratio between the required steel reinforcing ratio (ρ_{req}) and the provided steel reinforcing ratio (ρ_{prov}). Both ratios, ρ_{req} and ρ_{prov}, are equal to A_{st} / (b h), where A_{st} is the steel

reinforcing area and, *b* and *h* are the base and the height of the cross-sectional area of RC elements, respectively. NSR-10 (AIS, 2010) limits ρ_{prov} to values between 1 and 4% for columns. The maximum *DCR* per stories (DCR_{max}) of AO are shown in Figure 3-8a, differentiating the three load scenarios VSL, VFL and SEL. DCR_{max} values higher than 1 indicates that one or more columns on each story exceed the strength-limit states prescribed by code. Figure 3-8b and c show the DCR_{max} in the columns of BO and CO, respectively. The name of the series indicates the DCR_{max} according to the definitions provided.

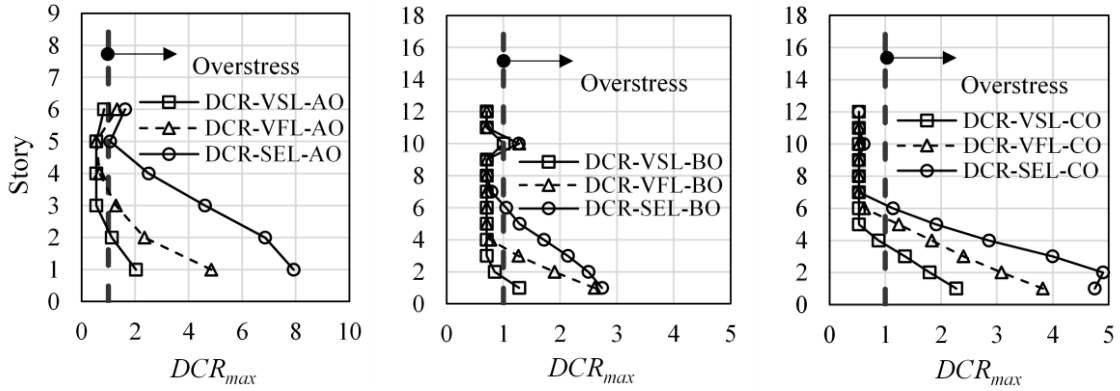

Figure 3-8. DCR in columns of the original prototype buildings

The codes and standards EC 8-04 (2004), GB-10 (2010), HKB-13 (2013) and NZS-06 (2006) define the limit to *ACR* unlikely. NSR-10 (2010) for concrete and ACI 318-08 (a previous version of ACI 318-14 (2014)) are basically similar, and do not stablish explicit limits to *ACR*. NZS-06 considers a load combination with service and partial seismic loads to limit the *ACR* explicitly, in terms of the axial capacity force $N_{n,max}$, which is a function of both materials, concrete and steel reinforcement, as per Eq. (3-1).

$$N_0^* \leq 0.7\,\phi\,N_{n,max} = 0.7\,\phi_a\,\alpha_1\,f'_c\left(A_g - A_{st}\right) + 0.7\,\phi_a\,f_{yst}\,A_{st} \tag{3-1}$$

where N_0^* is the acting axial force obtained from the structural analysis for vertical and lateral loads, ϕ_a is the strength reduction factor and α_1 is the Whitney stress-intensity factor (= 0.85). HKB-13 (2013) leads to an explicit limit on the *ACR* based on the concrete axial strength and non-seismic loads, as shown in Eq. (3-2).

$$N \leq 0.6\,A_g\,f'_c \tag{3-2}$$

where *N* is the required axial strength obtained from load combinations of the structural analysis, excepting seismic loads. The Chinese national standard GB-10 (2010) limits the *ACR* explicitly according with the Eq. (3-3). The GB-10 limits the *ACR* in terms of the concrete axial strength and load combinations including partial seismic loads.

$$\frac{N_{C,C}}{f_{c,GB}\,A_g} \leq \begin{Bmatrix} 0.65 & \text{(Grade I)} \\ 0.75 & \text{(Grade II)} \\ 0.85 & \text{(Grade III)} \\ 0.90 & \text{(Grade IV)} \end{Bmatrix} \tag{3-3}$$

where NC,C is the factored axial load for the column that includes gravity and seismic effects, $f_{c,GB}$ is the uniaxial concrete compressive strength ($\approx f'_c / 1.78$). Grades I-IV in Eq. (3-3) indicate the characteristics of ductility and detailing. The most rigorous design requirements correspond to grade I. EC 8-04 (2004) set the upper limits on the *ACR* in terms of ductility, the axial forces from seismic load combinations and design cylinder strength f_{cd}, as shown in Eq. (3-4).

$$\frac{N_{\mathrm{Ed}}}{f_{\mathrm{cd}}\,A_g} \leq \begin{Bmatrix} 0.55 & \mathrm{DCH} \\ 0.65 & \mathrm{DCM} \\ - & \mathrm{DCL} \end{Bmatrix} \tag{3-4}$$

where N_{Ed} is the factored axial force in the column that includes gravity and seismic effects, $f_{\mathrm{cd}} \approx f'_{\mathrm{c}} / 1.5$. DCH in Eq. (3-4) indicates a high ductility class for structures with the most stringent design requirements. DCM and DCL denote moderate and low ductility class, respectively, for structures with flexible requirements. The ACI 318-19 (the last version of ACI 318) still use the same formula (Eq. (3-5)) to limit the *ACR* in columns as ACI 318-14 (2014) and NSR-10 (2010), which is not an explicit limit. The axial compression is limited by the design resistance factors and the area of longitudinal reinforcement.

$$\frac{P_{\mathrm{u}}}{f'_{\mathrm{c}}\,A_{\mathrm{g}}} \leq \frac{\phi\,P_{\mathrm{n}}}{f'_{\mathrm{c}}\,A_{\mathrm{g}}} = \frac{0.85\,\phi\left[0.85\,f'_{\mathrm{c}}\left(A_{\mathrm{g}} - A_{\mathrm{st}}\right) + f_{\mathrm{y}}\,A_{\mathrm{st}}\right]}{f'_{\mathrm{c}}\,A_{\mathrm{g}}} \tag{3-5}$$

where P_{u} is the factored axial load from the analysis including all the load combinations for vertical and lateral loads. Given the differences in the way that design codes prescribe the upper limits to *ACR*, a re-normalization is needed to compare them, similar to that performed by Yuen et al. (2016). It shall be noticed that the codes or standards related in this chapter contemplates vertical and lateral loads for the *ACR*, excepting GB-10 (2010) that only contemplates service loads. In this research, the acting *ACR* values were calculated with service loads because the seismic effects on the axial loads can be beneficial in some cases, and it is common for consultant engineers to use *ACR* with service loads for pre-dimensioning at the initial stage of the structural design process. Therefore, there is no need to re-normalize the limits to *ACR* by means of the loads. On the other hand, the concrete compressive strength is affected by safety factors in some codes, as indicated in the description of Eqs. (3-1) to (3-5), thereby, a renormalization is made in terms of f'_{c}. Table 3-4 summarizes the re-normalized limits to *ACR* for AO, BO and CO.

Table 3-4. Re-normalized limits to ACR for original buildings

Code / Standard	NZS-06	HKB-13	GB-10	EC 8-04	ACI 318-14
Building	$\frac{N_0^*}{f'_{\mathrm{c}}\,A_{\mathrm{g}}}$	$\frac{N}{f'_{\mathrm{c}}\,A_{\mathrm{g}}}$	$\frac{N_{\mathrm{C,C}}}{f'_{\mathrm{c}}\,A_{\mathrm{g}}}$	$\frac{N_{\mathrm{ED,EC}}}{f'_{\mathrm{c}}\,A_{\mathrm{g}}}$	$\frac{P_{\mathrm{u}}}{f'_{\mathrm{c}}\,A_{\mathrm{g}}}$
Upper limit to ACR for AO	0.73	0.75	0.48 (G-III)	0.43 (DCM)	0.83
Upper limit to ACR for BO	0.68	0.75	0.48 (G-III)	0.43 (DCM)	0.78
Upper limit to ACR for CO	0.74	0.75	0.48 (G-III)	0.43 (DCM)	0.85

Figure 3-9 shows the maximum *ACR* (ACR_{max}) and the mean of the *ACR* (ACR_{mean}) in the columns of each story of AO, BO and CO. It shall be highlighted that the *ACR* in this study is evaluated for service loads. The *ACR* limits by EC 8-04 (2004), GB-10 (2010), NZS-06 (2006) and ACI 318-14 (2014) are also shown in the figure. The limits prescribed by HKB-13 (2013) and NSR-10 (2010) are not shown for practical purposes, considering also that they are similar to the limits by NZS-06 and ACI 318-14, respectively. The ACR_{max} of the building CO is higher than the upper limit prescribed by EC 8-04, from the first up to the sixth story (Figure 3-9c). The buildings AO and BO display values of ACR_{max} that are outlier from EC 8-04, from the first up to the third story (Figure 3-9a and c, respectively). Further discussion and analysis are presented in subsections 3.6.2 and 3.7.2.

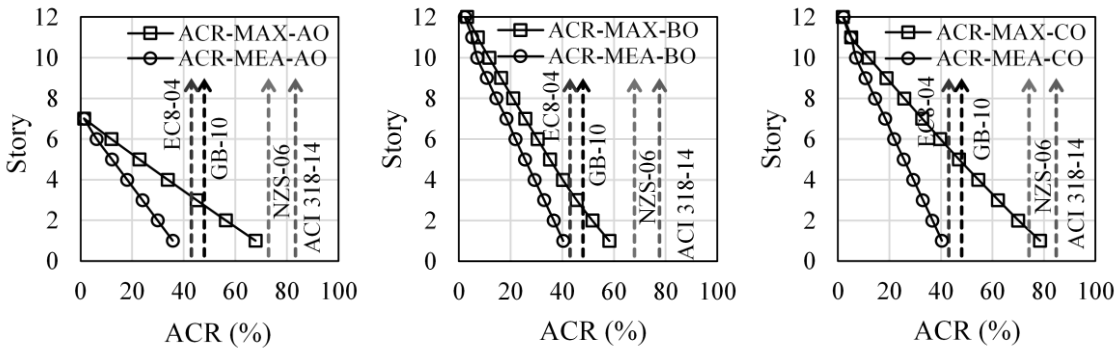

a) AO b) BO c) CO

Figure 3-9. ACR in columns of the original prototype buildings

3.4.3 MRSA of the retrofitted buildings

The MRSA of AO, BO and CO were used to set the number of columns to retrofit, which is equal to the number of columns with *DCR* greater than 1. Then, AR, BR and CR were also modelled in the software (Computer and Structures Inc, 2016, 2017) to obtain the story drifts, the *DCR*, and the *ACR* values to verify the effectiveness of the retrofitting for improving these indicators of the seismic performance. Table 3-5 summarizes the column labels (as defined in Figure 3-1) and the stories on which the retrofitting scheme (see Figure 3-3) was considered.

Table 3-5. Summary of the retrofitted columns in buildings AR, BR and CR

Prototype building	Retrofitted-columns labels	Number of retrofitted columns
AR	"A5, B5, D5 and B4: stories 1-4" "A4, B2 and C3: stories 1-2"; "D4: stories 1-2" "D2 and D3: story 1"; "B3, C2: stories 1-3" "D1: story 2"; "C1: stories 1-5"; "B1: stories 2-4"	16 6+2 2+6 1+5+3 (=41 in total)
BR	"G6: stories 1-3"; "B6: stories 1-2"; "D6: stories 1-3, 5-6" "F5: stories 1-5"; "A5: stories 1-4"; "F4: stories 1-4" "A4: stories 1-2"; "F2: stories 1-3"; "A3: stories 1-2" "C3: stories 1-3"; "E1: stories 1-2"	3+2+5 5+4+4 2+3+2 3+2 (=35 in total)
CR	“C1: stories 1-3”; “B1: stories 1-3”; “C2: stories 1-4” “B2: stories 1-5”; “A2: stories 1-2” “D3: story 1”; “C3: stories 1-4”; “B3: stories 1-5” “A3: stories 1-2”; “D4: stories 1-2”; “C4: stories 1-5” “B4: stories 1-5”; “A4: stories 1-3”; “D5: stories 1-3” “C5: stories 1-5”; “B5: stories 1-6”; “A5: stories 1-3” “D6: stories 1-3”; “C6: stories 1-4”; “B6: stories 1-5” “A6: stories 1-4”; “C’6: story 1”	3+3+4 5+2 1+4+5 2+2+5 5+3+3 5+6+3 3+4+5 4+1 (=78 in total)

3.4.3.1 Story drifts

Figure 3-10a and b show the maximum inter-story drifts of the retrofitted buildings along direction X and Y, respectively. It can be noticed in the figure that all the story drifts are within the limit by NSR-10 (2010) (equal to 1%) for AR, BR and CR.

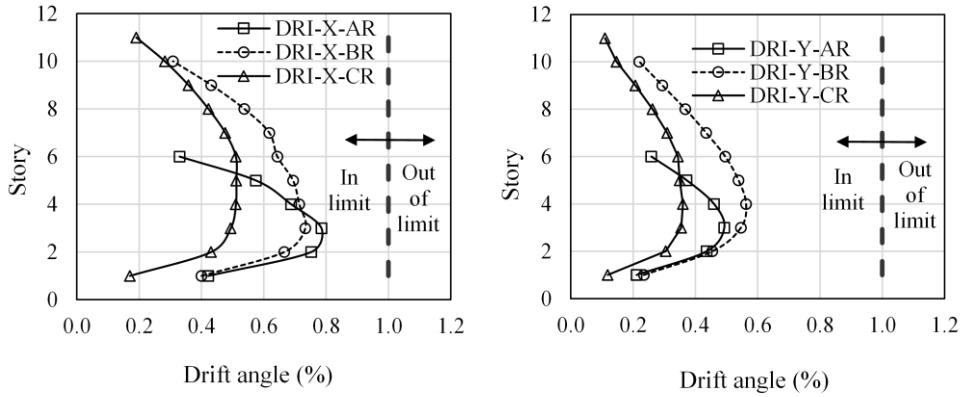

a) Direction X b) Direction Y

Figure 3-10. Maximum story drifts for AR, BR and CR along the main orthogonal directions

3.4.3.2 ACR and DCR

Figure 3-11 shows the values of DCR_{max} for AR, BR and CR under SEL combinations, which is the most critical scenario (series DCR-SEL-AR, DCR-SEL-BR and DCR-SEL-CR, respectively). It can be noticed in the figure that the retrofitting eliminates the overstress in all three buildings.

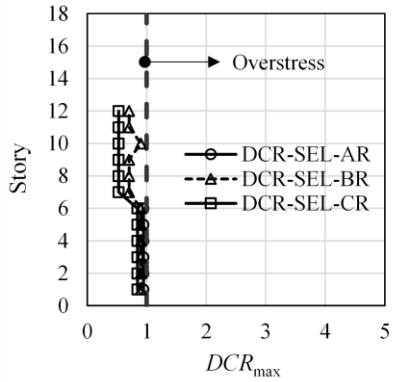

Figure 3-11. DCR in columns of the retrofitted prototype buildings AR, BR and CR

Figure 3-12 shows the ACR_{max} and ACR_{mean} for AR, BR and CR. The *ACR* limits prescribed by EC 8-04 (2004), GB-10 (2010), NZS-06 (2006) and ACI 318-14 (2014) are also shown in the figure. It shall be observed in the figure that BR (Figure 3-12b) and CR (Figure 3-12c) present columns with *ACR* higher than the upper limit prescribed by EC 8-04, on the first and two stories, respectively. It can be observed in Figure 3-12 that the *ACR* limits given by NZS-06 and ACI 318-14 for AR, BR and CR are different to those for AO, BO and CO. This is explained with the fact that the reinforcement ratio is included in the related equations to calculate the limits (Eqs. (3-1) and (3-5)). Subsections 3.6.2 and 3.7.2 include further analysis and discussion.

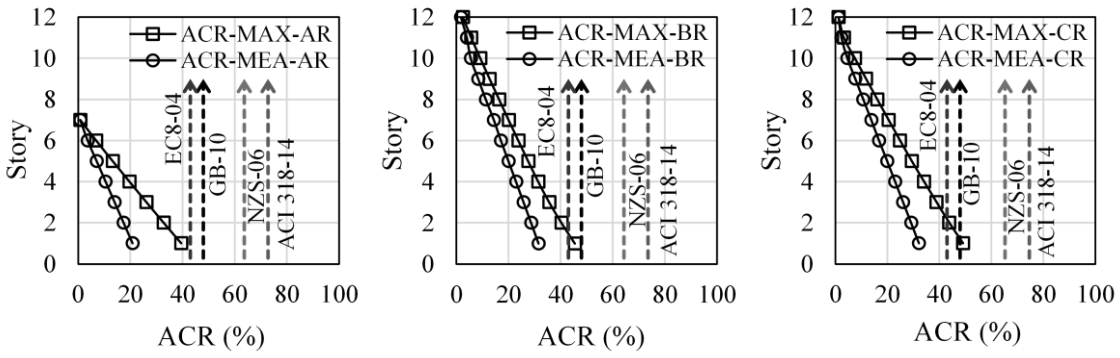

a) AR b) BR c) CR

Figure 3-12. ACR in columns of the retrofitted prototype buildings AR, BR and CR

3.5 Modal Pushover Analysis of the prototype original and retrofitted buildings

The assessment of the seismic performance of both the original and retrofitted buildings involves the non-lineal response of individual elements and the global system (Saborio-Romano et al., 2018), which represents a challenge in developing simple and practical analysis methods (Sheth et al., 2018). One of the most valued and studied method during the last decades is the Pushover Analysis (PA) (Cimellaro G. P. et al., 2014). An enhanced PA, named Modal Pushover Analysis (MPA), is chosen in this study to evaluate the seismic performance of buildings A, B and C. The MPA has shown important accuracy yet in higher modes (FEMA 440 (ATC-55), 2005; Han & Chopra, 2006; Yu et al., 2004) with a reasonable balance between accuracy and simplicity.

The plastic hinges of columns and beams are defined according to FEMA 440 (FEMA 440 (ATC-55), 2005) and ASCE 41 (ASCE/SEI 41-17, 2017), considering the flexural properties of beams and columns, which are obtained with Section Designer, built into the software (Computer and Structures Inc, 2016, 2017). The pushing load pattern used follows the shape of the combined-modal-response of the buildings, considering the contribution of the first 12 modes, similar to as defined for the MRSA in subsection 3.4.1. Figure 3-13 shows the normalized moment-rotation pattern for the columns of the prototype buildings, for different levels of ACR. It shall be noticed in the figure that the individual retrofitted columns can reach greater curvature and flexural moments than the individual original columns, which is caused by the action of the steel angles. The performance level considered for both the hinge properties of individual elements and the global structure are the conventional IO, LS and CP.

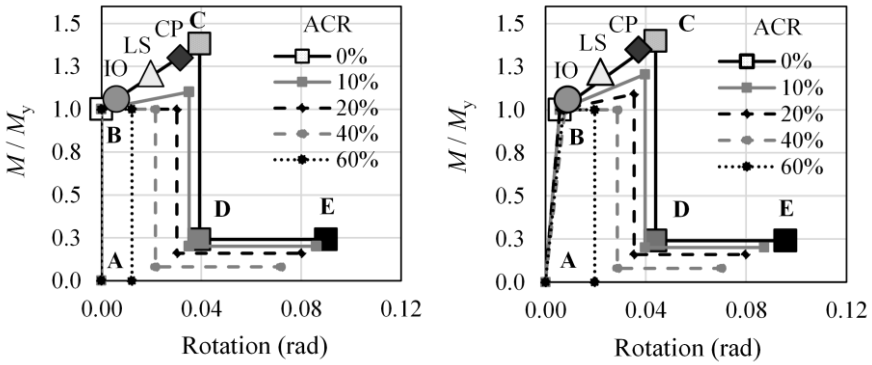

a) Original columns b) Retrofitted columns

Figure 3-13. Normalized plastic-hinge for the columns of the prototype buildings

The last loading step was controlled through the maximum horizontal roof-top displacements of 6% of the building's height. However, the convergence of the models failed in the case of a failure

mechanism before reaching the control maximum-displacement, as shown in the capacity curves in Figure 3-14. The lateral effects are represented as base shear coefficients, that is equal to the lateral loads divided by the seismic weight of buildings. The heights of buildings A, B and C are 19.6 m, 36 m and 35.5 m, respectively. The seismic weights are, in the same order, 13957, 35581 and 34198 kN.

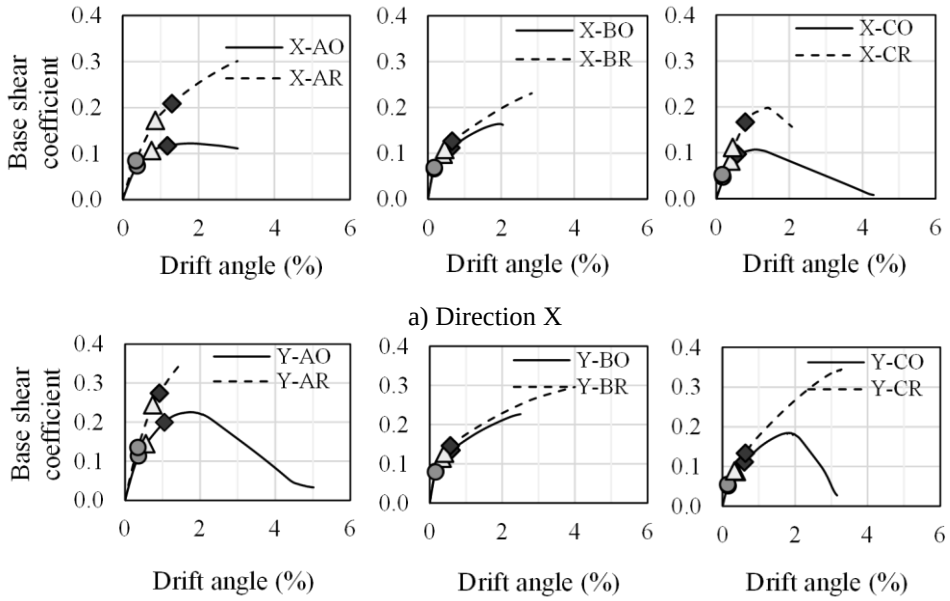

a) Direction X

b) Direction Y

Figure 3-14. Capacity curves of original and retrofitted buildings (○: IO, Δ: LS, ◊: CP)

The non-structural masonry-walls have not been considered in the models, given that the cooperation of these walls in the seismic response of the prototype buildings is not in the scope of this study. Other researches (López-Almansa et al., 2013) has accounted this cooperation and found that despite that the walls increase the lateral strength, are less ductile than the structure and thus, fails promptly. Besides, the non-reinforced masonry walls cause unexpected and inadequate hinges distribution on the RC MRF (Carrillo & González, 2007). The ground motions considered in this study to define the performance levels are similar to those defined by ASCE 7-16 (2017, p. 7) and most of the codes. The return periods for IO, LS and CP are defined as 2475, 475 and 225 years, respectively; which correspond to probabilities of exceedance of 2, 10 and 20% in 50 years (Tsompanakis, 2021). It shall be noticed that the ground seismic movements considered for the MRSA corresponds to a LS level.

The target drifts for IO, LS and CP shall correspond to intervals either equal or smaller than SD, MD and ED; in the same order (Pujades et al., 2012). Table 3-6 summarizes the adequacy of prototype buildings to reach the performance levels according to these damage intervals. In the table, "-" indicates that the correspondent capacity curve does not intersect the demand spectrum, and "Yes/No" means that a building satisfy/does not satisfy the related performance level.

Table 3-6. Seismic performance level of the original and retrofitted prototype buildings for the target drifts			
Building	Adequacy to performance levels to avoid excessive damage (X/Y Axes)		
	IO	LS	CP
AO	Yes/No	Yes/Yes	Yes/-
AR	Yes/Yes	Yes/Yes	Yes/Yes
BO	Yes/No	Yes/No	Yes/Yes
BR	Yes/No	Yes/Yes	Yes/Yes
CO	No/No	No/No	Yes/Yes
CR	No/No	No/Yes	Yes/Yes

Table 3-6 indicates that the retrofitting raises the damage capacity in one level for buildings B and C along Y-Axis (from CP to LS). The damage intervals in X-Axis basically remains unchanged with retrofitting scheme for the three buildings under study. These results can be explained if the relatively high flexibility of the buildings along X is considered, which is exposed by the drifts distribution in the original buildings (Figure 3-7). Figure 3-9 shows that the maximum ACR_{max} for CO, AO and BO are 78, 68 and 58%, respectively. As the definition of plastic hinges by ASCE 41 (ASCE/SEI 41-17, 2017) (Figure 3-13) considers the P-M interaction, the P-M-rotation levels of the prototype buildings are near to their ultimate capacity influenced by the high *ACR*. Consequently, the capacity curves Y-CO (Figure 3-14b) and X-AO (Figure 3-14a) show a rapid strength degradation when subjected to base shear coefficient of about 0.13, while X-BO and Y-BO (Figure 3-14a and b, respectively) holds a similar base shear coefficient without such degradation.

The lateral stiffness of the buildings can be calculated as the ratio of the base shear to the displacement. The analysis of the capacity curves in Figure 3-14 indicates that the lateral stiffness of AO, BO and CO is raised with the retrofitting by 30, 6 and 17% (on average), respectively (Table 3-7). It can be noted in the table and Figure 3-14 that the increment of the stiffness is higher for buildings AO and CO than for building BO, which is rational because building AO and CO expose greater *ACR* (Figure 3-9), *DCR* (Figure 3-8) and story drifts (Figure 3-7) than BO. Despite that BO shows *DCR* greater than 1 under service loads, its lateral behavior is governed by the geometry, principally in direction Y where the increment in the stiffness and lateral strength is relatively low.

Table 3-7. Elastic lateral-stiffness of the original and retrofitted buildings, K (kN / mm)									
Building	A			B			C		
Direction	AO	AR	Increment	BO	BR	Increment	CO	CR	Increment
X	14.4	20.5	30%	41.9	45.2	7.2%	21.7	27.7	22%
Y	22.2	31.4	30%	53.5	56.8	5.7%	33.8	38.1	11%
$\overline{X}$			30%			6.4%			16.5%

The response modification factor (*R*) of the three prototype buildings were taken as 4.5 to be used in the elastic MRSA. This value of *R* indicates a moderate ductility-capacity. Nevertheless, the capacity curves (Figure 3-14) do not match this assumption of the ductility for the seismic demands considered (LS per NSR-10 (2010)). The factor *R* for LS can be measured on the capacity curves as the ratio of the projected base shear obtained by extending the elastic line of the capacity curve for a LS target drift, to the base shear associated to the LS target drift. The capacity curves show that the behavior in direction Y is mostly elastic ($R = 1$) for the three prototype buildings to LS, where the maximum displacement is smaller than 0.05%. The values of *R* for LS measured from Figure 3-14 rounds between 1.1 and 2.4 for all the prototype buildings. The limit to *ACR* in columns is a parameter that might contribute to ensure an adequate structural performance of MRF buildings when elastic analysis (e.g., MRSA) is carried out given that *DCR* could be decreased. Alongside, the limit to *ACR* might motivate a proper structural behavior when

inelastic analysis (e.g., MPA) is performed because the damage capacity could be improved and, a brittle failure mechanism can be avoided.

3.6 Modal Response Spectrum Analysis of the buildings with higher concrete strength

3.6.1 Story drifts

The influence of f'_c on the story drifts has been recognized as insignificant by a previous research (Villar-Salinas et al., 2021) through a performance evaluation made on one building with similar characteristics to the building AO studied in this work. Therefore, for the purpose of this study (to show that *ACR* is a rather reliable indicator of the final strength *DCR*), the story drifts are not evaluated on the buildings with higher concrete. Instead of evaluating story drifts on these buildings, the relationships between *ACR*, *DCR* and story drifts are evaluated on: i) original buildings (see subsection 3.4.2), retrofitted buildings (see subsection 3.4.3) and buildings with less stories (see subsection 3.7).

3.6.2 ACR and DCR

A parametric analysis on the variability of the *ACR* and *DCR* with regard to f'_c of the original buildings is presented in this subsection, and the correlation between the *ACR* and *DCR* in the studied MRF buildings. The renormalized limits to *ACR* were calculated as summarized in Table 3-4. Eq. (3-4) shows that EC 8-04 (2004) does not specify a limit to *ACR* when low ductility-class buildings are considered. The limit to *ACR* by EC 8-04 for a medium ductility-class (43 %) is considered in this research to analyze the results. GB-10 (2010) sets a limit on *ACR* of 48 % for a structural grade III (Eq. (3-3)), which is near to the limit by EC 8-04. The limit by HKB-13 (2013) is the only standard considering an absolute limit (75 %), which does not depend on ductility class, longitudinal reinforcement or structural grade (Eq. (3-2)). The limits prescribed by NZS-06 (2006) and ACI 318-14 (2014) depend on the longitudinal reinforcement (Eqs. (3-1) and (3-5)). The limits by ACI 318-14 for the typical columns of AO, BO and CO are 83, 78 and 85%, respectively. NZS-06 set limits of 73, 68 and 74% for AO, BO and CO. Figure 3-15 shows the curves DCR_{max} vs. ACR_{max} evaluated for each story, this is, there are 6 coordinates for building AO and, 11 for BO and CO. Since logically the *ACR* is maximum on the lowest story, this story is represented at the right of each curve, where the values of *ACR* are maximum. This figure indicates that *ACR* is proportional to *DCR*, for AO, BO and CO. The limit to *DCR* is represented by a horizontal line, pointing out where the overstress state starts. The limit to *ACR* by codes under analysis are shown as vertical lines. Only the *ACR* limits by NZS-06 and ACI 318-14 for AO are displayed in Figure 3-15 for clarity.

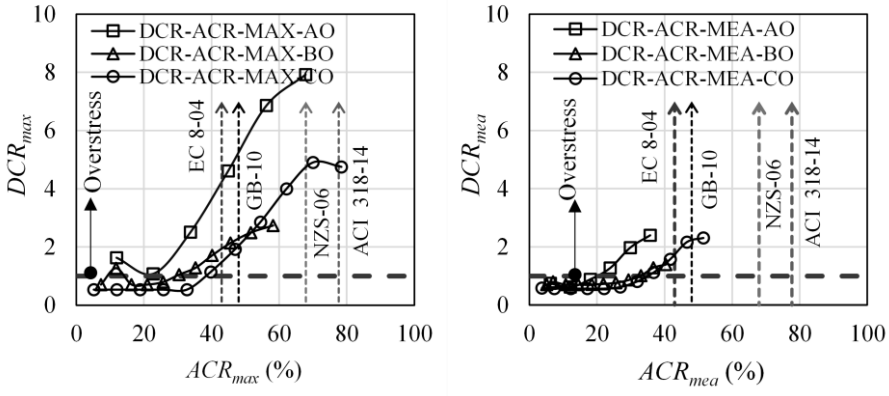

a) Maximum values b) Mean values

Figure 3-15. DCR vs ACR for each story of buildings AO, BO and CO

The parameter ACR_{mean} is not recommended as a reference to limit the axial compression in columns because the failure of just one column could cause the global or partial collapse of the structure. Therefore, it is recommended to use the ACR_{max} to check the limits, in order to warrant

that every column be in a reliable range of axial compression for structural safety. It can be observed in Figure 3-15 that the columns of BO get overstressed for *ACR* above 30% (DCR-ACR-MAX-BO). The columns of CO exceed the limit to DCR_{max} when ACR_{max} is near to 40% (Figure 3-15a). The plan irregularity of AO (Figure 3-1a) causes torsional seismic effects. Thereby, the influence of ACR_{max} on DCR_{max} is not clearly stablished for this building because the torsional effects alter the distribution of *DCR* values in the columns (DCR-ACR-MAX-AO in Figure 3-15a). Figure 3-15a shows that the DCR_{max} in the columns of AO exceeds the limit prescribed by ACI 318-14 (2014) when ACR_{max} is equal or greater than 20%.

Figure 3-8 shows that DCR_{max} increases nonlinearly from the top to the bottom of the original buildings, whereas *ACR* (both ACR_{max} and ACR_{mean}) grows linearly (Figure 3-9) from the top to the bottom. It can be noticed that, for all the three buildings AO, BO and CO, the ACR_{mean} values are lower than the upper limit by EC 8-04 (2004), the most stringent for the *ACR*. Figure 3-9a and b show that ACR_{max} in AO and BO fail to comply the limit by EC 8-04 from the first to the third story, the limit by GB-10 (2010) from the first to the second story, and, comply *ACR*-limits by ACI 318-14 (2014) and NZS-06 (2006). Figure 3-9c shows that ACR_{max} in CO fails to comply the limit by EC 8-04 from the first to the fifth story, the limit by GB-10 from the first to the fourth story, the limit by NZS-06 on the first story and is in-fulfilment of ACI 318-14. The ACR_{max} measured in the columns on the first story of AO, BO and CO are 68, 58 and 78%; respectively. Figure 3-8 shows overstress in columns of AO all along its height for SEL. The torsional effects influence this stress distribution. A trend of increasing DCR_{max} can be also observed for VFL and VSL. The overstress in some columns on the sixth story (B1, C1, D1 and D5) is caused by the effect of the P-M interaction. For instance, the tributary area of column B4 (Figure 3-1) is 25 m^2, a 5kPa of live load and is connected to an asymmetric beam, which influences on its overstress.

The proposed retrofitting shown in Figure 3-3 is a reasonable method to reduce the ACR_{max} and DCR_{max} in columns of existing RC MRF-buildings failing to comply strength-limits under service loads, given the important increment in the axial and the flexural capacity (Table 3-2). Figure 3-11 shows that the retrofitting reduces the DCR_{max} of AR, BR and CR down to an acceptable range (smaller than 1). Namely, the retrofitting eliminates the overstress in columns with strength-demand issues under VSL and SEL. Figure 3-12 shows a substantial reduction of ACR_{max} caused by the retrofitting. The ACR_{max} on the first story of AR, BR and CR (Figure 3-12) are 39 (reduced from 68%), 45 (reduced from 58%) and 48% (reduced from 78%), respectively. That is to say that retrofitting causes a reduction in ACR_{max} of 43, 22 and 49% for the prototype buildings A, B and C, respectively.

The concrete compressive strength f'_c is one of the most relevant and controversial inputs for the structural design and assessment of RC buildings, especially when it is obtained from core test results (Villar-Salinas et al., 2021). The influence of f'_c on the ACR_{max} is evaluated for the original buildings, parametrizing f'_c as 21, 28 and 35 MPa, as depicted in Figure 3-16.

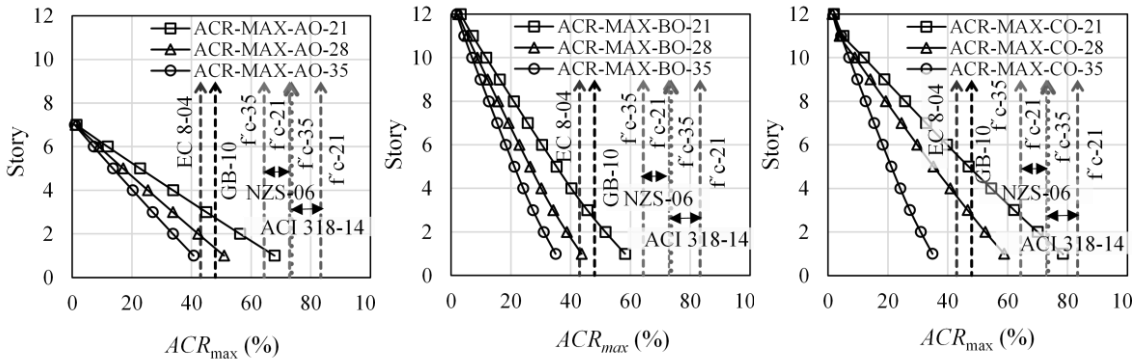

a) AO b) BO c) CO

Figure 3-16. Influence of f´c on ACR

Figure 3-16a shows that the ACR_{max} on the first story of AO for f'_c of 21, 28 and 35 MPa are 68, 51 (reduced by 20%) and 41% (reduced by 40%), respectively. It shall be noticed in the figure that the limits to *ACR* by NZS-06 (2006) and ACI 318-14 (2014) are specified as a range, because these limits depend on f'_c (Eqs. (3-1) and (3-5)). Analogically, it can be observed in Figure 3-16b that the ACR_{max} on the first story of BO are 58, 44 (reduced by 24%) and 35% (reduced by 40%). In addition, Figure 3-16c shows that the ACR_{max} on the first story of CO are 78, 59 (reduced by 24%) and 35% (reduced by 55%) for f'_c equal to 21, 28 and 35 MPa, respectively. Figure 3-16 shows that f'_c influences inversely the *ACR*. The raise of f'_c from 21 to 28 reduces the ACR_{max} in the columns on the first stories of AO, BO and CO by 40, 40 and 55%, respectively. These reductions bring about the compliment of the limit to *ACR* by EC 8-04 (2004), which is the most stringent code for the *ACR*. The increment of f'_c causes an important increase of the axial strength of the gross section of columns, equivalent to the reduction of the re-normalized *ACR* (40, 40 and 55%).

The original buildings studied fail to comply the *DCR* limit (equal to 1) predominantly due to the demand of flexural capacity for SEL; hence, the only increment of f'_c is not enough to eliminate the strength-demand issues and comply with all the NSR-10 (2010) requirements.

3.7 Modal Response Spectrum Analysis of the buildings without the top stories

3.7.1 Story drifts

The maximum story drifts of the three original buildings are reasonably greater along X-Axis than along Y-Axis, because the number of column axis for AO, BO and CO are less along direction X than along Y. The distribution of the drifts in the height is similar to the distribution displayed by most MRF systems. Figure 3-7 indicates that the maximum story drifts are located near to the third of the height, measured from the bottom. The buildings AO and CO do not comply with the limit of 1 % prescribed by NSR-10 (2010) for the drifts along X. The building CO does not comply with the limit for the drifts along Y, mainly because of the torsional effects of the seismic movements. The maximum drifts in X for AO, BO and CO are 1.9, 0.9 and 1.2%, respectively. In direction Y, the maximum drifts are 1.1, 0.6 and 0.8%, respectively. It shall be noticed that the flexural stiffness of the beams in BO is greater than the stiffness of the beams in AO and CO (Table 3-1), which influences the lateral drifts values.

Figure 3-10 demonstrates that the maximum drifts of AR, BR and CR get into the limit of 1% by NSR-10 (2010), both in X- and Y-Axis. The retrofitting shows a substantial reduction in the drifts of between 50 and 58% for the buildings AO and CO, in both directions X and Y. It can be noticed that these two buildings fail to comply with the limit of 1% without the retrofitting. Building BO is in compliment of the drift limit without the retrofitting and shows a lower reduction in the story drift by the retrofitting (of 22% along direction X). In direction Y, BO shows no significant reduction of drifts because the drifts are governed by the geometry in this direction more than by

the lateral stiffness. The distribution of the drifts in height for the retrofitted buildings follows a similar pattern to for original buildings, excepting that the maximum drifts occur one story higher for buildings A and C, due to the increment of stiffness in many columns of the bottom stories.

The direct comparison of the distributions of the ACR_{max} in Figure 3-9 and the story drifts in Figure 3-7, in the height of the original buildings, denote that ACR_{max} and story drifts are not directly related. This observation is consistent with the definition of both ACR_{max} and drifts. The story drifts are mainly dependent on the stiffness and geometry, while the total number of stories *N*s and the tributary area of the columns are variables that affects markedly the ACR_{max}. Additionally, Figure 3-17 shows the results of a parametric analysis on the maximum *N*s required for AO, BO and CO to fulfil the limit for the lateral story drifts prescribed by NSR-10 (2010) (1%), in order to determine the relationship between the ACR_{max} and drifts.

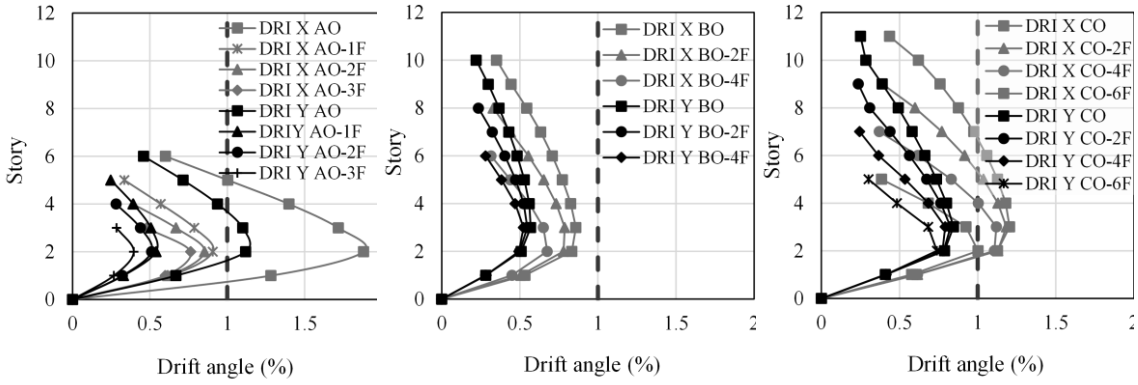

a) AO b) BO c) CO

Figure 3-17. Maximum number of stories for original buildings to fulfill the limits of story drifts

Figure 3-17 shows that AO might comply the limit to the drift prescribed by NSR-10 (2010) with five stories, this is one story less than the original *N*s. The buildings BO is already in fulfilment of the drift limit and CO could accomplish the drift limit of 1% only with *N*s equal to five. The significant reduction of the drifts of AO along X with the reduction of only one story, that is shown in Figure 3-17a, means that the torsional effects on AO decreased noticeably when reducing one story. The building BO shows no substantial reduction of the drifts, even reducing up to four stories, in direction Y mainly. Hence, the drifts of BO are governed by its geometry in plan and by the stiffness of its beams and columns. The analysis of the results in Figure 3-17c regarding CO indicates that there is a direct proportionality between the story drifts, DCR_{max} and ACR_{max}. For instance, CO could fulfil the drift limit with six stories less, whereas the same *N*s might be projected to comply the DCR_{max} (as shown in Figure 3-16c) and ACR_{max} (as shown in Figure 3-18c) limits. Therefore, for the case of the buildings studied in this research, columns with *ACR* under the upper limit by EC 8-04 (2004), eliminate the strength-demand issues, and comply the story drifts limit of 1 %. A previous research (Villar-Salinas et al., 2021) showed that the increment in f'_c from 21 to 35 MPa do not reduce the drifts substantially.

3.7.2 ACR and DCR

Another parametrization consists in calculating maximum *N*s of AO, BO and CO to comply with the *ACR* limit by EC 8-04 (2004) and the *DCR* limits by NSR-10 (2010). Figure 3-18 displays the ACR_{max} on each story of the original buildings and the mentioned parametric analysis. The series ACR MAX AO-3F indicates the ACR_{max} for building AO with three stories less than the original AO. The load definition for the buildings with a different *N*s follows the same criterion as that defined for the original buildings.

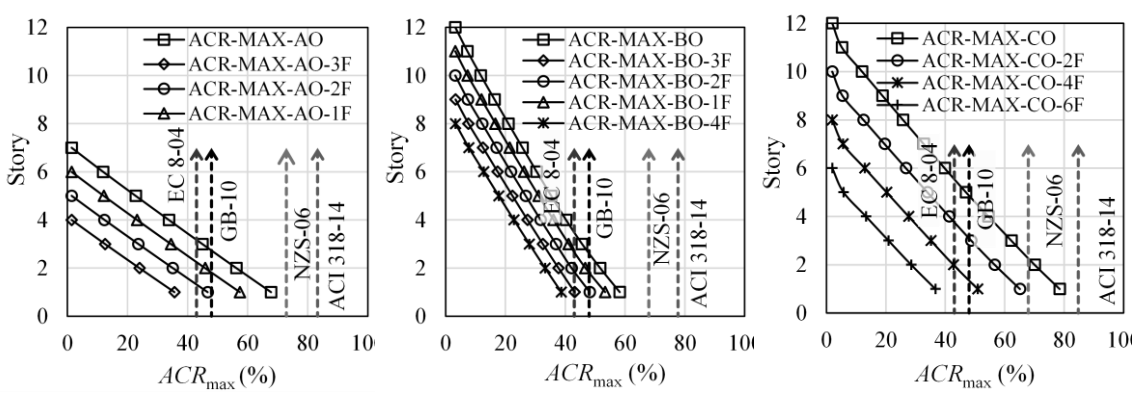

a) AO b) BO c) CO

Figure 3-18. Maximum number of stories for original buildings to comply the limits of ACR

Figure 3-18 indicates that AO could fulfil the limits to ACR_{max} by EC 8-04 (2004) with three stories only, this is, six stories minus 3 stories as per Figure 3-18a. A similar analysis for BO and CO shows that the ACR_{max} limits could be fulfilled with seven (eleven minus four) and five (eleven minus six) stories, respectively. The reduction of one story in the AO, BO and CO causes a decrease of 16, 9 and 8% in the ACR_{max}, respectively. This reduction is relatively low in comparison with the reduction caused by retrofitting and the increment of f'_c, as discussed before in this subsection. The reduction of *N*s, the selection of column dimensions, or the increment of f'_c may be useful mainly for the design stage, when these parameters still can be selected, prior to the construction phase. The effect of *ACR* and the retrofitting on the DCR_{max} are relevant for structural assessment. The number of columns with excessive DCR_{max} (for the seismic combinations) (*NC*) characterizes the number of columns to retrofit. Figure 3-19 summarizes a parametric analysis on *N*s required for AO, BO and CO to perform with DCR_{max} smaller than one in all the columns.

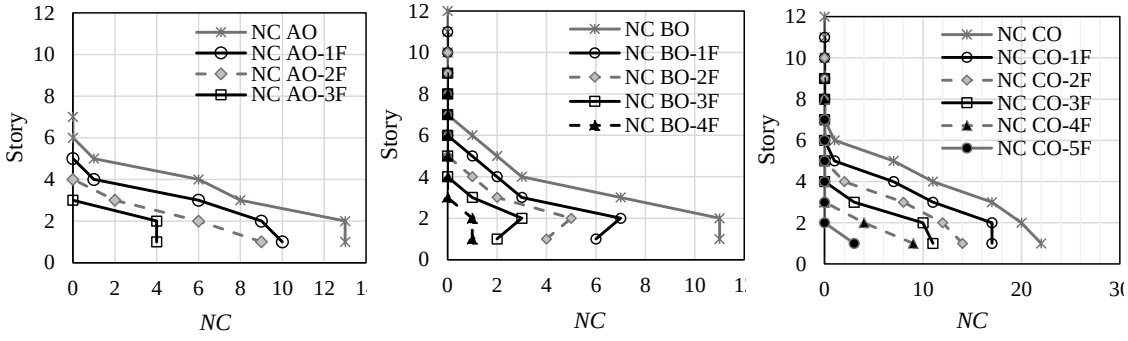

a) AO b) BO c) CO

Figure 3-19. Maximum number of stories for original buildings to comply the limits of DCR

Figure 3-19 shows that thirteen columns on the first story of AO are failing under SEL, and there are 41 columns with excessive DCR_{max} in total (NC-AO). The building AO consists of 108 column elements in the MRF structural system. There are 35 columns with excessive DCR_{max} (NC-BO) in the building BO and 178 column elements in the MRF structural system. The building CO exposes 78 columns with DCR_{max} higher than one (1) under SEL (NC-CO). The total number of columns in the MRF of CO is 276. Figure 3-19a indicates that eight (8) columns of AO would be overstressed with two stories less (NC AO-3F). The results in Figure 3-19a indicates that the reduction of one story in AO cause a reduction of 27% in the DCR_{max}, on average. The building AO could only hold up two stories to avoid excessive DCR_{max} at all. A similar analysis on BO and CO suggests that the reduction of one story in the height of these buildings generates a reduction of 29 and 25% in the DCR_{max}, on average, respectively. The reduction of *N*s of buildings

generates a reduction in the vertical loads and the seismic mass. Therefore, the shear and flexural stress in the columns decrease. The BO and CO could sustain six and five stories only to prevent excessive DCR_{max}, respectively.

Figure 3-8a shows that DCR_{max} values in AO are 7.92 for SEL and 2.03 for VSL, which means overstress factors of 792 and 203%, respectively. The relationship between the DCR_{max} for SEL and VSL is equal to 3.9. The required steel-reinforcement-ratio (ρ_{req}) for AO and CO is calculated as 14 and 9%, respectively, which are not accepted by mostly earthquake-resistant codes to avoid over-reinforced sections and consequently, fragile failures. The upper limit to the provided steel-reinforcement-ratio (ρ_{prov}) by NSR-10 (2010) is 4%. Figure 3-8b shows that, for BO, the DCR_{max} for SEL and VSL are 2.73 and 1.28, respectively. These values of DCR_{max} conduct to a ratio between the DCR_{max} for SEL and VSL of 2.1. Figure 3-8c shows that the DCR_{max} in CO is 4.90 for SEL and 2.27 for VSL, which means a ratio between the DCR_{max} for SEL and VSL of 2.2.

In accordance with the previous analysis of results in this subsection, it can be synthetized that the DCR_{max} in the columns of all three buildings are greater than one (1) under VSL. Besides, the torsional irregularity in AO influences its DCR_{max} markedly. While the ratios DCR_{max}-for-SEL/ DCR_{max}-for-VSL in BO and CO are near to 2, this ratio is roughly 4 in AO, because the torsional effects are critical for this building. Figure 3-9a evidence that BO is the building with the lowest calculated ACR_{max} (58%), and consistently, BO is the prototype building with the smallest DCR_{max} for SEL. On the other hand, Figure 3-9c points out that CO is the building with the highest calculated ACR_{max} (78%), and consistently, CO is building with the greatest DCR_{max} for SEL. Hence, the *ACR* is directly related to the seismic performance measured from the *DCR* values obtained from the MRSA.

4 NUMERICAL ANALYSIS OF THE MOMENT-AXIAL LOAD INTERACTION IN EXPOSED COLUMN-BASE PLATES

4.1 Introduction to this section

Exposed Column Base Plate (ECBP) connections have increasingly been recognized as highly relevant for the global structural behavior of Steel Moment Resisting Frames (SMRF) (Ermopoulos & Michaltsos, 1998; Fasaee et al., 2018; Grauvilardell et al., 2005; Khodaie et al., 2012; Torres-Rodas et al., 2022; Tsavdaridis et al., 2015; Zareian & Kanvinde, 2013). The Exposed Column Base Plate (ECBP) type is widely used in low-rise SMRF buildings (Aviram et al., 2010; Choi & Choi, 2013; Kavoura et al., 2017; D.-Y. Lee et al., 2008; Song et al., 2021; Torres Rodas et al., 2016); this base joint involves several components (e.g., grout pad, concrete foundation, anchor bolts, steel plate, column, and stiffeners) whose interaction defines the strength of these joints. Therefore, it is overly complex to predict the strength of ECBP including all these variables into an accurate model (A. M. Kanvinde et al., 2013). Consequently, the classical approach for the strength design of the connections, according to either American or European standards, is associated with the critical failure of any individual component of the ECBP, being based on pre-assumed stress distributions. Although these approaches are conservative to predict the flexural strength of ECBP from a deterministic standpoint, there are some research opportunities suggested by other researchers, which motivated the present study: i) the combined effects of the axial force P and moment resistance M are not discriminated for each component of the connection (Gomez et al., 2010; Kavoura et al., 2018a; Latour et al., 2014; Torres Rodas et al., 2016) and hence, the failure mode of these joints cannot be accurately predicted, ii) the overall check of the M-P interaction capacity of the components may be more consistent with probabilistic modern approaches (Song et al., 2021).

Despite the paramount role of ECBP in the structural behavior of SMRF, there is not uniformity between the design philosophies for these connections (Aviram et al., 2010; Díaz et al., 2020; D.-Y. Lee et al., 2008). The American and European philosophies are based on the early models proposed by Salmon *et al*. (Drake & Elkin, 1999) and, Ermopoulos and Stamatopoulos (Ermopoulos & Stamatopoulos, 1996), respectively. The non-seismic design of ECBP is featured in the AISC Design Guide 1 (DG1) (Fisher & Kloiber, 2006) and AISC 360 (AISC 360, 2016) for the American approach, or in Eurocode 3 (EC3) chapters 1-1 (CEN, 2005a) and 1-8 (CEN, 2005b) for the European one. On the other side, the seismic design is respectively featured in AISC 341 (AISC 341, 2022) and Eurocode 8 (EN-1998, 2004). In general, the seismic design of SMRF looks forward to an adequate cyclic-inelastic behavior of the ECBP. Consistently, numerous experimental and theoretical investigations have been conducted to study the rotational and the cyclic behavior of ECBP (Eröz Murat et al., 2008; A. Kanvinde et al., 2012; Latour & Rizzano, 2013; Choi & Choi, 2013; Razzaghi & Khoshbakht, 2015; Torres Rodas et al., 2016; Huang et al., 2019; Falborski et al., 2020). On the other hand, the ECBP in SMRF that are designed to withstand gravity and wind loads are expected to meet the strength limits, basically in the elastic range of each component (Kavoura et al., 2018a). Other researches have studied the shear (Gomez & Kanvinde, 2009; Shaheen et al., 2017; Tsavdaridis et al., 2015), axial and flexural (DeWolf & Sarisley, 1980; Wald et al., 1994; Jaspart & Vandegans, 1998; Gomez et al., 2010; Jaspart et al., 2008) strength of ECBP.

High values of Axial Compression Ratios (ACR) might cause that columns in Moment Resisting Frame (MRF) buildings fail to comply with strength limits proposed in building codes (Villar-Salinas et al., 2023). Besides, the column-flanges with high ACR could shorten their length due to buckling (Elkady & Lignos, 2015; Kavoura et al., 2018a; Lignos & Hartloper, 2020), which is another important reason to consider the M-P interaction in the ECBP system. Stamatopoulos *et al*. (Stamatopoulos & Ermopoulos, 1997) studied the M-P interaction diagrams for ECBP connections, considering a variation of the size and thickness of the plate; the size, length and location of the anchor bolts; and the ACR, assuming a stress-distribution which differs from the actual distribution assumed in DG1 and EC3. In Stamatopoulos *et al*. (Stamatopoulos & Ermopoulos, 1997), one M-P interaction diagram represents the failure of the ECBP subsystem for each assumed distribution of stress, but the M-P interaction diagram of each ECBP component is not discriminated.

In the light of the discussion presented in this section, this work examines the influence of the M-P interaction on the strength and failure modes of ECBP and suggests a design methodology; the scope is mainly oriented to the non-seismic design of low-rise MRF buildings. The objectives of this part of the thesis are: i) to perform Finite Element Analysis (FEA) on code-type specimens of ECBP to reproduce their failure modes and stress distributions, validating against previous experimental investigations, ii) to present an approach for obtaining the uniaxial M-P interaction diagrams of ECBP components, along the strong direction of the column, iii) to analyze the variability of the thickness of plate when the classical design approaches are followed. A background is provided in subsection 2.2 including the classical design philosophies by the American and European standards: DG1 and EC3, respectively. Subsection 4.2 describes the analyzed specimens in this study; the whole range of M-P load pairs was contemplated and grouped into three load scenarios: Zero Eccentricity (ZE), Small Eccentricity (SE) and High Eccentricity (HE). Subsection 4.3 describes the materials constitutive models, methodology and validation of the FEA. Subsection 4.4.2 presents the formulation of the M-P interaction diagrams; next, this formulation was applied to the specimens (see subsection 4.4.2.3). The code-type vs finite element analysis results are compared and discussed in subsection 4.5. Finally, a routine was programmed to calculate the required thickness of plates of the specimens for 180 M-P combinations, following the classical approach by DG1 and EC3, as shown in subsection 4.6. The main conclusions of this work are summarized in subsection 6.2.

4.2 Analyzed specimens

Early in the research, the American and European philosophies were accounted for the analysis of 180 configurations of ECBP to define three code-conforming specimens representing light, medium and deep section. HEA and HEB steel sections are intended to be used as column elements. However, HEB profiles are more robust than HEA and therefore, the former type is more commonly used than the second one, mainly in high seismic environments. For instance, Latour *et al*. (2014) also included HEA sections. Furthermore, although the M-P interaction diagram approach developed in this work is applicable to any column section, to be consistent with non-seismic low-rise MRF, the column sections selected are HEA200, HEA300 and HEA400 profiles, respectively. The materials and dimensions of the components were standardized, pointing at representing the details that are commonly used in low rise steel buildings (e.g., with less than three stories (You & Lee, 2020)) other than Special MRF; the Special MRF buildings encompass rigorous limits for the width-to-thickness ratios of columns to achieve a high ductile behavior in high seismicity areas. The aim of this standardization is to compare the implicit failure mechanisms and stress distributions by these standards. 4-bolted ECBP (type 1) were defined for HEA 200 column sections and, 6-bolted ECBP (type 2) for HEA300 and HEA400. Figure 4-1 shows the geometry configuration of the specimens.

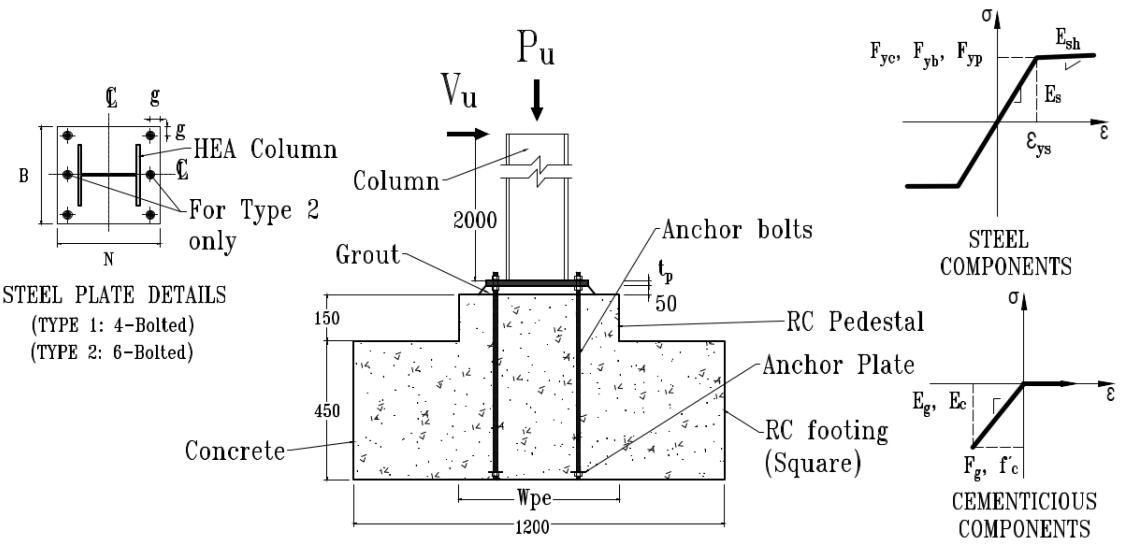

Figure 4-1. Specimens geometry (mm), configuration and material constitutive models (schematic)

In Figure 4-1; E_g, E_c and E_s are the modulus of elasticity of grout, concrete and steel elements, respectively; E_{sh} is the post-yielding modulus of elasticity of steel components; F_g is the grout strength; g is as indicated; ε_g, ε_c and ε_s are the yielding strains of grout, concrete and steel elements, respectively; V_u is the factored shear force at the column base; F_{yb} is the yielding stress of anchor bolts and; t_p is the thickness of plate. It shall be noticed that the height of the column segment for all specimens is defined as 2000 mm. Table 4-1 works complementary with Figure 4-1 on indicating the dimensions of the three specimens called S1, S2 and S3.

Table 4-1. Dimensions of specimens

Specimen	Column Section	Anchor bolts				Steel plate			
		N_b	D_b (mm)	L_e (mm)	L_b (mm)	B (mm)	N (mm)	t_p (mm)	Type
S1	HEA 200	4	20	600	725	450	450	20	1
S2	HEA 300	4	37	600	775	600	600	37	1
S3	HEA 400	6	37	600	775	650	750	37	2

In Table 4-1, N_b is the total number of bolts in the ECBP, D_b is the diameter of bolts, L_e is the length of embedment of bolts and L_b is the total length of bolts. Table 4-2 shows the geometrical properties for the three column sections used in the specimens. The slenderness ratios for flanges and web, λ_f and λ_w respectively, are calculated to classify the section per EC3 (CEN, 2005a); the column is classified as class-3 section by this document.

Table 4-2. Geometric properties of column sections

Column Section	b_f (mm)	d (mm)	s (mm)	t_f (mm)	t_w (mm)	A (mm^2)	S_x ($10^3 mm^3$)	λ_f ($b_f / 2t_f$)	λ_w (h / t_w)
HEA 200	200	190	18	6.5	10	5380	389	15.4	19.0
HEA 300	300	290	27	8.5	14	11200	1260	17.6	20.7
HEA 400	300	390	27	11	19	15900	2311	13.6	20.5

In Table 4-2, A is the cross-sectional area of the column and S_x is the elastic modulus of the column. Table 4-3 shows the details of the load definition in this study. The M-P combinations contemplate a wide range. The ACR varies from 10% to 100% and, the normalized moments from zero to 25%. This limitation to the loading ranges points to fulfill the requirements by DG1 and EC3. The axial loads and moments were incremented proportionally between the lower and upper limits to get adequate data for the M-P interaction diagrams.

Table 4-3. Loading definition					
Load Scenario	P_u / (A F_{yc}) = ACR		M_u / (S_x F_{yc})		Number of BPs analyzed
	Lower Limit (%)	Upper Limit (%)	Lower Limit (%)	Upper Limit (%)	
ZE	10	100	0	0	60
SE	20	50	5	25	90
HE	1	5	20	25	30

4.3 Numerical modelling

This section shows the results of the FEA performed in this study. The material constitutive laws are summarized in subsection 4.3.1. Subsections 4.3.2 and 4.3.3 describe the modelling method and validation of the FEA, respectively.

4.3.1 Concrete and steel constitutive models

Kanvinde *et al*. (2013) observed that the reinforcing steel of concrete pedestals of ECBP cause no significative effects on the behavior of these connections through a comprehensive numerical modelling. Besides, Fasaee *et al*. (2018) showed that the material model for grout and concrete of exposed column base plates can be simplified as elastic, based on the response observed in experimental campaigns. In this study, the concrete and grout are modeled as elastic uniaxial compressive materials (with no tensile strength), similar to as considered by Latour and Rizzano (2019). On the other hand, the steel components (anchor bolts, column and plates) were modelled as bilinear-isotropic-hardening materials, following the von Mises yield condition. The properties of materials for the specimens are summarized in Table 4-4.

Table 4-4. Material properties of specimens					
Components	F_y (MPa)	F_u (MPa)	E (GPa)	E_{sh} (MPa)	υ
Steel plates	250.0	N/A	200.0	980.0	0.3
Anchor bolts	250.0	N/A	200.0	980.0	0.3
Steel column	350.0	N/A	200.0	980.0	0.3
Grout	N/A	67.0	31.9	N/A	0.2
Concrete	N/A	24.5	21.5	N/A	0.2

In Table 4-4, F_y is the yielding stress of indicated steel-components, F_u is the ultimate stress of materials, E is the modulus of elasticity of indicated materials and υ is the Poisson ratio of materials. The elasticity modulus for all the steel components were standardized as 200 GPa; the modulus of the concrete was standardized as 21.5 GPa (= 4700 * (21) ^ 0.5 MPa), which are consistent with the minimum values allowed according to the American documents. Although the European code establishes different values for the modules, the main idea was to compare the M-P diagrams obtained with the same properties.

4.3.2 Finite element model

Figure 4-2 displays the finite element model built to represent the ECBP system for specimen S1, using Ansys (Ansys, Inc, 2018). The anchor bolts, steel plate and grout pad are shown in exploded views. The steel column, the concrete footing and the load application scheme can be noted in the 3D overview. The model meshing is composed of hexahedral elements for steel components (column flanges and web, and the steel plate). Tetrahedral-refined elements were used for the surface surrounding anchor bolts and the volume of the concrete footing.

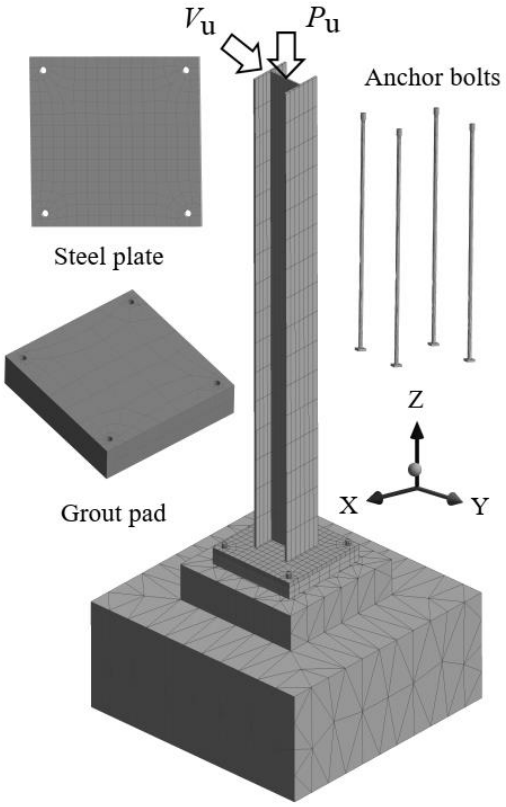

Figure 4-2. Finite element model (mesh for specimen S1)

The contact joint between the column and the steel plate was modelled as bonded-body type (monolithic) to consider that welds are detailed to withstand the probable maximum-strength of the columns. Also, the contact between the grout pad and the concrete footing was simulated as monolithic, which is aligned with experiments by Gómez *et al*. (2010) and Kanvinde *et al*. (2013). The contact between the cementitious and the steel surfaces (e.g., grout-plate, bolts-grout along the threaded length in the projection and near to the washer plates, and washers-concrete) were simulated as frictional elements with a friction coefficient equal to 0.35. The leveling nuts were not modelled given that they do not influence the stress distribution (Díaz et al., 2020).

4.3.3 Validation of the finite element analysis

For the sake of validation of the simulation methodology, one calibration model was analyzed using the same properties of the test # 1 conducted by Gómez *et al*. (2010) and then, the simulated and the experimental responses were compared. Figure 4-3b shows the base moment vs. drift curves, which indicates a good fit between; this figure displays that the performed FEA reliably predicts the elastic and inelastic drifts of the ECBP subsystem. It is noticed that the initial yielding of anchor-bolts and plate occurs at early drift values of 0.9 and 1.3%, respectively. However, the ECBP connection shows a ductile behavior up to a rather large drift of 8.5% when the grout spalls; similar observations have also been reported in many other experimental campaigns (e.g., (A. Kanvinde et al., 2012; Latour et al., 2014; Trautner et al., 2017; Wald et al., 1994)). Figure 4-3a shows the deformed shape of the specimen S1 for the scenario HE (with P_u = 0 kN and M_u = 80 kN-m). It can be noticed that the deformation distribution is in accordance with the direction of the applied force V_u (Y+, see Figure 4-2). This is, there are tensile deformations at the pair of bolts located in the direction Y-, and compression at the bolts group in the direction Y+.

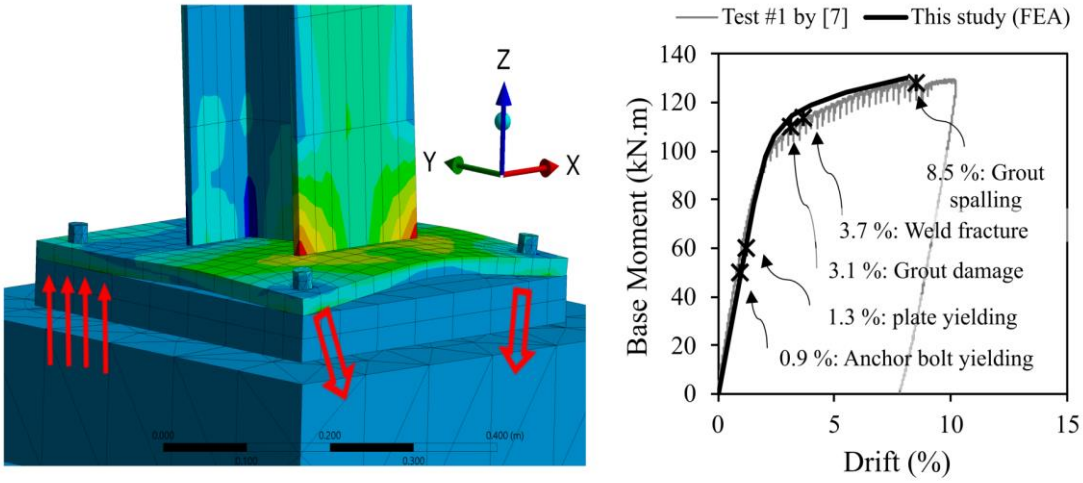

a) Deformed shape of S1 for V_u=40kN and P_u= 0 b) Moment vs. drift curves

Figure 4-3. Validation of the FEA methodology

Figure 4-4a and b show the maximum principal tensile stresses σ_1 on the grout pad and the steel plate of S1 when it is subjected to HE loads (P_u = 0 kN and M_u = 80 kN-m). There are tensile stresses in the anchor bolts located at Y- with pure bending around axis X (Figure 4-4a), while no tensile stresses are transferred to the top of the grout (Figure 4-4a).

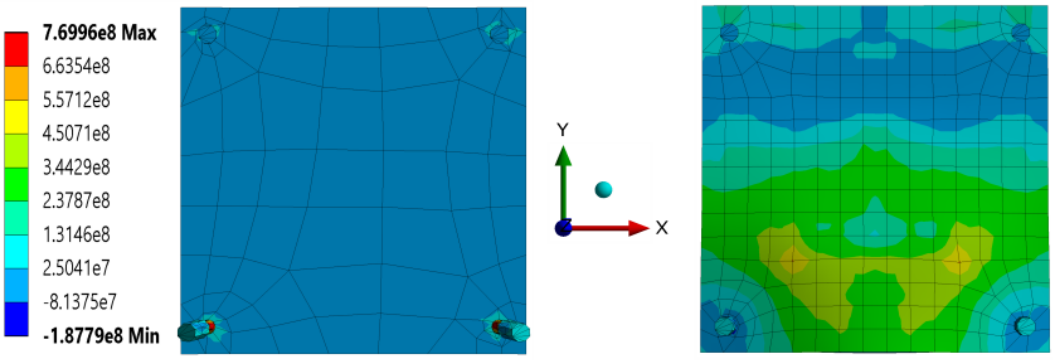

a) Grout pad surface b) Steel plate surface

Figure 4-4. Maximum principal tensile stresses σ1 (Pa) in S1 for Pu = 0 and Vu = 40 kN

Figure 4-5a and b show the maximum principal compressive stresses σ_3 on the grout pad and the steel plate, of S1 for ZE, under a vertical load of 1890 kN, in that order. It is noticed that ZE only generates compressive stress on the top of the grout pad. No tensile stress in the anchor bolts (Figure 4-5a). In general, Figure 4-4 and Figure 4-5 show that the compressive and tensile stress distributions are directly associated with the loading scenario. Further discussion of the FEA results is presented in section 4.5.

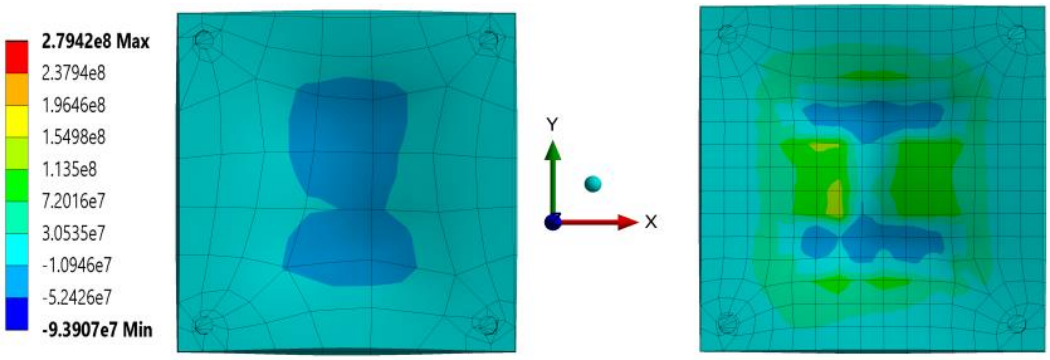

a) Grout pad surface b) Steel plate surface

Figure 4-5. Maximum principal compressive stresses σ3 (Pa) in S1 for Vu = 0 and Pu = 1890 kN

4.4 Analysis of ECBP according to the American and European design philosophies

Subsection 4.4.1 summarizes the classical analysis and design of ECBP by DG1 and EC3. The M-P interaction approach for the analysis and design of all the components of the ECBP is described in subsection 4.4.2.

4.4.1 Classical analysis and design framework by AISC and EC3

This research connects MATLAB® routines with Microsoft Excel® spreadsheets to apply the design philosophies summarized in subsection 2.2, in a classical approach. This framework aims to calculate the minimum thickness of plate required to fulfill the strength limit-states per DG1 and EC3. Figure 4-6 shows a flowchart which summarizes this process.

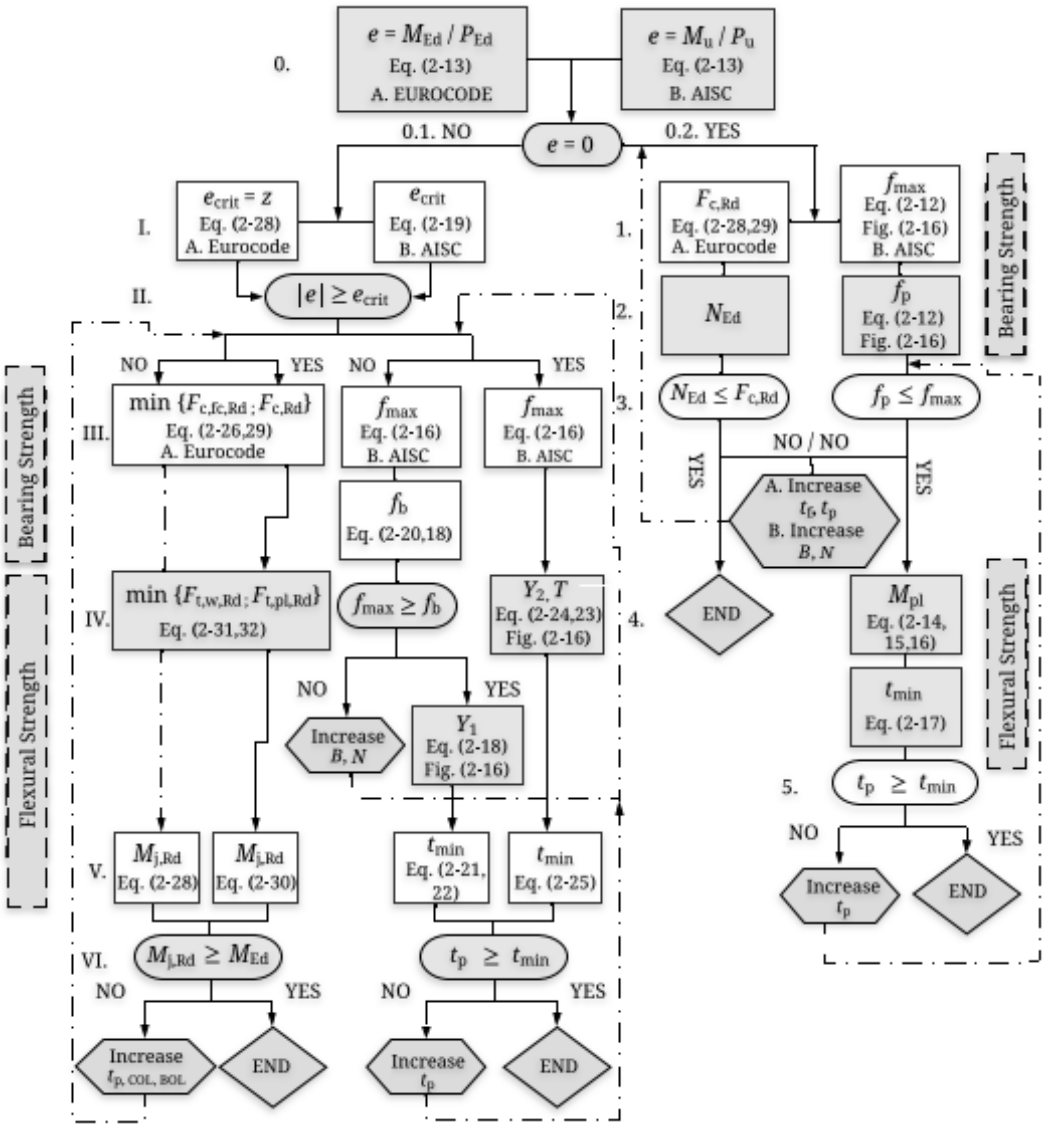

Figure 4-6. Flowchart of the traditional analysis and design process by AISC and Eurocode

4.4.2 M-P interaction diagrams approach to the analysis and design of ECBP

The design philosophies described in subsection 2.2 can be adapted to build M-P interaction diagrams for each of ECBP components; the process to obtain these diagrams is summarized in Figure 4-7; the formulations for these approach are summarized in subsections 4.4.2.1 and 4.4.2.2. The M-P interaction diagrams include all the dimensions and material properties of the connection. Therefore, the proposed approach might work complementary with the classical approach. For instance, the classical framework (subsection 4.4.1) can be used to define dimensions and materials and, the M-P interaction diagrams might be used to check each component against every M-P reaction on the ECBP that results from the structural analysis.

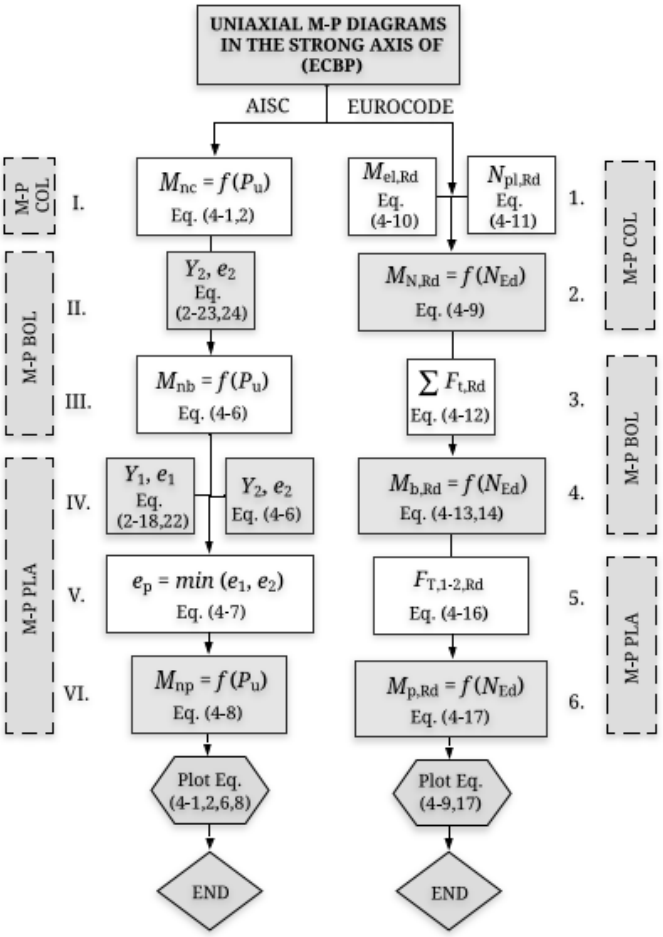

Figure 4-7. Flowchart of the M-P interaction diagrams approach to the analysis and design of ECBP

The results of the FEA can also be adapted to simulate the experimental M-P interaction diagram of ECBP. For this purpose, several combinations of increasing M-P loads (e.g., P_u and M_u) are applied to the specimens S1, S2 and S3. Then, the maximum principal stresses σ_1 and σ_3 are measured at each loading step to identify which of the components reach the yielding stress first. At the time of the failure of any component, one pair of M-P values is registered to build the finite element M-P interaction diagrams. Figure 4-8 depicts the macro-model for the M-P interaction diagrams approach presented in this study.

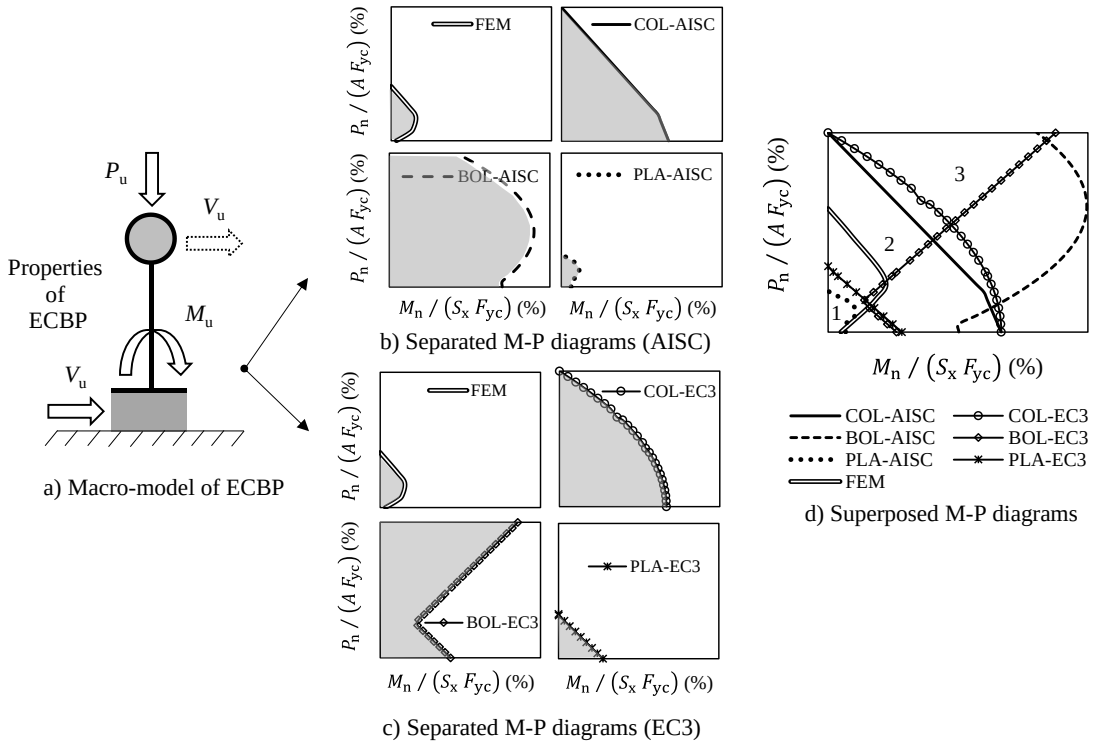

Figure 4-8. Schematic macro-model for the M-P interaction diagrams approach for ECBP

The material properties and, the geometrical and load definition of ECBP are considered to develop the M-P interaction diagram for each component, as shown in Figure 4-8b; the internal shallowed area of the diagrams represent the fulfillment area while the external area depicts the non-fulfillment area of elements. When the diagrams of the main components of ECBP are superposed (see Figure 4-8c), the strength and the failure mode of the connection can be estimated for any M-P combination. For instance, in the figure, the connection would withstand the load combination represented by point 1 in the elastic range, would have a yielding plate for point 2 and, yielding plate and column for point 3. The overall adjustment between the Finite Element Method (FEM) diagram and the diagrams of the plate PLA-AISC and PLA-EC3, denotes that the plate would be the first yielding component for the full-range of M-P pairs. Apparently, this drawback (in the standpoint of a non-optimal use of the strength of other elements) might be overcome by increasing the plate thickness. Nevertheless, also the ductility of the ECBP subsystem shall be verified for seismic design.

4.4.2.1 M-P interaction diagrams of ECBP according to AISC

The M-P interaction in columns is explicitly set by AISC 360 (2016), as shown in Eq. (4-1) and (4-2):

$$\frac{P_u}{\phi P_{nc}} + \frac{8}{9}\left[\frac{M_u}{\phi_f M_{nc}}\right] \le 1 \text{ for } \frac{P_u}{\phi P_{nc}} \ge 0.2 \tag{4-1}$$

$$\frac{1}{2}\frac{P_u}{\phi P_{nc}} + \frac{M_u}{\phi_f M_{nc}} \le 1 \text{ for } \frac{P_u}{\phi P_{nc}} < 0.2 \tag{4-2}$$

ϕ and ϕ_f are set as 1.0 in this research. P_{nc} and M_{nc} are the resistant axial force and flexural moment of the column, in the same order. In the M-P interaction diagrams, the maximum values of these strengths are located on the ordinate (vertical) and abscissa (horizontal) axes, respectively; these maximum values are determined by Eqs. (4-3) and (4-4), in the same order. For other strength values, M_{nc} can be obtained directly from Eqs. (4-1) and (4-2), as a function of P_u, M_u and P_{nc}, which are all three considered as known variables for each specimen. M_{nc} in Figure 4-7, refers to the failure of the column. The plots of the M-P interaction diagrams for the columns of S1, S2 and S3 (Figure 4-9a, b and c) are shown by the series COL-AISC.

$$P_{nc} = A\ F_{yc} \tag{4-3}$$

$$M_{nc} = S_x\ F_{yc} \tag{4-4}$$

The M-P interaction diagrams for the bolts, by combining Eqs. (4-5) and (4-6). The tensile strength of one line of bolts T is calculated with Eq. (4-5).

$$T = F_{ub}\left(N_b/2\right)A_b \tag{4-5}$$

$Y2$ in Eq. (4-6) is obtained from Eq. (2-23), in terms of the previously known variables q_{max} (Eq. (2-19)), f'_c, B, T (Eq. (4-5)) and P_u. In parallel, $e2$ may be computed re organizing Eq. (2-24). Finally, M_{nb} is defined as a function of P_u, considering the failure of bolts (Eq. (4-6)). The plot of the M-P interaction diagram for the bolts of S1 is shown by the series BOL-AISC (Figure 4-9a), and it is shown accordingly for specimens S2 and S3 (Figure 4-9b and c).

$$M_{nb} = P_u\ e2;\ Y2 = \frac{T + P_u}{q_{max}};$$
$$e2 = \frac{\left[\left(f_b + \frac{N}{2}\right)^2 - \left(\left(f_b + \frac{N}{2}\right) - Y2\right)^2\right] q_{max}}{2\ P_u} - f_b \tag{4-6}$$

The M-P interaction approach for the steel plate, is affected by the critical eccentricity between scenarios SE and HE, e_p (Eq. (4-7)). e_p is the minimum between $e1$ (Eq. (2-18)) and $e2$ (Eq. (4-6)). Then, reduced flexural strength M_{np} is given by Eq. (4-8).

$$e_p = \min\left[e1; e2\right] \tag{4-7}$$

$$M_{np} = P_u\ e_p \tag{4-8}$$

The series PLA-AISC in Figure 4-9a, b and c represent the plots of the M-P interaction diagrams for the steel plates of S1, S2 and S3; respectively.

4.4.2.2 M-P interaction diagrams of ECBP according to EC3

The M-P interaction in columns is explicitly set by EC3-subsection 1-1 (CEN, 2005a), with $M_{N,Rd}$, the reduced resistance to bending moments making allowance for the presence of normal forces, as shown in Eq. (4-9).

$$M_{N,Rd} = M_{el,Rd}\left[1 - \frac{N_{Ed}}{N_{pl,Rd}}\right]^2 \tag{4-9}$$

$N_{pl,Rd}$ is the plastic resistance force of the gross cross-section; N_{Ed} is the acting normal force; the flexural resistance is equivalent to the maximum elastic resistance $M_{el,Rd}$. Since the columns of S1, S2 and S3 are class 3-sections, $M_{el,Rd}$ is calculated with Eq. (4-10).

$$M_{el,Rd} = \frac{S_x\ F_{yc}}{\gamma_{M0}} \tag{4-10}$$

It shall be noticed that $M_{el,Rd}$ is equal to M_{nc} in Eq. (4-4) when no safety factors are considered, or γ_{M0} equal to 1, as considered in this research. $N_{pl,Rd}$ for class 3-sections can be stated per Eq. (4-11).

$$N_{pl,Rd} = \frac{A\ F_{yc}}{\gamma_{M0}} \tag{4-11}$$

$M_{N,Rd}$ can be obtained directly by replacing Eqs. (4-10) and (4-11) in Eq. (4-9), as a function of N_{Ed}. The series COL-EC3 in Figure 4-9a, b and c represent the plots of the M-P interaction diagrams for the columns of S1, S2 and S3; respectively.

The M-P approach for the bolts begins with the definition of their tensile strength $\Sigma\ F_{t,Rd}$. $\Sigma\ F_{t,Rd}$ is equivalent to T in DG1, and may be calculated with Eq. (4-12).

$$F_{t,Rd} = \frac{0.9\, F_{ub}\, A_s}{\gamma_{M2}} \tag{4-12}$$

The ratio $0.9 / \gamma_{M2}$ is considered as 1.0 to refer to the failure, as safety factors are excluded in this work. A_s is the total area of the bolts in one line that acts as a moment resisting element. The flexural resistance of the ECBP, associated to the failure of the bolts $M_{b,Rd}$ can be determined as a function of N_{Ed}, with Eq. (2-30). In this equation, $M_{j,Rd} = M_{b,Rd}$. This is, the resistance of the joint is forced to be equal to the resistance of the bolts. Besides, the eccentricity may be $M_{b,Rd} / N_{Ed}$. Eqs. (4-13) and (4-14) shall be used to calculate $M_{b,Rd}$.

$$M_{b,Rd} = \sum F_{t,Rd}\ z - N_{Ed}\ Z_C \quad \text{for e} \geq e_{crit} \tag{4-13}$$

$$M_{b,Rd} = N_{Ed}\ Z_C \quad \text{for e} < e_{crit} \tag{4-14}$$

It can be noted in Figure 2-18 that e_{crit} is approximately equal to Z_C ($\approx d / 2$). Besides, anchor bolts work in traction only for HE (high eccentricity scenario or $e \geq e_{crit}$). Thus, Z_C is a limit for Eq. (4-13). Then, hypothetically the strength of the bolts increases continuously asymptotically when N_{Ed} is greater than the N_{Ed} related to e_{crit}, as stated in Eq. (4-14). $F_{T,1\text{-}2,Rd}$ (Eq. (4-15)) represents an alternative calculation of $\Sigma\ F_{t,Rd}$ (Eq. (2-30)). Thereupon, Eq. (2-33) and (4-15) may be combined to re write $F_{T,1\text{-}2,Rd}$ as shown in Eq. (4-16).

$$F_{T,1\text{-}2,Rd} = \frac{2\, M_{pl,1,Rd}}{m} \tag{4-15}$$

$$F_{T,1\text{-}2,Rd} = \frac{0.5\, l_{eff}\ t_f^2\ F_{yc}}{m\ \gamma_{M0}} \tag{4-16}$$

The plots of the M-P interaction diagrams for the ultimate strength of the anchor bolts of S1, S2 and S3 are shown by the series BOL-EC3 in Figure 4-9a, b and c; respectively.

For the M-P interaction diagrams of the steel plate, Eq. (4-13) and (4-16) may be combined to obtain the reduced flexural strength $M_{p,Rd}$, as shown in Eq. (4-17). In Eq. (4-13), $M_{b,Rd}$ is replaced by $M_{p,Rd}$ to refer to the plate; $\Sigma\ F_{t,Rd}$ is replaced by the alternative method for $F_{T,1\text{-}2,Rd}$ (Eq. (4-16)).

$$M_{p,Rd} = F_{T,1\text{-}2,Rd}\ z - N_{Ed}\ Z_C \tag{4-17}$$

The series PLA-EC3 in Figure 4-9a, b and c represent the plots of the M-P interaction diagrams for the steel plates of S1, S2 or S3; respectively.

4.4.2.3 M-P interaction diagrams for the analyzed specimens

Figure 4-9a, b and c show the M-P interaction diagrams for the components of specimens S1, S2 and S3 respectively. The failing components are marked on the diagrams. Besides, the fit between M-P interaction diagrams obtained from the FEA and those obtained through the proposed approach, is illustrated on these figures.

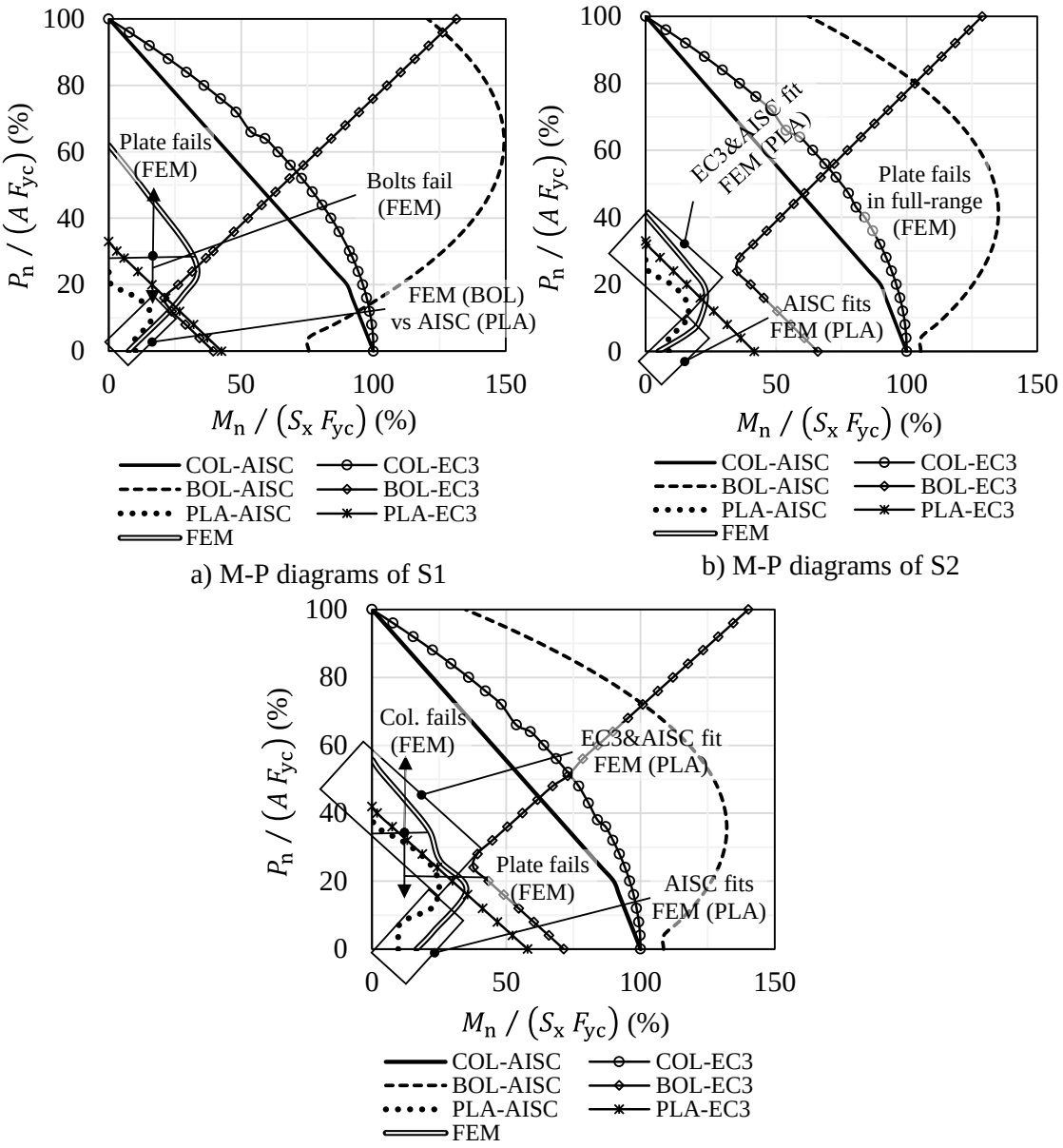

a) M-P diagrams of S1

b) M-P diagrams of S2

c) M-P diagrams of S3

Figure 4-9. Application of the M-P interaction diagrams approach for the specimens S1, S2 and S3

The FEM diagrams reveal that the steel plates of specimens S2 and S3 are the failing components for almost the whole range of axial loads (see Figure 4-9b and c); only for S3, there is an initial yielding of the column flanges for ACRs greater than 34%. For S1, the FEA displays that the plate yields for ACRs greater than 28% while the bolts are the yielding component for other values of ACR. Further discussion of these diagrams is presented in subsection 4.5.

4.5 Code-type vs. finite element analysis

The results of the FEA and the application of the M-P interaction diagrams approach to the specimens are discussed in this section; the discussion points to examine the influence of the M-P interaction on the strength of the ECBP components (subsection 4.5.1) and the failure mode of the connections (subsection 4.5.2).

4.5.1 Effect of the M-P interaction on ECBP strength

For ZE, Figure 4-9 shows that the normalized axial-strength P_n / ($A F_{yc}$) of the specimens, according to the FEM, AISC and EC3 respectively are: i) 62, 24 and 33% for S1; ii) 41, 24 and

33% for S2 and; iii) 56, 36 and 40% for S3. The plate is the yielding component for all samples. These results indicate that the thickness of plate is not enough to reach the whole axial strength of the columns, neither by EC3 nor DG1. Besides, the M-P interaction diagrams illustrate that DG1 is more conservative than EC3, which is consistent with the results of the classical analysis shown in Figure 4-10, namely, EC3 specify slightly thinner plates than AISC does. Overall, according to DG1 and EC3, the yielding of the plate is expected for ZE, in a strong-column-weak-plate fashion. Conversely, the FEA results display that some yielding of the column-flanges might occur in deep sections. In accordance with this analysis, recent experimental tests on deep sections (Elkady & Lignos, 2015), also shows that the strength of these columns could be reduced by local or general buckling, which are not currently contemplated by DG1 and EC3. In seismic environments, the ACR for bottom story columns are around 20-35% (Elkady & Lignos, 2015). Therefore, the ACR in columns should be limited to warrant appropriate safety levels.

For SE, the simultaneous axial-flexural strengths for each specimen are predicted through the M-P interaction diagrams and, represented with pairs ACR-M_n / ($S_x F_{yc}$). According to the FEA diagrams in Figure 4-9, these pairs are: i) 25%-27% for S1 (plate and bolts), ii) 18%-23% for S2 (plate) and, iii) 35%-21% for S3 (plate and column). It shall be noticed that related failing components are stated within brackets. Analogically, DG1 conducts to 12%-16% (plate), 12%-17% (plate) and 16%-25% (plate) for S1, S2 and S3 respectively. On the same way, EC3 leads to 16%-21% (plate), 18%-23% (plate) and 20%-30% (plate and bolts) for S1, S2 and S3 respectively. Overall, DG1 and EC3 are properly adjusted to the FEA results for SE.

For HE, the normalized flexural-strengths M_n / ($S_x F_{yc}$) of the specimens can be graphically observed on the M-P interaction diagrams for FEA, AISC and EC3 (Figure 4-9). These strengths are respectively: i) 9, 9 and 43% for S1 (bolts); ii) 5, 5 and 42% for S2 (plate) and iii) 19, 9 and 58% (bolts). Table 4-5 summarizes the strength and failure modes of the specimens, for all the load scenarios.

Table 4-5. Strength and failure modes of the specimens

Specimen	Method	Description	Load scenarios					
			ZE		SE		HE	
			$\frac{P_n}{A F_{yc}}$	$\frac{M_n}{S_x F_{yc}}$	$\frac{P_n}{A F_{yc}}$	$\frac{M_n}{S_x F_{yc}}$	$\frac{P_n}{A F_{yc}}$	$\frac{M_n}{S_x F_{yc}}$
S1	FEA	BP Strength (%)	62	0	25	27	0	9
		Failing component	Plate		Plate-Bolts		Anchor bolts	
	AISC	BP Strength (%)	24	0	12	16	0	9
		Failing component	Plate		Plate		Plate	
	EC3	BP Strength (%)	33	0	16	21	0	43
		Failing component	Plate		Plate-Bolts		Anchor bolts	
S2	FEA	BP Strength (%)	41	0	18	23	0	5
		Failing component	Plate		Plate		Plate	
	AISC	BP Strength (%)	24	0	12	17	0	5
		Failing component	Plate		Plate		Plate	
	EC3	BP Strength (%)	33	0	18	23	0	42
		Failing component	Plate		Plate		Plate	
S3	FEA	BP Strength (%)	56	0	35	21	0	16
		Failing component	Column		Plate-Column		Plate	
	AISC	BP Strength (%)	36	0	16	25	0	9
		Failing component	Plate		Plate		Plate	
	EC3	BP Strength (%)	40	0	20	30	0	58
		Failing component	Plate		Plate		Plate	

In general, the M-P interaction diagrams in Figure 4-9 indicate that the flexural strength of code-complying ECBP is reduced by the increment of the ACR.

4.5.2 Failure mechanism and stress distribution

For ZE, the FEA results shown in Figure 4-5a, reveal that for specimen S1, a 3/4" thickness plate is not thick enough to uniformly spread the applied axial load of 1890 kN, on the grout pad. The compressive stress is concentrated below the column web zone with a magnitude of about 52 MPa, while the stress around is about 11 MPa. Reasonably, the stress distribution on the steel plate (Figure 4-5b) is still less uniform than the stress distribution on the grout pad. The former stress-distribution follows the shape of the column section, and therefore is similar to the T-Stub distribution adopted by EC3 (see Figure 2-18). The RSB distribution of DG1 assumes a uniform spread, therefore it is not in accordance with the distribution observed in the FEA results.

For HE loads on specimen S1, Figure 4-4a indicates that a 3/4" thickness plate uniformly spread the 80 kN-m moment (= 40 kN × 2 m) on the grout pad, with a stress magnitude near to 188 MPa; the bolts are subjected to a tensile stress of about 770 MPa. On the opposite, the stress distribution on the steel plate (Figure 4-4b) is not uniform. The zone of the plate at Y- is mainly under tensile stress with a maximum of near to 663 MPa, and the zone at Y+ is principally under compressive stress, with a maximum of near to 81 MPa. Reasonably, the stress distribution in Figure 4-4 is in accordance with the deformed shape shown in Figure 4-3, which is also associated with HE. Figure 4-3 shows that the column flange is under a tensile stress of about 770 MPa at the bottom, which makes the plate to partially unstick from the grout pad; this deformation shape is similar to that observed in the test # 1 performed by Gómez *et al*. (2010). The T-stub distribution assumed by EC3 for HE (Figure 2-19c) fits the results obtained by the FEA (Figure 4-4b). The RSB distribution assumed by DG1 for HE (Figure 2-16c) contemplates a wide band extended to the edge of the plate, which is not exactly equal to the FEA distribution.

4.6 Required thickness of ECBP

The thickness of plate t_p is one of the most relevant design variables of ECBP, given that t_p directly affects the strength of the connection, following both DG1 and EC3. In order to investigate the variability of t_p due to M-P combinations according to the classical approach of DG1 and EC3 (summarized in Figure 4-6), this variable is selected as the response variable while the other design variables of specimens (e.g., B, N, N_b and D_b) remains constant as defined in subsection 4.2. Then, the minimum t_p values required for each M-P pair are calculated and discussed in this subsection. Figure 4-10 shows the variability of t_p due to the ACR, for ZE.

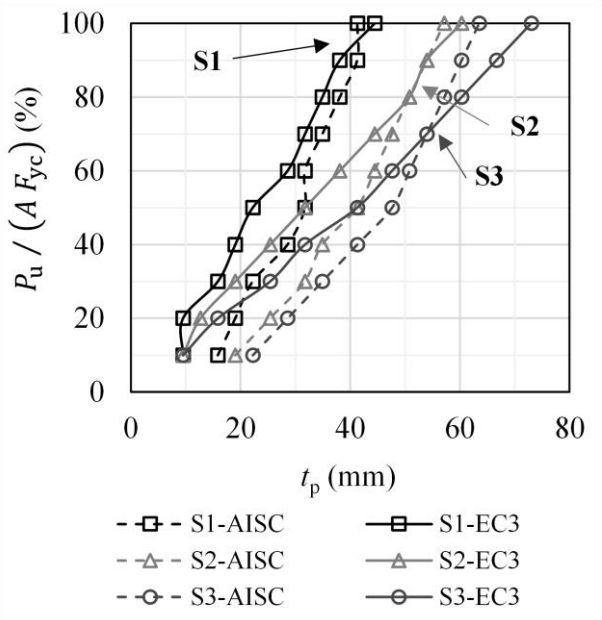

Figure 4-10. Variability of the thickness of plate for zero eccentricity (ZE)

It is observed in Figure 4-10 that overall, DG1 conducts to slightly thicker plates than EC3 for ZE. However, the trend changes for ACR above 60%, especially for S3. Figure 4-11 shows the variability of t_p due to the normalized moment M_u / (S_x F_{yc}), for SE with ACR equal to 30% (Figure 4-11a), 40% (Figure 4-11b) and 50% (Figure 4-11c). This figure indicates that for SE, DG1 also conducts slightly thicker plates than EC3.

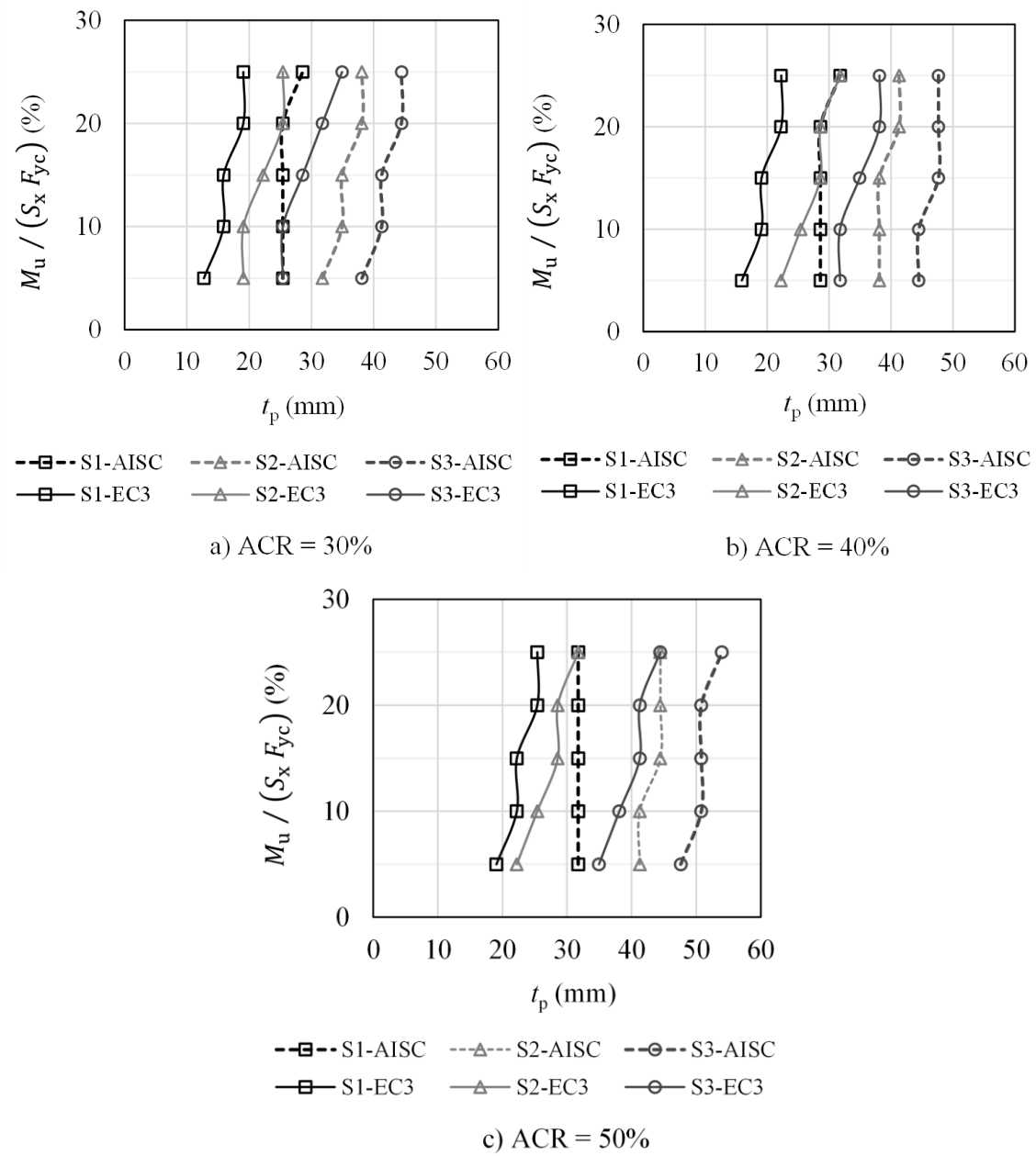

Figure 4-11. Variability of the thickness of plate for small eccentricity (SE)

The straight line generated by the points S1-AISC in Figure 4-11c indicates that the plate is not the failing component according to the AISC philosophy for the range of moments evaluated. Nevertheless, this result does not agree with FEA results; this disagreement is suggested by the M-P diagram approach. For instance, the points PLA-AISC Figure 4-9a do not converge with the points FEM of the same figure. Figure 4-12 shows the variability of t_p due to M_u / (S_x F_{yc}), for high eccentricity scenario HE, with ACR equal to 5% and f'_c equal to 28 MPa. This figure indicates that DG1 leads to slightly thinner plates than EC3 when M_u / (S_x F_{yc}) decreases under 20%, mainly for light-weight column sections (S1). For medium-weight sections (S2), t_p is similar for both DG1 and EC3, and for heavy-sections (S3), the trend is similar to the results for ZE and SE. This is, DG1 requires thicker plates than EC3, for normalized moments above 15%.

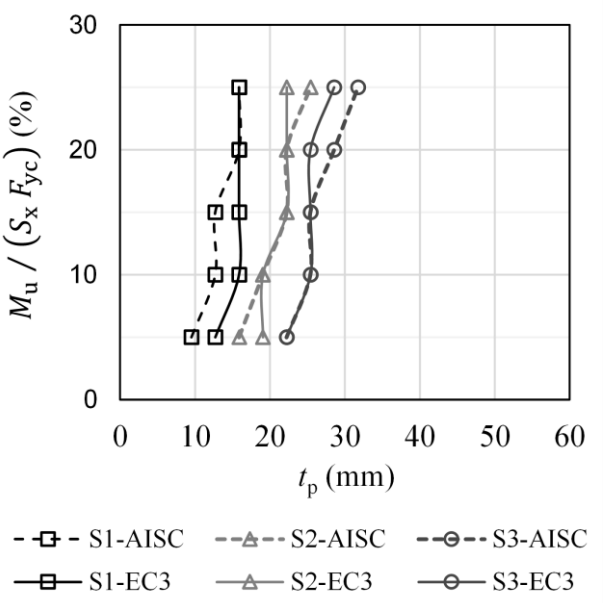

Figure 4-12. Variability of the thickness of plate for high eccentricity (HE)

5 MODELLING PARAMETERS FOR PERFORMANCE-BASED ASSESSMENT OF EXPOSED COLUMN BASE PLATES SUBJECTED TO FLEXURE AND AXIAL COMPRESSION

5.1 Introduction to this section

Exposed Column-Base Plate (ECBP) connections are critical to steel Moment Resisting Frames (MRF), since their behavior influences the overall performance of these structures, as noted in numerous studies (Ermopoulos & Michaltsos, 1998; Eröz Murat et al., 2008; Fasaee et al., 2018; Grauvilardell et al., 2005; Jaspart & Vandegans, 1998; Khodaie et al., 2012; Piana & F. G. Calenzani, 2018; Tsavdaridis et al., 2015). Despite major advances in the understanding of their strength (e.g., axial, rotational and shear) and stiffness, important knowledge gaps remain. As noted by Zareian and Kanvinde (2013), and, Latour and Rizzano (2019), a significant gap is in the area of guidance for simulating the nonlinear rotational behavior of these connections, within the context of modern performance assessment frameworks. This behavior is often complex and a function of the interaction of its components (e.g., column, anchor bolts, plate, and concrete), loads and the soil structure interaction, as described by Kanvinde *et al*. (2013). When base connections are designed to be elastic, which is common in non-seismic conditions (AISC DG1 (Fisher & Kloiber, 2006)), and many seismic conditions as well (AISC 341-22, D2.6c (2022)), the primary concern is representing their rotational flexibility (or initial stiffness). Previous studies (e.g., Kanvinde *et al*. (2012), Latour *et al*. (2014)) have developed models for the estimation of such flexibility. These models have been validated at the laboratory scale (e.g., Gómez *et al*. (2010)), as well as through data obtained from instrumented buildings (Falborski *et al*. (2020)), and indicate that: (i) assuming the base connection to be either fixed or pinned, as is often done, is erroneous, and (ii) base connection configuration has a strong influence on connection rotational stiffness. More recently, there has been a focus on "weak-base" connections in seismic conditions, wherein the base connection is designed to be weaker than the column. Such connections are explicitly mentioned in American design codes, wherein the ECBP may be designed for typically for a building base shear corresponding to the overstrength (i.e., the Ω_0-factor, AISC 341-22 (2022)). Specifically, studies by Hassan *et al*. (2022), Falborski *et al*. (2020), as well as Trautner *et al*. (2017), indicate that substantial economies may be achieved in connection design if adequate deformation capacity is provided in these connections. However, the implied nonlinear response of these connections (either by design or through unanticipated overloads) necessitates approaches for estimation of the full nonlinear response (beyond just the initial rotational stiffness) for performance assessment of structures utilizing weak-bases. Developing such approaches is the primary objective of this paper.

A review of literature over the last three decades indicates significant progress in understanding ECBP response, and the development of models to represent it. Studies by Picard and Beaulieu (1985), Melchers (1992), Hon and Melchers (1988), Jaspart and Vandegans (1998), and, Kavoura and co-workers (refer to (Kavoura et al., 2015, 2017, 2018b)) collectively indicate that the rotational stiffness of ECBP connections increases with the axial load on the column; thus, this stiffness should be considered in the structural analysis. Following this observation, analytical models have been proposed to represent various parts of the load deformation response. Primarily, these models focus on the strength or stiffness of these connections. For strength characterization,

notable work includes that of Salmon *et al*. (1957), Ermopoulos and Stamatopoulos (1996), Drake and Elkin (1999) (which forms the basis of AISC Design Guide 1 (Fisher & Kloiber, 2006)), and Kanvinde *et al*. (2015). For rotational stiffness characterization notable work includes Kanvinde *et al*. (2012), Dumas *et al*. (2006), and Diaz *et al*. (2020). Cumulatively, these models provide fairly reliable ways of characterizing the strength and stiffness of these connections. The former (i.e., the strength) is important from a design perspective, and the latter (i.e., the stiffness) is important from the perspective of representing these connections in linear analysis (or when the base is anticipated to remain elastic). However, only the strength and stiffness are not sufficient for representing the full nonlinear rotation response of these connections, which includes other features as well, corresponding to the deformation hardening, ductility, as well as the capping (or loss of stiffness) as failure modes are initiated. As discussed above, representation of such response becomes important when the base connections are anticipated to deform into the inelastic range, either by design, or due to unanticipated overloads. In this regard, it is relevant to mention models for estimating the in-cycle ductility (e.g., Latour and Rizzano (2013)) and the cyclic degradation of ECBP (i.e., Torres-Rodas *et al*. (2016), and, Latour and Rizzano (2019)). Other than these limited studies (that focus on very specific connection configurations), there is very limited guidance for the simulation of this full response. Motivated by this, an approach to estimate parameters defining the full rotational response of ECBP connections is presented. This approach focuses on monotonic response (i.e., the backbone curve) and is based on a combination of mechanistic models (for some parameters) and regression based predictive equations for others, where the mechanics is not evident. A complementary web-based tool and database (https://cbp-db-modelling.utb.edu.co/model) of test results is also provided to facilitate convenient and transparent estimation of parameters.

The next subsection of the chapter provides relevant background information; this is followed by a description of the test database from which the approach is developed. The approach, involving estimation methods for each relevant parameter is then presented, and examined against test data.

5.2 Background: a trilinear model for the Moment-rotation curves of ECBP

Figure 5-1 illustrates a typical ECBPs assembly to the common construction practice in the United States, and experimental testing of these connections. Also, the figure displays the force transfer mechanism in the joint, which entails interaction among the various components. For instance, applied force and moment in the column, are transferred to the steel plate. Then, depending on the moment-axial loads interaction itself (e.g., large loads eccentricity), eventual tensile loads in the anchor rods and bearing stresses in the concrete footing.

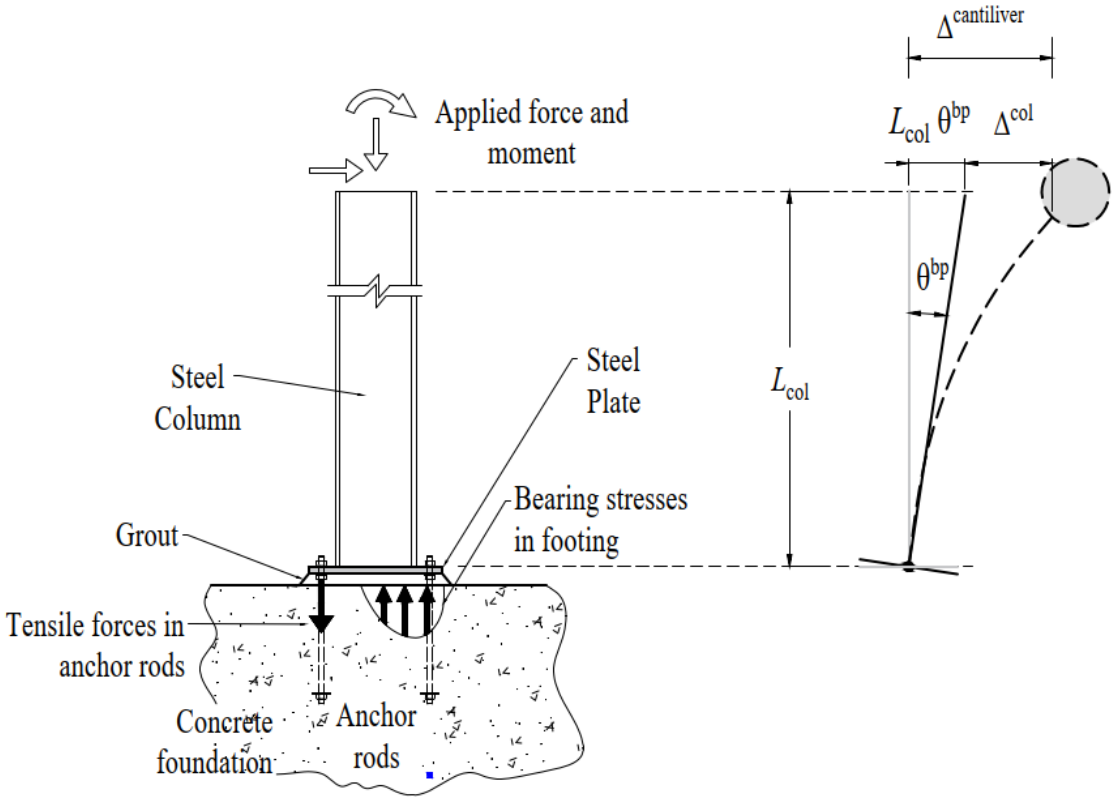

Figure 5-1. Typical assembly and general response of ECBP (schematic)

Referring to Figure 5-1, it is important to note that in the context of this paper, the elastic deformations of the column Δ^{col} are not considered in the model development considered herein. In most of the experiments the lateral force and cantilever displacements $\Delta^{cantiliver}$ are recorded, then, the test data is processed accordingly to remove these deformations. The moment-rotation (M-θ) curves may be converted as shown in Eqs. (5-1) and (5-2).

$$M_u = V_u \, L_{col} \tag{5-1}$$

$$\theta^{bp} = \left(\Delta^{cantiliver} - \frac{V_u \, L_{col}^3}{3 \, E_{col} \, I_{col}} \right) \frac{1}{L_{col}} \tag{5-2}$$

where V_u and M_u are the measured horizontal load and moment at any loading step, respectively. L_{col} is the column length, θ^{bp} is the measured rotation of the ECBP, E_{col} is modulus of elasticity of the column, I_{col} is the moment of inertia of the column.

A trilinear model for the backbone of M-θ curves is used to idealize the response of ECBPs in a parametric way. Such a model is sufficient to represent the ductility, stiffness and strength degradation of the connections, considering the results by Rodas *et al.* (2016). Figure 5-2 illustrates the key assumptions of the trilinear model and its basis. It shall be noted that the ordinates of the curves are conveniently normalized to the column yielding-strength M_y^{col} (= $S_x \, F_{yc}$); where S_x and F_{yc} are the elastic modulus and yielding stress of the column, respectively. The inset hysteretic graphic corresponds to a half-cycle of loading; for subsequent half-this graphic repeat accompanied by degradation due to residual deformations of the components.

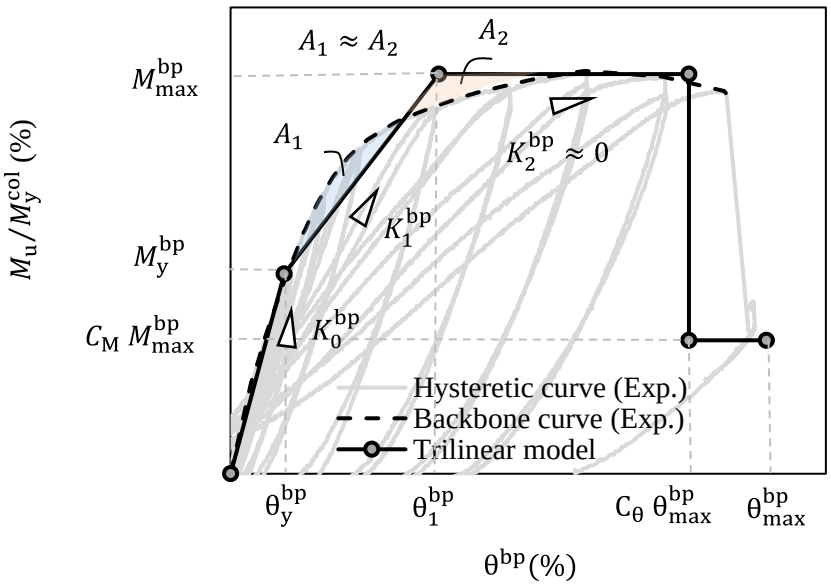

Figure 5-2. Trilinear model for idealization of moment versus rotation response of ECBP (schematic)

The trilinear idealization is parametrically represented through the parameters shown in Table 5-1.

Table 5-1. Summary of the model parameters for moment-rotation curves of ECBP

Modeling parameter	Description
θ_y^{bp}	yielding rotation. This deformation marks the end of the initial nearly linear response. This parameter normally matches the yielding of one of the connection components (e.g., the plate in either the compression or traction side, or the anchor rods in traction). the pos-yielding range employs energy balance to have $A_1 \approx A_2$. The initial and post-yielding rotational stiffnesses K_0^{bp} and K_1^{bp} can be derived with the modelling parameters.
θ_1^{bp}	rotation associated with the start of the plastic plateau. Experiments performed by Gomez *et al*. (2010) indicate that this parameter involves the yielding of a second component in the joint (e.g., if the plate yielded first in compression, then a subsequent yielding of the plate or anchor rods in traction)
θ_{max}^{bp}	ultimate base rotation.
M_y^{bp}	yielding strength. This is the moment associated with the yielding rotation of the connection. Larger deformations then the yielding rotation, involve a stiffness (moment-rotation relationship) degradation of the connection.
M_{max}^{bp}	ultimate or capping moment strength. This moment is linked to the yield plateau. Often, the connection can sustain this moment until the ultimate base rotation or unloading stage (i.e., for cyclic loading)
C_M, C_θ	post-peak degradation coefficients for cyclic effects. C_M and C_θ are less than 1.0 to represent the percentage of degradation in the strength and deformation, respectively.

In contrast to the helpfulness of the curves, the cost and time of setting the full range of the M-θ curves by experimental testing, for all the practical types and geometrical configuration of ECBP, would be too expensive and time consuming (Razzaghi & Khoshbakht, 2015). As a result, some analytical (i.e., those in Torres-Rodas *et al*. (Torres Rodas et al., 2016) and, Latour and Rizzano (Latour & Rizzano, 2019)) and numerical (e.g., Stamatopoulos and Ermopoulos (Stamatopoulos & Ermopoulos, 2011), and,

Abdollahzadeh and Ghobadi (Abdollahzadeh & Ghobadi, 2014)) models have been proposed to predict the full range of M-θ curves for ECBP. Based on authors´ analysis, the following are limitations of some published analytical models for predicting the full range of M-θ curves, which are evaluated and overcome in this study:

- the predicted rotational strength M_n^{bp} by Fisher and Kloiber (2006) (DG1) is conceptually defined as the moment for the yielding of the first BP component, which should be comparable with M_y^{bp}. However, the results of some experimental tests (e.g., Gómez *et al*. (2010) and Kanvinde *et al*. (2015)) show that M_n^{bp} is in general, considerably larger than M_y^{bp} and smaller than M_{max}^{bp} (see Figure 5-2). This concept is properly conservative for strength design, but it could overestimate the initial stiffness K_0^{bp} ($=M_y^{bp}/\theta_y^{bp}$) and the yielding rotation θ_y^{bp} ($=M_y^{bp}/K_0^{bp}$), according to the models proposed by Kanvinde *et al*. (2015) and Torres-Rodas *et al*. (2016), respectively. Also, an overestimation of K_0^{bp} by Eurocode 3:1-8 is reported by Latour *et al*. (2014).
- some of the core parameters to characterize the start of the plastic range (e.g., K_0^{bp}, M_y^{bp} and θ_y^{bp}), are not explicitly identified by Ermopoulos and Stamatopoulos (1996). Furthermore, these authors have made efforts to simplify the model, although this model still entails extrapolation and iterations to obtain characteristic coefficients given for specific pre-assumed stress distributions under the ECBP, which is not convenient to balance sophistication vs accuracy for the sake of implementation in standards and use by practical engineers.
- the influence of the *ACR* on the rotational capacity of the connections are not considered in published models. The rotational behavior of the ECBP system is interdependent with the rotational capacity of the columns, according to the results of Elkady and Lignos (2015), and Mohabeddine *et al*. (2021).

5.3 New database of experimental tests on ECBP subjected to flexure and axial loads

A systematic assemblage of experimental data was developed and made available in https://cbp-db-modelling.utb.edu.co/search. The database contains information from tests aimed at obtaining individual parameters (e.g., M_{max}^{bp}) or the full range of the M-θ curves of ECBP with shallow column sections. The metadata can be grouped into three categories: (i) test setup, (ii) reported results, and (iii) deduced data. For the former category, the following variables are defined as reported by each author (see Table 5-2):

- column section: wide flange (e.g., HEA, W and HEB) or Hollow Structural Sections (HSS)
- loading type: monotonic, cyclic, constant or variable
- *ACR* from 0% (no axial loads) to around 63%
- bolt pattern: 1 row-1 bolt, 2 rows-4 bolts, 2 rows-6 bolts or 3 rows-8 bolts
- thickness of plate t_p and diameter of bolts D_b: from 12 mm to 32 mm
- bolt-installation-method: pretensioned, cast-in-place, epoxy drilled or undercut bolts
- measured materials properties as reported in the referenced text documents.

The second category contains the values for θ_y^{bp}, θ_{max}^{bp}, M_y^{bp} and M_{max}^{bp}, as observed from each reference (see Table 5-2). For the third category, as the parameters θ_1^{bp}, C_M and C_θ are exclusively referred to the trilinear model defined in sub section 5.2, their values are not directly reported by previous authors (see Table 5-2) and therefore, these parameters are determined from the backbone M-θ curves, by shaping the trilinear curves to match the experimental curves (i.e., backbone of cyclic, or, monotonic); this methodology is similar to that used by Lignos and Krawinkler (2011) for other cases than ECBP. Besides, additional indicator parameters (e.g., L_{col} / d and m / t_p) are included for the sake of determining the relevant variables on the prediction of

the modeling parameters of ECBP through multiple regression analysis, as explained in the following sections.

The test results of 84 specimens in total were analyzed. The data for cyclic curves correspond to 42 specimens (e.g., tests by Gómezs *et al*. (2010) and Kanvinde *et al*. (2015); see Table 5-2), which were more recently tested as compared to early monotonic tests by Picard and Beaulieu (1985) and, Jaspart and Vandegans (1998). The M-θ curves of the tests led by the second author ((Gomez et al., 2010; A. M. Kanvinde et al., 2015)) were provided in digital format, whereas the other experimental curves were digitized graphically. An Excel-based tool was created to facilitate the following steps during the process: data collection, plotting and editing of M-θ curves. In addition to the references collected in the database (see Table 5-2), several other experimental studies on ECBP were analyzed, however these were found out of the scope of this study for a range of reasons, as summarized in Table 5-3.

Table 5-2. Summary of specimens and loading types in the experimental tests database

Author	Specimens (-)	Loading type (-)	Author	Specimens (-)	Loading type (-)
(Picard & Beaulieu, 1985)	8F, 9F	Mon/V_u, M_u=Var/P_u= 0	(Choi & Choi, 2013)	ECB19SCUY0	Cyc/V_u, M_u=Var/P_u= Con
	12F, 13F			ECB9SCUY1	
(Thambiratnam & Paramasivam, 1986)	1, 3, 4, 5	Mon/V_u, M_u, P_u=Var	(Demir et al., 2014)	E1	Cyc/V_u, M_u=Var/P_u= 0
	7, 8		(A. M. Kanvinde et al., 2015)	1, 2, 3, 4	Cyc/V_u, M_u=Var/P_u= 0
	9, 11, 12			5, 6	Cyc/V_u, M_u=Var/P_u= 0
(Wald et al., 1994)	W8	Mon/V_u, M_u=Var/P_u= 0		7, 8	
	W7, W10, W12	Mon/V_u, M_u, P_u=Var	(Latour et al., 2014)	HE240B-15-585	Mon/V_u, M_u=Var/P_u= Con
(Jaspart & Vandegans, 1998)	PC4.15.100, -400, -1000	Mon/V_u, M_u=Var/P_u=Con		HE240B-25-585	
	PC4.30.100, -400, -1000			HE160A-15-34	Mon/V_u, M_u=Var/P_u= Con
(Wheeler et al., 1998)	11, 17	Mon/V_u, M_u=Var/P_u= 0		HE160A-15-233	
	12, 18, 23, 24		(Trautner et al., 2016)	S1S1, S1S2 S1S3, S1S4	Cyc/V_u, M_u=Var/ P_u= 0
	13, 19			S2S1, S2S2 S2S3, S2S4	
(Fahmy et al., 1999)	W10x77	Mon/V_u, M_u=Var/P_u= 0	(Trautner et al., 2017)	S3S1	Cyc/V_u, M_u=Var/ P_u= Con
(Burda & Itani, 1999)	T1, T4	Mon/V_u, M_u=Var/P_u=Con		S3S2, S3S3, S3S4, S3S5	Cyc/V_u, M_u=Var/ P_u= 0
	T2, T5			S4S1, S4S2 S4S3, S4S4	
	T3, T6				
(Gomez et al., 2010)	1	Mon/V_u, M_u=Var/P_u= 0	(You & Lee, 2020)	SR1, SR2, SR3	Cyc/V_u, M_u=Var/ P_u= Con

Table 5-2. Summary of specimens and loading types in the experimental tests database

Author	Specimens (-)	Loading type (-)	Author	Specimens (-)	Loading type (-)
	2	Cyc/V_u, M_u=Var/P_u= 0		SR4	
	3			ST2	
	5, 7	Cyc/V_u, M_u=Var/P_u= Con		ST4	
(Gomez et al., 2010)	4	Cyc/V_u, M_u=Var/P_u= Con		ST5	
	6				
∑	-	-	-	84 specimens	-

Mon: monotonic, Var: variable, Con: constant, Cyc: Cyclic

Table 5-3. Summary of experimental studies on column bases that are out of the scope of this study					
Ref.	Criteria	Ref.	Criteria	Ref.	Criteria
(Hon & Melchers, 1988)	1 row-2 bolts pattern, only axial loads	(Della Corte & Landolfo, 2017)	Battened Steel columns	(D. Grilli et al., 2017)	Embedded connection
(Di Sarno et al., 2007)	Composite columns	(Freddi et al., 2017)	Rocking damage-Free connection	(Santos & Leitão, 2017)	Self-centering, low-damage ECBP
(Yeow et al., 2018)	Friction low-damage connection	(Chi & Liu, 2012)	Rocking, post-tensioned, with grade beams	(Kavoura et al., 2017)	Pinned connections
(Kamperidis et al., 2018)	Rocking, post-tensioned	(Latour et al., 2019)	Rocking, low yielding, with friction dampers	(DeWolf & Sarisley, 1980)	A-bolts in idealized anchoring state
(Takamatsu & Tamai, 2005)	Self-centering, slip type	(Wang et al., 2019)	Self-centering, Composite column	(D. A. Grilli & Kanvinde, 2015)	Embedded connection
(Kayani & W. Tabsh, 2012)	Data for M-θ curves are not available	(Lim et al., 2017)	Weak axis of column	(Zhou et al., 2004)	ECBP with grade beams
(Melchers, 1992)	Pinned ECBP	(Cui et al., 2009)	Embedded connection through grade beams and slabs	(D. Y. Lee et al., 2008)	Weak axis
(Pertold et al., 2000)	Embedded connection	(Rodas et al., 2017)	Embedded connection	(Targowski et al., 1993)	Pure flexure state

5.4 Selection of predictor variables

There is a lack of specific modeling parameters for components (i.e., ECBP) in SMRF, in a code-based framework, as stated by Gutiérrez-Urzúa *et al*. (2021). Data-driven models have increasingly been used by researchers to fill this gap (e.g., regression models by Lignos and Krawinkler (2011) and, machine-learning models by Kabir *et al*. (2021)). In these models, a careful selection of predictor variables is needed to avoid overfitting and thus, reach an adequate predictive performance. In this study, the selection is codependent on the regression process itself. This section summarizes the initial selection method followed, which corresponds to the filter method suggested by Sun *et al*. (2021). The final selection of variables for each predictive equation of modelling parameters, was made after the regression process explained in subsection 5.5.

5.4.1 Identification of potential predictor variables

The first step identified the important potential variables from a behavioral standpoint (which are in general combinations of test parameters); these variables are input to the predictive equations for the modelling parameters of ECBP. The variables contained in some published analytical models to determine the strength, stiffness or ductility of ECBP (Latour and Rizzano (2019) and (2013), and, Kanvinde *et al.* (2015) and (2012)) were preliminary selected to latterly test their statistical significance. Forty-one variables were identified from these models. Then, a reduction of variables was made to reach a satisfactory trade-off between accuracy and simplicity in the regression analyses. This reduction accounted for: (i) the main conclusions from some studies (experimental and numerical) compiled in the database described in subsection 5.3, (ii) the subjectivity in the definition of some variables, as explained by the authors, (iii) the obvious collinearity between some variables, which is recognized as undesirable for predictive models (Chatterjee and Hadi (2015)). Next, there is a briefly discussion on the physical significance of some potential predictor variables and adopted criteria for excluding them:

- Rod-edge distance, rod length and distance between rods. These variables are commonly a function of the bolt's diameter D_b, the cross area of bolts in the tensile side A_{rod} and, the plate width and length (B and N). The variables B, N, A_{rod} and D_b have shown to be determinant for the structural behavior of ECBP (see Gómez *et al.* (2010) and Trautner *et al.* (2017)); then, these were maintained to test their statistical significance later. Other variables with direct dependance on these selected (e.g., the moment of inertia of the plate section in bending), were also tested as explained in subsection 5.4.2.
- Concrete and welding - dimensions and material properties. The concrete footings and welding of ECBP should be designed to behave elastically (e.g., according to as prescribed by the American design guide (Fisher & Kloiber, 2006) and Diaz *et al*. (2020)). Also, the expected in-field behavior of these connections may not be controlled by concrete properties, but the interaction with surrounding soil and other challenging phenomena that are not encompassed so far in the models adopted by the standards (see discussions by Kanvinde *et al*. (2013), Latour and Rizzano (2019)). Lastly but not less important, it can be observed in the dataset that the tests entailed similar values of concrete properties, while the modeling parameters indicate a wide range of values. Therefore, the concrete properties clearly show poor statistical significance for predicting these parameters.
- Loads and resistance factors for design, coefficients of models. These are fixed parameters by models or standards, then have no significance for prediction purposes.
- Steel elements – material properties. The values of the yielding and ultimate stresses of steel elements in the dataset show a wider range than their moduli of elasticity (see Gómez *et al*. (2010) and Trautner *et al*. (2017)). Besides, for design purposes, these moduli are commonly fixed by standards (e.g., DG1 (Fisher & Kloiber, 2006)). Based on these analyses, the yielding stresses of the plate and bolts (F_{yp} and F_{yb}) are selected as potential predictor variables. On the other hand, the yielding stresses of other steel elements (column, nuts and

washers) are neglected because these showed minor influence on the behavior of ECBP during test campaigns.

- Column dimensions. The findings in Gómez *et al*. (2010) displays the deformation contribution of flexible columns to the drift deformation is relatively large. Therefore, the ratio of the column length to the column-section height L_{col} / d was conveniently selected as a potential predictor variable to point out predominant flexural or axial load transfer instead of shear load one (e.g., as L_{col} / d is greater). In addition, experiments with slender columns by Kanvinde *et al*. (2015) and short columns by You and Lee (2020), indicate that this mentioned ratio, is directly related with the moment-to-shear ratio for the joint, and then, with the load transfer mechanics. In this study, when the test specimens have a column in cantilever, a coefficient of 2 is applied to L_{col} for calculating the ratio L_{col} /d, assuming a classical Euler´s general-buckling approach. Apart from the abovementioned, only standard columns are used in the tests, which normally fulfil the limits of width-to-thickness ratios prescribed by standards. Given these considerations, the thickness and width of the column section were excluded.
- Plate dimensions. Several variables are comprised in the analytical models reviewed herein. Many of these depend on plate dimensions that were selected (e.g., B and N), then to avoid collinearity issues, many of these variables were extracted. The thickness t_p was selected because this variable is in consensus, one of the most influent on the response of ECBP. In addition, the ratio m / t_p was conveniently selected as potential predictor, to consider the effect of thinner plates on the rotational deformation of these joints; where $m = (N - d) / 2$. This effect has been pointed by Gómez *et al*. (2010).
- Axial loads. Analytical (e.g., Latour and Rizzano (2019), and Kanvinde *et al*. (2012)) and experimental findings (e.g., Jaspart and Vandegans (1998)), have revealed the paramount influence of axial loads on the stiffness of ECBP. Low axial loads are expected to increase the initial stiffness of ECBP, whereas high axial loads tend to reduce the initial stiffness of these connections. In line with these findings, the *ACR* was selected as a potential predictor.

According to the discussion presented herein, there are twelve potential predictor variables in total, which are listed next:

- yielding stress of anchor rods F_{yb}
- yielding stress of plate F_{yp}
- length of plate N
- width of plate B
- thickness of plate t_p
- cross sectional area of bolts group in the tensile side A_{rod}
- diameter of bolts D_b
- Axial Compression Ratio *ACR*
- moment of inertia of the plate section in bending I_{plate} (= $B\ t_p^3$ / 12)
- cross sectional area of the plate in bending A_{plate} (= $B\ t_p$)
- ratio to study the effects of slender columns L_{col} / d
- ratio to study the effects of thinner plates m / t_p

5.4.2 Predictive significance of predictor variables

The second step tested the predictive significance of the variables selected in subsection 5.4.1, to filter them. For instance, the most significant predictor between: (i) A_{plate}, I_{plate} and B (ii) D_b and A_{rod}, had to be selected because of its obvious collinearity. For this purpose, three criteria were considered:

- Analysis of scatter plots and slopes of linear regression lines. A linear regression analysis was individually performed between each modeling parameter in the database (i.e., those defined in subsection 5.2), and each of the selected variables in subsection 5.4.1, to show

their dependance or correlation. Regarding these regressions, horizontal regression lines theoretically indicate no dependance of the modeling parameters on the referred variable. On the other hand, the steeper the regression line, the more predictive significance the variable might have.

- Calculation of the correlation coefficient (R^2) for each linear regression. The greater value of R^2, the greater predictive significance that any predictor variable has.
- Performing *t*-tests. The larger the value of $|t|$, the more significance a predictor variable might show in regression equations, namely, more predictive significance. In simple linear-regression problems (only one predictor variable), $|t|$ should be greater or equal to 1.67, to get a confidence level of 95%.

Although the simple linear regressions illustrate the trends and dependences of the modeling parameters on the predictor variables, these regressions are not adequate to predict the parameters. To illustrate the criteria mentioned above, Figure 5-3a and b show the scatter plots and linear regressions between the yielding strength of ECBP and, B and I_{plate}, respectively. The median X and deviation S for each variable are shown also. The figure shows that B has greater values of R^2, $|t|$ and slope of the regression line, thus B might be a better predictor variable of the yield strength of ECBP than I_{plate}.

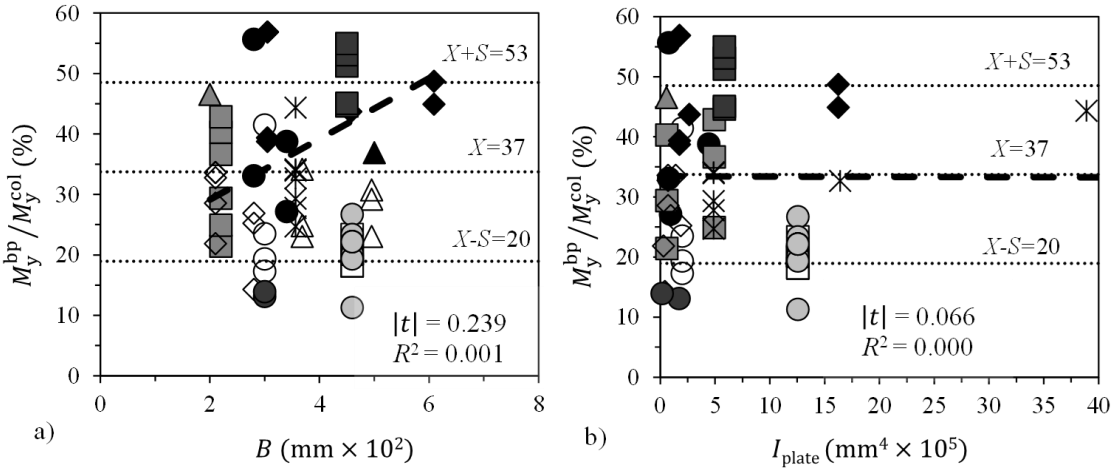

Figure 5-3. Scatter plots and linear regression between the yielding strength parameter and two predictor variables

After the analysis of the scatter plots and linear regressions between all the potential predictors (see subsection 5.4.1) and modelling parameters (see subsection 5.2), the variables B and A_{rod} were found to show more significance as predictor variables; therefore A_{plate}, I_{plate} and D_b were excluded. The statistical analysis was performed with the help of the free software JASP© (2023). Table 5-4 summarizes the values of R^2 and $|t|$ of the linear regressions performed for all the selected predictor variables. For example, the table shows that F_{yp} is highly significant to predict the yielding rotation θ_y^{bp} (high values of R^2 and $|t|$ were calculated, 0.312 and 5.266, respectively). On the opposite, F_{yp} should display poor predictive performance of the ultimate rotation θ_{max}^{bp} (low values of R^2 and $|t|$ were respectively computed as, 0.000 and 0.147).

Table 5-4. Summary of significance evaluation of predictor variables

Description	θ_y^{bp}		θ_{max}^{bp}		θ_1^{bp}		C_M		C_θ		$\frac{M_y^{bp}}{M_y^{col}}$		$\frac{M_{max}^{bp}}{M_y^{col}}$	
	$\|t\|$	R^2	$\|t\|$	R^2	$\|t\|$	R^2	$\|t\|$	R^2	$\|t\|$	R^2	$\|t\|$	R^2	$\|t\|$	R^2
F_{yb}	2.838	0.117	1.691	0.050	2.861	0.157	0.525	0.006	2.122	0.101	1.743	0.047	1.768	0.037
F_{yp}	5.266	0.312	0.147	0.000	4.260	0.292	2.161	0.089	0.521	0.007	2.334	0.082	0.666	0.005
N	0.779	0.010	1.057	0.020	1.678	0.060	1.908	0.070	1.216	0.036	0.501	0.004	0.125	0.000
B	0.367	0.002	0.215	0.001	0.062	0.000	1.985	0.076	0.967	0.023	0.239	0.001	0.530	0.003
t_p	1.612	0.041	1.445	0.037	1.341	0.039	1.897	0.070	0.185	0.001	0.537	0.005	0.088	0.000
A_{rod}	0.407	0.003	2.421	0.098	1.511	0.049	0.087	0.000	2.113	0.100	2.623	0.101	3.238	0.113
ACR	1.304	0.027	0.006	0.000	2.674	0.140	1.152	0.027	1.038	0.026	1.715	0.046	2.051	0.049
L_{col} / d	3.040	0.132	1.208	0.026	5.873	0.439	1.711	0.068	0.055	0.000	0.071	0.000	0.509	0.003
m / t_p	2.777	0.112	4.052	0.233	5.125	0.374	0.185	0.001	2.220	0.110	0.740	0.009	0.444	0.002

After selecting the nine predictor variables (subsection 5.4.1), the Pearson´s correlation coefficient *r* is used to measure the linear correlation between these predictors (see Table 5-5). This coefficient is a number between -1 and 1. The closer *r* is to -1 or 1, the stronger is the linear relationship between two evaluated variables (Chatterjee and Hadi ("Simple Linear Regression," 2006)). In the table, the highest linear correlation is shown between *B* and *N* ($r = 1$). It shall be spelled out that the testing of significance performed in this subsection does not necessarily means that a variable showing a high value of R^2, $|t|$ or *r* cannot be latterly considered in regression process; this is because the criteria mentioned above do not consider other predictors simultaneously, e.g., like is considered in multivariate regression analysis. The main purpose of this evaluation is to filter predictor variables and avoid obvious collinearities between predictors, as recommended by some authors (Aladsani *et al*. (Aladsani et al., 2022), Sun *et al*. (Sun et al., 2021)).

Table 5-5. Pearson´s correlation coefficient r between predictor variables

Variable	L_{col} / d	F_{yb}	N	m / t_p	B	F_{yp}	t_p	A_{rod}	ACR	1.000
L_{col} / d	-									0.750
F_{yb}	0.265	-								0.500
N	0.225	0.249	-							0.250
m / t_p	0.274	0.257	0.342	-						0.000
B	0.201	0.204	0.900	0.158	-					
F_{yp}	0.731	0.385	-0.030	0.242	0.005	-				-0.250
t_p	0.132	0.022	0.535	-0.413	0.535	-0.244	-			-0.500
A_{rod}	-0.031	0.272	0.491	-0.176	0.556	-0.006	0.539	-		-0.750
ACR	-0.533	-0.251	-0.295	-0.089	-0.289	-0.385	-0.226	-0.212	-	-1.000

5.4.3 Selected predictor variables

Table 5-6 shows the distribution of the nine selected predictor variables, with corresponding units inside brackets, similarly as compiled in the database. C_1, C_2 and C_3 are coefficients for units' conversion from international (e.g., millimeters and megapascals) to imperial units (e.g., inches and ksi). Accordingly, these coefficients are equal to 1.0 if international units are used, and, respectively equal to 0.145, 3.937×10^{-2} and 1.550×10^{-3} if imperial units are chosen.

Table 5-6. Distribution of predictor variables				
Predictor variable	Mean (X)	Standard deviation (S)	Min	Max
F_{yb} (MPa C_1)	569.2	210.6	240.0	830.0
F_{yp} (MPa C_1)	269.9	39.34	235.0	354.0
N (mm × 10^2 C_2)	3.671	1.007	2.000	6.090
B (mm × 10^2 C_2)	3.418	1.179	1.778	6.090
t_p (mm C_2)	24.67	8.874	9.000	69.85
A_{rod} (mm^2 × 10^2 C_3)	6.452	2.944	2.262	23.75
ACR (%)	9.641	14.69	0.000	72.09
L_{col} / d (1)	18.02	10.53	6.000	50.39
m / t_p (1)	3.954	1.456	1.500	8.667

5.5 Regression equations for the modelling parameters

In this section, regression equations are provided to predict the parameters for M-θ curves of ECBP, according to the selected trilinear-model (see subsection 5.2). The whole procedure used to determine these equations is summarized as follows:

- The experimental values of predictor variables and backbone M-θ curves of ECBP were compiled in the database, as explained in subsection 5.3.
- A trilinear M-θ curve for each of the experimental curves, was defined to fit the backbone of experimental curves, as explained in subsection 5.2.
- The modeling parameters of the trilinear curves were arranged in the database.
- Individual linear regressions were made to test the predictive significance and filter potential predictor variables, as explained in subsection 5.4.2.
- Regression equations were defined through a backward elimination process considering all the predictor variables for each regression equation, to select the final predictor variables for each parameter, and train each predictive model as recommended by Chatterjee and Hadi (2006).

The software JASP© (2023) was used to facilitate the statistical simulation process. Chatterjee and Hadi (2006) states that the variables to be finally selected for regression models are linked to the specification of the equations. After several tests with different type of equations, multiple-nonlinear-regressions were selected for predicting the modeling parameters because these regressions showed better correlation and *t*-values than others. The fitting of nonlinear instead of linear equations for the modeling parameters of ECBP can be explained by the fact that the yielding of plates in the joint occurs at initial loading stages, as observed in most of the test campaigns reported in the dataset. The general nonlinear form of the predictive equations is shown in Eq. (5-3).

$$Y = \beta_0 \left(\frac{L_{col}}{d} + C \right)^{\beta_1} \cdot \left(F_{yb} + C \right)^{\beta_2} \cdot \left(N + C \right)^{\beta_3} \cdot \left(\frac{m}{t_p} + C \right)^{\beta_4} \cdot \left(B + C \right)^{\beta_5} \cdot \left(F_{yp} + C \right)^{\beta_6} \cdot \left(t_p + C \right)^{\beta_7} \cdot \left(A_{rod} + C \right)^{\beta_8} \cdot \left(ACR + C \right)^{\beta_9} - C \tag{5-3}$$

where Y is the so-called response or dependent variable (e.g., the predictive modeling parameter in this work), and β_0 to β_n are the regression coefficients. The predictive equations proposed in this research are summarized in Table 5-7, following the fashion of Eq. (5-3). These equations

were found to be the best-fit for predicting the modeling parameters of ECBP, following the methodology of this research. The statistical metrics Root Mean Square Error (*RMSE*), mean *X*, number of specimens *n* and correlation coefficient R^2 were calculated and included in the table. These metrics were used to evaluate the goodness of the fit, next (see subsection 5.6).

Table 5-7. Predictive equations for the modelling parameters of ECBP

Parameter	Equations´ coefficients (1)											Predictive performance (1)			
	C	β_0	β_1	β_2	β_3	β_4	β_5	β_6	β_7	β_8	β_9	*n*	R^2	*RMSE*	*X*
θ_y^{bp}	1.000	7.568×10^{-3}	-0.143	0.000	-0.236	0.339	0.000	0.955	0.116	-6.000×10^{-3}	-0.025	63.00	0.410	0.310 %	0.700 %
θ_{max}^{bp}	1.000	1.607	0.000	-0.363	-2.631	1.988	0.745	0.000	1.198	-0.040	0.103	56.00	0.456	2.990 %	8.610 %
θ_1^{bp} [1]	1.000	2.754×10^{-2}	0.007	0.000	0.785	0.358	-0.920	0.855	0.000	-0.037	-0.048	46.00	0.590	1.010 %	3.350 %
C_M [2]	0.100	5.649×10^{-4}	-0.161	0.036	0.525	-0.200	-0.582	1.522	-0.193	0.045	0.008	42.00	0.224	0.090	0.930
C_θ [2]	0.100	2.075×10^{-4}	-0.077	0.033	1.536	-0.840	-1.063	1.861	-0.677	0.201	0.026	42.00	0.313	0.170	0.750
$\frac{M_y^{bp}}{M_y^{col}}$ [3]	1.000	0.038	0.025	0.315	3.028	-1.611	-0.942	1.367	-1.254	0.000	-0.037	63.00	0.539	10.60 %	32.70 %
$\frac{M_{max}^{bp}}{M_y^{col}}$ [4]	1.000	0.075	-0.041	0.000	1.306	-0.523	-1.304	1.398	-0.418	0.507	0.075	76.00	0.435	22.00 %	59.80 %

[1] For pretensioned bolts, $\theta_1^{bp} = 0.51\ \theta_{max}^{bp}$.

[2] For pretensioned bolts, $C_M = C_\theta = 1$.

[3] For this equation, the result shall be factored by the empirical coefficient $C_{M_y}^{FTB}$. This is 1.500 when cast-in fully threaded bolts are used. For other cases, $C_{M_y}^{FTB}$ shall be 1.000.

[4] For this equation, the result shall be factored by two empirical coefficients ($C_{M_{max}}^{PB}$ and $C_{M_{max}}^{FTB}$). For pretensioned bolts only, $C_{M_{max}}^{PB}$ shall be equal to 0.640. For other cases, $C_{M_{max}}^{PB}$ shall be equal to 1.000. Besides, for fully threaded bolts $C_{M_{max}}^{FTB}$ shall be 1.400. For other cases, $C_{M_{max}}^{FTB}$ shall be 1.000.

5.6 Evaluation and discussion of model´s performance

5.6.1 Prediction of individual modelling parameters

This subsection discusses the predictive performance of the proposed equations (Table 5-7), by comparing measured versus predicted modelling parameters, both the fit to individual parameters and the full range of M-θ curves. In addition, validation was made by comparing predicted against experimental data which were not considered to train the predictive equations (e.g., tests on deeper wide flange columns by Cravero *et al*. (2020)). A discussion on the most significant predictor variables from the equation's coefficients and its physical meaning, is provided.

5.6.1.1 Rotational parameters

Table 5-7 shows that the best-fit predictive equations for the rotational parameters include 7 of 9 selected predictor variables. The predictive equation for θ_y^{bp} (Table 5-7) shows relatively high values of the regression coefficients for F_{yp}, m / t_p, N, L_{col} / d and t_p, which indicate strong dependence of θ_y^{bp} on these predictor variables; mostly confirms the trends previously suggested (e.g., these variables display high values of $|t|$ and R^2 in linear regression against θ_y^{bp}, see Table 5-4). On the other hand, notwithstanding F_{yb} was previously identified as a potential predictor variable of θ_y^{bp}, finally the proposed equation in Table 5-7 does not include it. It shall be remarked that a potential predictor does not mandatorily need to go in the predictive equation with the best fit, as stated by Chatterjee and Hadi (2006). In Table 5-7, the equation for θ_{max}^{bp} points out that N, m / t_p, A_{rod} and B are the most influential predictor, because their regression coefficients are relatively larger than others. On the analysis of equations for the yielding and ultimate rotations (θ_y^{bp} and θ_{max}^{bp}), the rods yielding-strength ($A_{rod} \times F_{yb}$) and the *ACR* are more influential for θ_{max}^{bp} than for θ_y^{bp}. This conclusion is aligned with experimental observations by Trautner *et al*. (2017), this is θ_y^{bp} shows low variance upon the rods tensile-strength.

Regarding θ_1^{bp}, the predictor variables F_{yp} and N are the two most influential (e.g., see Table 5-7); this observation indicates that the size and material properties of the steel plate influence on the predicted values of θ_1^{bp}. A similar conclusion can be deduced from experimental tests by Burda and Itani (1999), where the size of the steel plate is parametrized. For the subset with pretensioned bolts (17 specimens), the sample size is not adequate to develop the same statistical analysis as done for the full dataset; for this case, θ_1^{bp} can be empirically predicted as 0.51 θ_{max}^{bp}, where θ_{max}^{bp} can be predicted with the corresponding predictive equation, proposed in Table 5-7. Figure 5-4 shows the relation between predicted and experimental values of the rotational parameters.

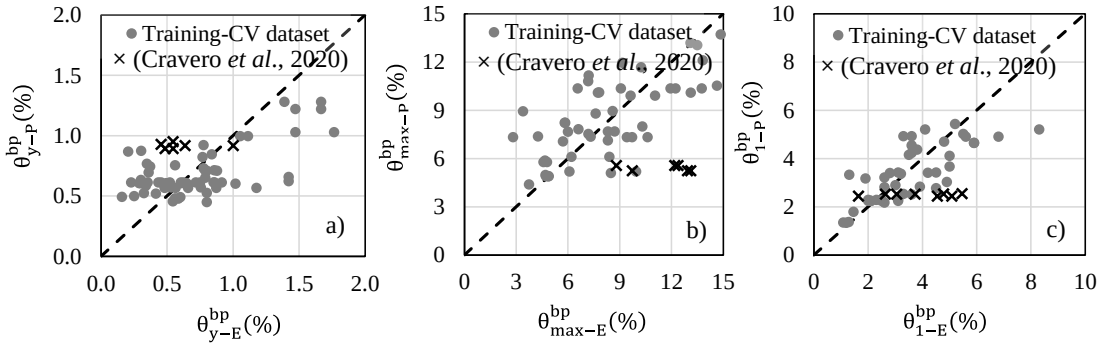

Figure 5-4. Predicted vs. Experimental values of the rotational parameters of ECBP

Overall, the predicted rotational parameters of ECBP using the equations proposed (see Table 5-7) have reasonable correlation with experimentally measured parameters in the database. It should be noticed that the correlation of predicted individual-parameters is normally lower than the correlation of M-θ curves (e.g., see Lignos and Krawinkler (2011)). The values of R^2 for the predicted values of θ_y^{bp}, θ_{max}^{bp} and θ_1^{bp} are 0.410, 0.456 and 0.590, respectively. In the same order, the average values of the predicted rotations are 0.7 %, 8.6 % and 3.3 %, respectively; these values are like experimental ones 0.7 %, 9.4% and 4.2 %.

5.6.1.2 Post-capping degradation parameters

The regression equations for post-capping degradation parameters needed all nine selected predictor variables to reach the best-fit (see Table 5-7) for the full set of data, which were set based on 42 specimens. It should be noticed that the variables are added with a constant 0.1 instead of 1.0 (e.g., as considered for rotational parameters), because the values of degradation parameters are expected to be smaller than 1. Furthermore, for practical purposes, the predicted values of the parameters are limited to 1.

The correlation coefficients for the predicted values of the parameters C_M and C_θ (equal to 0.224 and 0.313, respectively) are smaller than those for the rotational and strength parameters, especially for C_M. However, these predictions were found reasonably accurate when the full-range of predicted M-θ curves were plotted, as shown in subsection 5.6.2; besides, the comparison of the means of the predicted and experimental values of C_M and C_θ also show good accuracy; these means are 0.93 and 0.91 for the former parameter, while 0.75 versus 0.71 for the second one, respectively. Since pretensioned bolts cause that the ECBPs have a self-centering behavior (Trautner *et al*. a (2016) and b (2017)), the degradation parameters C_M and C_θ for the subset pretensioned bolts are rather different than for the full dataset. These parameters can be reliably estimated as 1 for this data subset, instead of the predicted values with the proposed equation (Table 5-7).

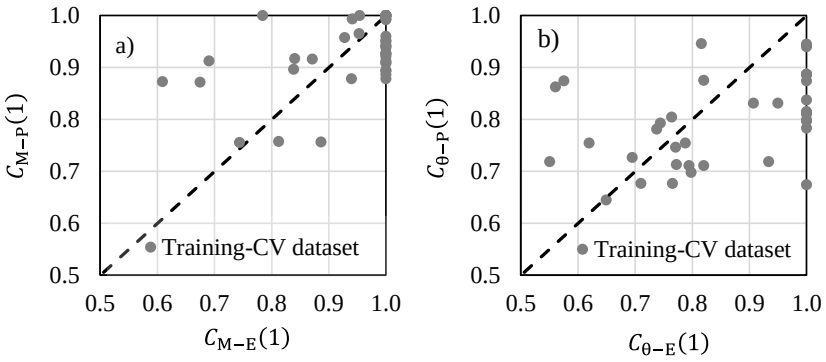

Figure 5-5. Predicted vs. Experimental values of the degradation parameters of ECBP

The analysis of the scatter plot in Figure 5-5a, indicates also that the correlation between predicted and experimental values of C_M is relatively low. The following observation can be considered as a potential reason to study: even though most of the predictor variables are parametrized within the full database, the width-thickness ratios of the column sections are not. The results of the study by Lignos and Krawinkler (2011) on beam-to-column joints, point out that these ratios have a significative influence on the deterioration parameters of the connections. Accordingly, the parametrization of the width-thicknesses ratio of column web and flanges is highly recommended to be studied in future works, in order reduce the dispersion of the predicted C_M and C_θ.

5.6.1.3 Strength parameters

There are 17 specimens with pretensioned bolts (those under tensile pre-loads of around 30% of $A_{rod} \times F_{yb}$); these have notably lower normalized strength $M_{max}^{bp} / M_{y}^{col}$ than the specimens in the full dataset (e.g., see Trautner *et al*. (2017)). In addition to the effect of pretensioned bolts, there are 5 specimens with fully threaded bolts, which showed to cause an increment on the strength parameters (e.g., see You and Lee (2020)). Such a few specimens elicit a low significance regression analysis if a specific equation for the subset is developed. For instance, after applying the backward elimination process for a specific equation for the subset pretensioned bolts, excessive variables appeared as collinear. Therefore, after several tests on three datasets (i) full dataset (ii) pretensioned bolts (iii) fully threaded bolts, the best-fit predictive equation for M_{y}^{bp} / M_{y}^{col} is given as shown in Table 5-7. In this equation, the empirical coefficient $C_{M_y}^{FTB}$ shall be 1.5 when cast-in fully threaded bolts are used. For other cases, $C_{M_y}^{FTB}$ shall be 1.

Regarding $M_{max}^{bp} / M_{y}^{col}$, the predictive equation shown in Table 5-7 shall be used for any specimen; then, the empirical coefficient $C_{M_{max}}^{PB}$ is equal to 0.64 for pretensioned bolts subset; for cast-in fully threaded bolts, $C_{M_{max}}^{PB}$ is 1. In this equation, the empirical coefficient for fully threaded bolts $C_{M_{max}}^{FTB}$ shall be 1.4. For other cases, $C_{M_{max}}^{FTB}$ shall be 1.

The best-fit equations for the yielding and ultimate strength of ECBP (see Table 5-7) need minimum eight predictor variables. The correlation coefficients of the predicted strength parameters M_{y}^{bp} / M_{y}^{col} and $M_{max}^{bp} / M_{y}^{col}$ are 0.539 and 0.435, respectively. The average values of predicted parameters are 33% and 60% (for the full dataset) in the same order, while the corresponding experimental values are 37% and 61%. The analysis of the scatter plot of predicted versus experimental strength-parameters (see Figure 5-6) confirms the wellness of the fit.

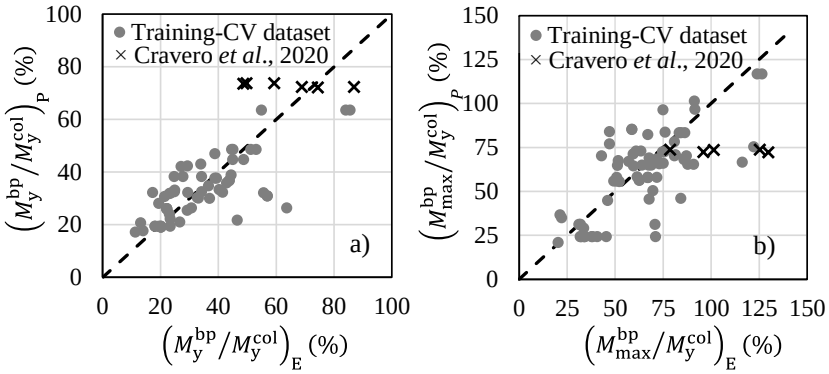

Figure 5-6. Predicted vs. Experimental values of the strength parameters of ECBP

5.6.2 ***Prediction of the full-range of M-θ curves***

In addition to the examination of the scatter plot of data and the index R^2 for predicting individual parameters (see subsection 5.6.1), the use of the index R^2 can be used to assess the quality of the fit of predictive equations to the full-range of M-θ curves of ECBP. The closer R^2 to 1, the higher quality of the fit of the regression equations proposed in this work (see Chatterjee and Hadi (2006)). Figure 5-7a to p show that the proposed models have high accuracy on predicting these curves. The median for the coefficient R^2 between the 56 predicted and experimental full-range curves (e.g., monotonic and cyclic) is equal to 0.91, which indicates a prediction accuracy of 91% on average. Figure 5-7p displays the M-θ curve for specimen E1, tested by Demir *et. al*. (2014), for which the fit is not particularly pleasing; it can be observed that predicted curve notably sub

estimate the yielding strength of the connection; this sub estimation might be explained with the fact that this testing specimen was particularly stiffened, while the effects of stiffening on the connection response is not explicitly being considered in the proposed equations. These effects of stiffening on the response of ECBP have been studied by Diaz *et al*. (2020). Also, a sub estimation of the yielding strength is observed for specimens 1 and 3 by Kanvinde *et al*. (2015) (Figure 5-7e and f); in this case, a 3 rows-8 bolts pattern tested have been found to provide more stability and stiffness than commonly used 2 rows-6 or 8 bolts.

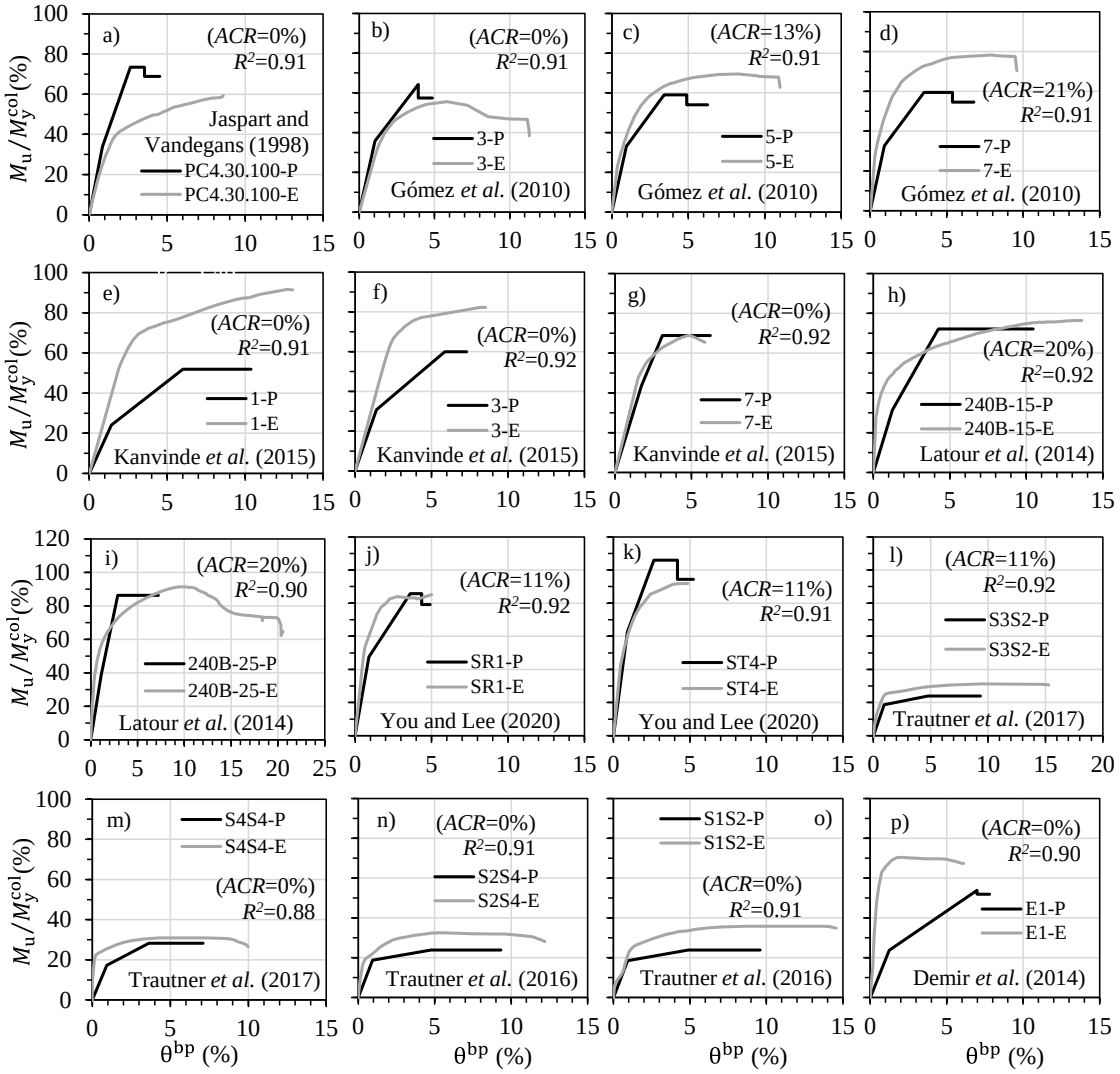

Figure 5-7. Full-range of predicted M-θ curves for various specimens in the compiled database

Although the proposed equations (Table 5-7) in this study show satisfactory agreement with experimental results, the range of parameters used in the regression process (see Table 5-6) shall be considered for the sake of obtaining an adequate significance level of prediction. Despite that there are two studies in the database with some values of *ACR* greater than 25 % (e.g., Thambiratnam and Paramasivam (1986) and Wald *et al*. (1994)), it shall be stated that the test assemblages for these works contemplate variable vertical loads and moments. Then, the *ACR* registered in these cases is the maximum *ACR* (e.g., at the failure moment). For the rest of the tests in the full dataset, the axial load is constant, which is more comparable to the situation of ECBP in MRF buildings under seismic excitations.

A complementary web-based tool was developed to calculate the modelling parameters of ECBP using the proposed equations (Table 5-7). The tool has an intuitive interface, which follows the same notation of this paper. For the sake of illustration, Figure 5-8 shows a screenshot of the tool, corresponding to the prediction of the modelling parameters for the specimen S2S4 by Trautner *et al*. (2016). In the figure, the input data are (i) the nine predictor variables, located at the left side of the screen (ii) the selection of the bolt's installation method (e.g., pretensioned bolts and cast-in fully treaded bolts). The output data are the predicted modelling parameters and the plot of the full-range of M-θ curves of ECBP.

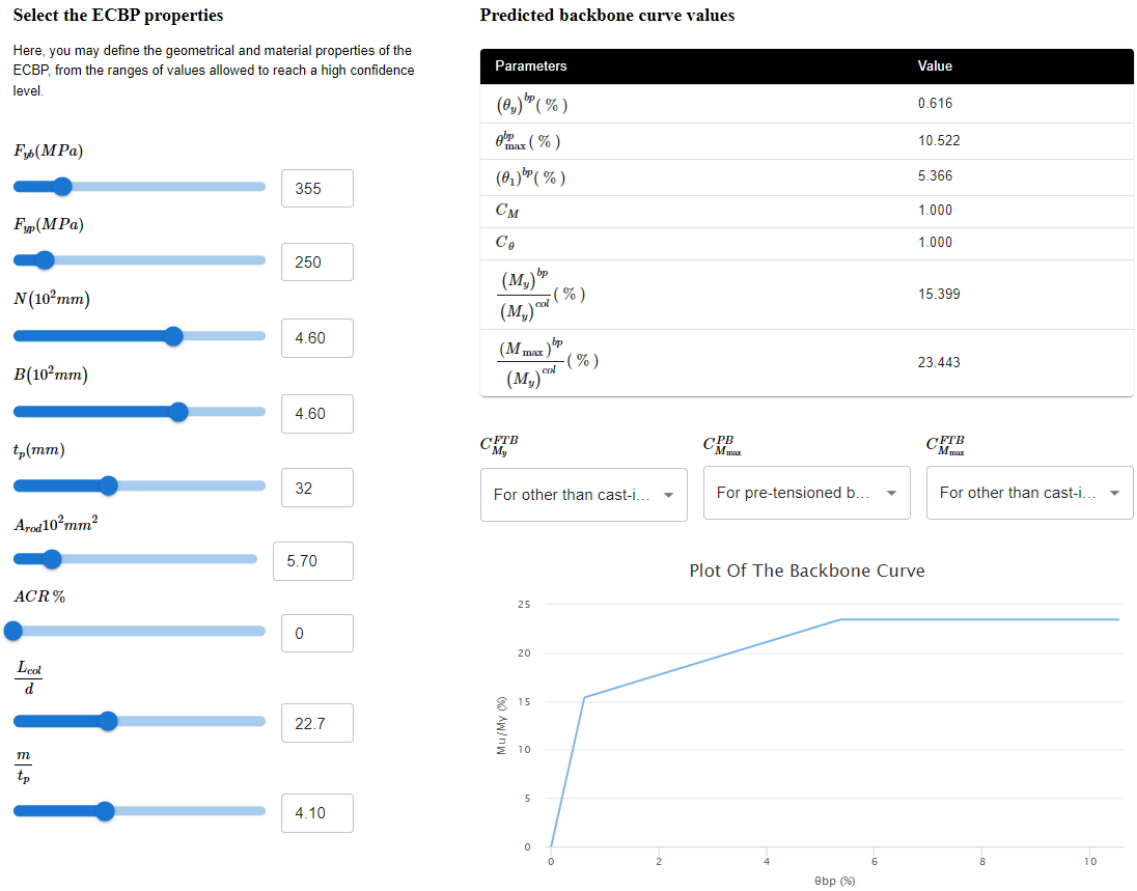

Figure 5-8. Estimation of the modelling parameters for specimen S2S4 (Trautner et al. (2016)) with the web-based tool

5.6.3 ***Cross validation test***

A *k*-fold Cross-Validation (CV) process illustrated in Figure 5-9 was used to evaluate the performance of the proposed equations against out-of-sample predictions. The *k*-fold CV procedure is a well stablished technique to test the predictive performance of regression models for new data (Sun *et al*. (2021), Wakjira *et al*. (2022)). This procedure consisted in randomly splitting the full dataset (or the original training dataset) into testing and training subsets in the proportion near to 20% / 80%, respectively. Then, the training subset was used to train new regression models while the testing one was used to test them. This process was repeated *k* times such that the testing subsets are mutually exclusive and of approximately equal size to previous folds. Finally, since the metric *RMSE* was used to evaluate the performance of the proposed regression models for new data (or out-of-sample data), then the generalized performance of the models for new data is considered as the average of the *RMSE* over the *k* folds. Overall, the out-of-sample performance of a model is as good as the average *RMSE* is smaller; besides, the *RMSE*

of a least-square regression model shall be lower than the generalized performance obtained through CV.

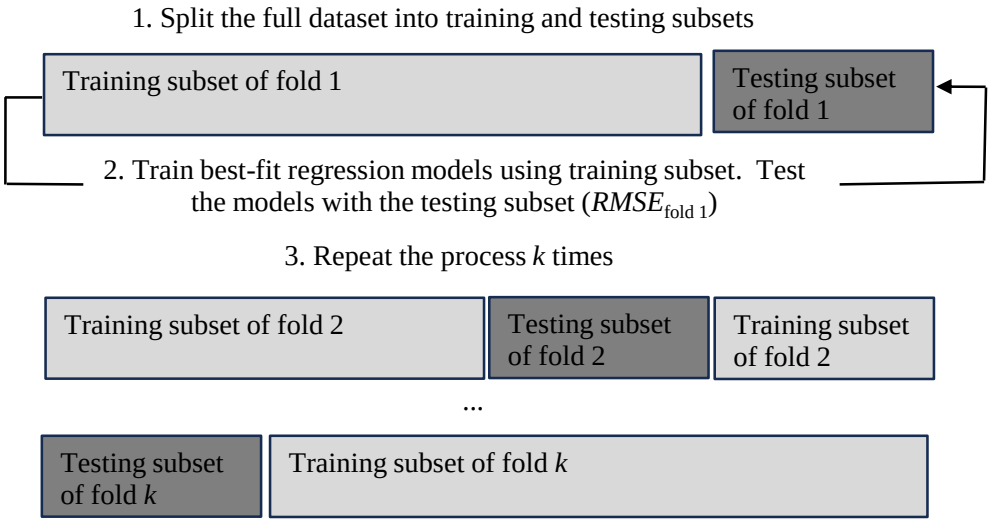

Figure 5-9. Illustration of CV using k folds

Table 5-8 summarizes the results of the CV test performed in this study. It is noticed that all the models for the seven modeling parameters display a satisfactory performance for new data also. For instance, the in-sample *RMSE* for θ_y^{bp} is 0.31 while the out-of-sample $RMSE_{\text{new data}}$ is 0.34; this is, both *RMSE* values are relatively low while the predictive model has a slightly lower value.

Table 5-8. Summary of k-fold cross validation of predictive equations

Description	θ_y^{bp} (%)	θ_{max}^{bp} (%)	θ_1^{bp} (%)	C_M (1)	C_θ (1)	$\frac{M_y^{bp}}{M_y^{col}}$ (%)	$\frac{M_{max}^{bp}}{M_y^{col}}$ (%)
$RMSE_{\text{fold 1}}$	0.28	4.09	0.75	0.11	0.35	15.12	34.54
$RMSE_{\text{fold 2}}$	0.66	5.45	0.80	0.15	0.31	14.03	19.30
$RMSE_{\text{fold 3}}$	0.52	3.64	1.00	0.06	0.21	14.02	25.05
$RMSE_{\text{fold 4}}$	0.30	1.93	1.11	0.14	0.13	16.38	50.60
$RMSE_{\text{fold 5}}$	0.23	2.68	1.20	0.07	0.26	6.51	11.29
$RMSE_{\text{fold 6}}$	0.21	3.11	1.01	0.11	0.18	6.17	17.56
$RMSE_{\text{fold 7}}$	0.33	2.58	1.67	-	-	15.96	40.92
$RMSE_{\text{fold 8}}$	0.18	3.02	1.56	-	-	3.85	6.93
$RMSE_{\text{fold 9}}$	0.37	2.55	-	-	-	22.19	8.47
$RMSE_{\text{fold 10}}$	-	-	-	-	-	-	11.28
$RMSE_{\text{new data}}$	0.34	3.23	1.14	0.11	0.24	12.69	22.59
In-sample *RMSE*	0.31	2.99	1.01	0.09	0.17	10.63	22.04
k	9	9	8	6	6	9	10
Training-testing split	56-7 (9 folds)	49-7 (2 folds) 50-6 (7 folds)	40-6 (6 folds) 41-5 (2 folds)	35-7 (6 folds)	35-7 (6 folds)	56-7 (9 folds)	68-8 (6 folds) 69-7 (4 folds)
n	63	56	46	42	42	63	76

k: number of folds for cross-validation.

The experimental studies on the type of ECBPs in the scope of this research (with bolts located out of the column flanges) only include W10 and HSS300x300 as the deepest sections, mainly because these connections are typically designed with W14 or shallower sections. Nevertheless, the experiments on W14 and W16 steel columns by Cravero *et al*. (2020) (specimens A1, A2, B1, B2, C1 and C1) involved ECBPs which are like the type studied in this research and has been used as additional testing subset to test the predictive performance of the models with deeper columns. The predicted and experimental modeling parameters have been compared and found to be reasonably similar, therefore the proposed models can provide the best estimates until more specific tests are available. This comparison is reflected on Figure 5-4 and Figure 5-6. Based on the results of Elkady and Lignos (2015), the deterioration of deeper columns on ECBP is not recommended to be predicted with these models, thus C_M and C_θ are not predicted with these models. These models can reasonably predict the modeling parameters of deeper columns, except the deterioration parameters; in this regard, refer to Ibarra and Krawinkler (2005) about how these may not be important for overall response

6 SUMMARY, CONCLUSIONS, AND FUTURE INVESTIGATIONS

6.1 Summary

The Thesis focus on the influence of Axial Compression Ratio (*ACR*) in columns on the seismic performance of two building frame systems, namely reinforced-concrete moment-resisting frames and Exposed Column Base Plates (ECBP). For this purpose, the work is split into three parts. Chapter 2 presents a review on the state-of-the-art of the seismic design methodologies and, the strength models for ECBP according to the American and European standards.

- The **first part** (chapter 3) numerically studies the influence of the Axial Compression Ratio (*ACR*) of RC columns of frame buildings on their global structural performance, even accounting for seismic effects. In order to obtain preliminary conclusions, three existing prototype 6 and 11-story buildings are analyzed; they exhibit, only under vertical service loads, excessive Demand Capacity Ratios (*DCR*) in some columns. To improve that situation, three types of alterations have been considered: (i) retrofitting the overloaded columns with steel jacketing, (ii) increasing the concrete strength (f'_c), and (iii) reducing the number of stories *N*s. Code-type and pushover analyses are performed on the original and retrofitted buildings with steel jacketing; the suitability of the modified buildings (higher concrete strength and less *N*s) is checked by code-type analyses only.
- In the **second part** (section 4), the design philosophies adopted by the American Institute of Steel Construction and Eurocode 3, are adapted to develop a M-P interaction diagrams approach for the analysis and design of exposed column base plates; the diagrams are associated with the failure of the components against uniaxial bending along the section strong-direction. Three code-complying specimens are designed to be representative of low-rise steel moment-resisting-frame buildings. The aims of this work are to: i) simulate the expected failure modes and stress distributions of the specimens, through the finite element method, ii) apply the M-P interaction diagrams approach to the specimens, iii) compare the finite element analysis results with the M-P interaction diagrams predictions, iv) parametrically analyze the variability of the thickness of plate according to the classical design approach. The results of this study are discussed in terms of i) the influence of the M-P interaction on the flexural strength of the components of the connections, ii) the failure modes of the specimens.
- The **third part** (chapter 5) is focused on the characterization of the modelling parameters of ECBP subjected to combined uniaxial flexure and compression loads, and their dependence on the main design variables for these connections. A dataset of 84 experimental test-results was developed and made available at https://cbp-db-modelling.utb.edu.co/search. A trilinear fashion was adopted to represent the M-θ curves of the ECBP, given its feasibility to represent both the stiffness and strength deterioration of structural components. The selection of predictor variables was attempted in three steps; firstly, potential predictor variables from published mechanics-based models and test parameters, were preliminary selected; secondly, the number of predictor variables was filtered considering experimental observations, and their statistical significance; Thirdly, final predictor variables for each modelling parameter were defined through a

backward regression analysis. Best-fit predictive equations for the trilinear model adopted were set and then, their modelling parameters were evaluated for each specimen in the database.

6.2 Conclusions

The overall conclusion of the **first part** of this thesis (section 3) is that *ACR* is a sufficiently reliable index of the final strength of the structure (quantified in terms of *DCR*); therefore, the limitation of *ACR* in the design codes might save money, time and effort. The main particular conclusions of this section are listed next.

- The columns of the original buildings with *ACR* of 20, 30 and 40% or greater, exhibit *DCR* larger than 1, even for a low seismic demand. For the analyzed situations, the European regulations (EN-1998, 2004) limit *ACR* to 43%; this fits the outputs of this study. Conversely, the American documents do not include any such prescription.
- Comparison between the original and retrofitted buildings shows that the retrofit increases the axial capacity of the columns by percentages ranging between 98 and 187%; larger increments are obtained for bending. These gains eliminate over stress.
- Comparison between the original and modified buildings shows that the increment of f´c from 21 to 35 MPa causes a reduction in ACR ranging between 40 and 55%. Nonetheless, neither DCR nor the story drift gets substantially reduced because f´c has no significant influence on the column's flexural capacity. The removal of each story causes reductions of ACR ranging between 9 and 18%; thereby, the maximum Ns for these buildings to meet the limit for ACR (in the Eurocode) and the seismic capacity (in the Colombian code) are, three instead of six, and seven or five instead of eleven.
- Comparison between the original, retrofitted, and modified buildings shows that columns ACR is directly related to the building's seismic performance (in terms of strength and drift).

The general conclusion of the **second part** of this thesis (section 4) is that the proposed uniaxial M-P interaction diagrams approach can reliably predict the failure modes of exposed column base plates along their major column-axis and, the reduced flexural strength of the main components of these connections due to M-P loads. The main individual conclusions of this section are listed below:

- For high eccentricity loads, the M-P interaction diagrams for the American philosophy are substantially adjusted to the finite-element-analysis results; conversely, the diagrams for the European philosophy do not show a good fit to the finite-element-analysis. For the case of pure bending, the predicted normalized-flexural-strength of the three analyzed specimens are: i) 9% (finite-element-analysis), 9% (American) and 43% (Eurocode); ii) 5% (finite-element-analysis), 5% (American) and 42% (European); iii) 16% (finite-element-analysis), 9% (American) and 58% (European).
- For low eccentricity loads, the M-P interaction diagrams for the American and European philosophies are reasonably adjusted to the finite-element-analysis results; both design philosophies conduct to properly conservative predictions. Nonetheless, the diagrams for the Eurocode are slightly closer to the simulated results than the diagrams for the American standards. For the case of pure axial loads, the predicted normalized-axial-capacity of the analyzed specimens are: i) 62% (finite-element-analysis), 24% (American) and 33% (European); ii) 41% (finite-element-analysis), 24% (American) and 33% (European); iii) 56% (finite-element-analysis), 36% (American) and 40% (European).
- For a common ACR of 30%, the design philosophy adopted by the European codes leads to plates 48 and 54% thinner than the American standards, for zero and small eccentricity conditions respectively. However, these standards produce plates 34% thinner than the European code for high eccentricity loads.

The main conclusions of **part three** (section 5) of this research are:

- When the proposed predictive equations for the rotational parameters are used, the yielding, intermediate (that associated with the start of the plastic plateau) and ultimate rotations can be individually predicted with satisfactory correlation coefficients. On the analysis of the equations for the rotational parameters, the length and thickness of plate notably influence on all the modelling parameters, while the design variables of the bolts (i.e., cross-sectional area of bolts in the tensile side, and their yielding stress) particularly influence on the ultimate rotation. These analyses agree with experimental observations.
- The predicted and measured post-peak degradation parameters of ECBPs indicate a small degradation, and large ductility capacity of these connections. Overall, the properties and dimensions of the steel plate are the most influential variables on these parameters. On the other side, the determination coefficients for post-peak degradation parameters are relatively low, when compared with those of other modelling parameters. It is recommended to extend the dataset for cyclic tests, including different width-thickness ratios for the column web and flange, to study their influence on the post-peak degradation parameters.
- On average, the predicted yielding and ultimate strength parameters of ECBP are 37 % and 61 % (normalized to the yielding strength of the column), respectively. These parameters are predicted with high correlation coefficients. Overall, the length and thickness of plate considerably influence the strength parameters, and the cross-sectional area of the rods in the tensile side, especially influences on the ultimate strength, which match experimental findings of compiled publications.
- The regression-equations proposed in this work can accurately predict the modeling parameters required to build the full-range M-θ curves of ECBP, following a trilinear model. The average determination coefficient between the predicted and the experimental full-range curves is 0.91.
- The median values of the experimental and predicted yielding-rotations are both equal to 0.7 % Therefore, ECBPs in MRF-buildings are expected to deform inelastically even under inter-story-drifts lower than 1%.
- The multivariable regression analysis performed in this study shows that the axial loads have a paramount role in the prediction of the strength and deformation parameters of ECBP, and therefore on their seismic performance.

6.3 Future Investigations

From the obtained results, the following further researches are envisaged:

For the **second part**:

- The generation of additional M-P interaction diagrams of more specimens, varying the design variables of Exposed Column Base Plates. Besides, additional experimental tests are recommended to be conducted in order to generalize the remarks for code-based purposes.

For the **third part**:

The expansion of the experimental database. Being regression based, the models are limited by the range of experimental data – and extrapolation may result in loss of accuracy. In addition, as the most of the specimens in the set of data are code-designed ones, the regression equations proposed are mainly applicable to configurations of ECBP which follow code specifications (e.g., DG1 (Fisher & Kloiber, 2006) and EC 3:1-8 (CEN, 2005b)). Most of the specimens utilize light to medium sections (e.g., with section depth equal or smaller than 250 mm), thus the use of the models proposed in this work provides better confidence level with these sections. Also, the *ACR*s employed for most of the experimental champaigns are between 0 % and 25%, therefore the axial

load within this range could provide a higher confidence level.

Despite these limitations, it is hoped that the methods presented herein will facilitate improved simulation of base connections in building models, given the lack of such models in the literature.

REFERENCES

Abdelkerim, D., Wang, X., Ibrahim, H. A., & Wu, Z. (2019). Static and fatigue behavior of pultruded FRP multi-bolted joints with basalt FRP and hybrid steel-FRP bolts. *Composite Structures*, *220*. https://doi.org/10.1016/j.compstruct.2019.03.085

Abdollahzadeh, G., & Ghobadi, M. (2014). Mathematical modeling of column-base connections under monotonic loading. *Civil Engineering Infrastructures Journal*, *47*(2), 255–272. https://doi.org/10.7508/ceij.2014.02.008

Abou-Elfath, H., Ramadan, M., & Omar Alkanai, F. (2017). Upgrading the seismic capacity of existing RC buildings using buckling restrained braces. *Alexandria Engineering Journal*, *56*(2), 251–262. https://doi.org/10.1016/j.aej.2016.11.018

Aboutaha, R. S., Engelhardt, M., Jirsa, J. O., & Kreger, M. E. (1999). *Rehabilitation of shear critical concrete columns by use of rectangular steel jackets* (Vol. 96).

ACI 318. (2014). *Building Code Requirements for Structural Concrete and Commentary*.

Acun, B., & Sucuoğlu, H. (2010). The effect of displacement history on the performance of concrete columns in flexure. In M. N. Fardis (Ed.), *Advances in Performance-Based Earthquake Engineering* (pp. 373–382). Springer Netherlands. https://doi.org/10.1007/978-90-481-8746-1_35

AIS. (2010). NSR-10. Reglamento Colombiano de Construcción Sismo Resistente. *Bogotá, DC*.

AISC 341. (2022). *Seismic provisions for structural steel buildings*. ANSI/AISC. https://www.aisc.org/globalassets/aisc/publications/standards/seismic-provisions-for-structural-steel-buildings-ansi-aisc-341-16.pdf

AISC 360. (2016). *Specification for structural steel buildings*. https://www.aisc.org/Specification-for-Structural-Steel-Buildings-ANSIAISC-360-16-1#.XGXrjlxKjIU

Aladsani, M., Burton, H. V., Abdullah, S., & Wallace, J. (2022). Explainable Machine Learning Model for Predicting Drift Capacity of Reinforced Concrete Walls. *ACI Structural Journal*, *119*(3). https://doi.org/10.14359/51734484

Alfarah, B., López-Almansa, F., & Oller, S. (2020). Numerical Study on the Relevance of Columns Hidden Failure Modes in the Seismic Capacity of Non-Ductile RC Frames. *Journal of Earthquake Engineering*, *24*(9), 1417–1434. https://doi.org/10.1080/13632469.2018.1458666

Al-Mahaidi, R., & Kalfat, R. (2018). Chapter 5—Strengthening members in flexure using FRP. In R. Al-Mahaidi & R. Kalfat (Eds.), *Rehabilitation of Concrete Structures with Fiber-Reinforced Polymer* (pp. 25–119). Butterworth-Heinemann. https://doi.org/10.1016/B978-0-12-811510-7.00005-7

Al-Osta, M. A., Khan, U., Baluch, M. H., & Rahman, M. K. (2018). Effects of variation of axial load on seismic performance of shear deficient RC exterior BCJs. *International Journal of Concrete Structures and Materials*, *12*(1), 46. https://doi.org/10.1186/s40069-018-0277-0

Ansys, Inc. (2018). *ANSYS Release 19.0 Elements Reference*. ANSYS, Inc.

ASCE 7-16. (2017). *Minimum design loads for buildings and other structures* (2016th ed.). American Society of Civil Engineers.

ASCE/SEI 41-17. (2017). *Seismic evaluation and retrofit of existing buildings*. https://doi.org/10.1061/9780784414859

Asif Bin Kabir, Md., Sajid Hasan, A., & Muntasir Billah, A. (2021). Failure mode identification of column base plate connection using data-driven machine learning techniques. *Engineering Structures*, *240*, 112389. https://doi.org/10.1016/j.engstruct.2021.112389

ATC 40, A. (1996). ATC-40: Seismic evaluation and retrofit of concrete buildings. *Applied Technology Council, Report ATC-40. Redwood City*.

Aviram, A., Stojadinovic, B., & Der Kiureghian, A. (2010). *Performance and Reliability of Exposed Column Base Plate Connections for Steel Moment-Resisting Frames* (Technical Report PEER Report 2010/107; p. 190). Pacific Earthquake Engineering Research Center, University of California.

Azarm, R., Maheri, M. R., & Torabi, A. (2017). Retrofitting RC joints using flange-bonded FRP sheets. *Iranian Journal of Science and Technology, Transactions of Civil Engineering*, *41*(1), 27–35. https://doi.org/10.1007/s40996-016-0028-x

Benmokrane, B., Zhang, B., & Chennouf, A. (2000). Tensile properties and pullout behaviour of AFRP and CFRP rods for grouted anchor applications. *Construction and Building Materials*, *14*(3), 157–170. https://doi.org/10.1016/S0950-0618(00)00017-9

Bertero, R., Bertero, V., & Teran-Gilmore, A. (1996). Performance-based earthquake resistant design based on comprehensive design philosophy and energy concepts. *Proceedings of the Eleventh World Conference on Earthquake Engineering*. 611. https://www.iitk.ac.in/nicee/wcee/article/11_611.PDF

Birzhandi, M. S., & Mirzakhani, D. (2023). Modified Modal Pushover Design for Asymmetric-Plan RC Shear-Wall Structures. *Advances in Civil Engineering*, *2023*, 1–36. https://doi.org/10.1155/2023/5627191

Bracci, J. M., Kunnath, S. K., & Reinhorn, A. M. (1997). Seismic Performance and Retrofit Evaluation of Reinforced Concrete Structures. *Journal of Structural Engineering*, *123*(1), 3–10. https://doi.org/10.1061/(ASCE)0733-9445(1997)123:1(3)

Buildings Department (HKBD). (2013). *Code of practice for structural use of concrete 2013*. The HKSAR Goverment.

Burda, J. J., & Itani, A. (1999). *Studies of seismic behavior of steel base plates. CCEER 99-7* (Technical Report CCEER 99-7; p. 298). Center for Civil Engineering Earthquake Research (CEER).

Carrillo, J., & González, G. (2007). Inelastic modeling of concrete frames with nonreinforced masonry. *DYNA*, *74*(152), 229–239.

CEN. (2005a). *Eurocode 3: Design of steel structures—Part 1-1: General rules and rules for buildings (EN 1993-1-1 :2005)* (Standard EN 1993-1-1; p. 227).

CEN. (2005b). *Eurocode 3: Design of steel structures—Part 1-8: Design of joints (EN 1993-1-8 :2005)* (Standard EN 1993-1-8; p. 135).

Chatterjee, S., & Hadi, A. S. (2015). *Regression analysis by example*. Wiley. https://public.ebookcentral.proquest.com/choice/publicfullrecord.aspx?p=918623&entityid=urn:mace:eduserv.org.uk:athens:provider:liv.ac.uk

Chen, T., Xia, Z., Wang, X., Zhao, Q., Yuan, G., & Liu, J. (2018). Experimental study on grouted connections under static lateral loading with various axial load ratios. *Engineering Structures*, *176*, 801–811. https://doi.org/10.1016/j.engstruct.2018.09.056

Chen, Z. Y., Chen, W., Zhang, W., & Lou, M. L. (2016). Effects of axial compression ratio of central columns on seismic performance of a multi-story underground structure. *International Journal of Computational Methods*, *13*(04), 1641014. https://doi.org/10.1142/S0219876216410140

Chi, H., & Liu, J. (2012). Seismic behavior of post-tensioned column base for steel self-centering moment resisting frame. *Journal of Constructional Steel Research*, *78*, 117–130. https://doi.org/10.1016/j.jcsr.2012.07.005

China Architecture & Building Press. (2010). *National Standard of the People´s Republic of China. Code for seismic design of buildings (GB 50011-2010)*. Beijing.

Choi, J.-H., & Choi, Y. (2013). An experimental study on inelastic behavior for exposed-type steel column bases under three-dimensional loadings. *Journal of Mechanical Science and Technology*, *27*(3), 747–759. https://doi.org/10.1007/s12206-012-0901-x

Chopra, A. K. (2007). *Dynamics of Structures: Theory and Application in Earthquake Engineering* (Vol. 11).

Chopra, A. K., & Goel, R. K. (2002). A modal pushover analysis procedure for estimating seismic demands for buildings. *Earthquake Engineering & Structural Dynamics*, *31*(3), 561–582. https://doi.org/10.1002/eqe.144

Cimellaro G. P., Giovine T., & Lopez-Garcia D. (2014). Bidirectional pushover analysis of irregular structures. *Journal of Structural Engineering*, *140*(9), 04014059. https://doi.org/10.1061/(ASCE)ST.1943-541X.0001032

Clough, R. W., & Penzien, J. (1993). *Dynamics of Structures*. McGraw-Hill.

Computer and Structures Inc. (2016). *Concrete Frame Design Manual ACI 318-11 for SAP 2000*. Computers & Structures, Inc. http://docs.csiamerica.com/manuals/sap2000/Design/CFD-ACI-318-11.pdf

Computer and Structures Inc. (2017). *Steel frame design manual AISC 360-16 for SAP 2000*.

Cravero, J., Elkady, A., & Lignos, D. G. (2020). Experimental Evaluation and Numerical Modeling of Wide-Flange Steel Columns Subjected to Constant and Variable Axial Load Coupled with Lateral Drift Demands. *Journal of Structural Engineering*, *146*(3), 04019222. https://doi.org/10.1061/(ASCE)ST.1943-541X.0002499

Cui, Y., Nagae, T., & Nakashima, M. (2009). Hysteretic behavior and strength capacity of shallowly embedded steel column bases. *Journal of Structural Engineering*, *135*(10), 1231–1238. https://doi.org/10.1061/(ASCE)ST.1943-541X.0000056

Della Corte, G., & Landolfo, R. (2017). Lateral loading tests of built-up battened columns with semi-continuous base-plate connections. *Journal of Constructional Steel Research*, *138*, 783–798. https://doi.org/10.1016/j.jcsr.2017.08.018

Demir, S., Husem, M., & Pul, S. (2014). Failure analysis of steel column-RC base connections under lateral cyclic loading. *Structural Engineering and Mechanics*, *50*(4), Article 4. http://dx.doi.org/10.12989/sem.2014.50.4.459

DeWolf, J. T., & Sarisley, E. F. (1980). Column base plates with axial loads and moments. *Journal of the Structural Division*, *106*(11), 2167–2184. https://doi.org/10.1061/JSDEAG.0005569

Di Sarno, L., Pecce, M. R., & Fabbrocino, G. (2007). Inelastic response of composite steel and concrete base column connections. *Journal of Constructional Steel Research*, *63*(6), 819–832. https://doi.org/10.1016/j.jcsr.2006.08.007

Díaz, H., Nuñez, E., & Oyarzo-Vera, C. (2020). Monotonic response of exposed base plates of columns: Numerical study and a new design method. *Metals*, *220*(3), 396. https://doi.org/10.3390/met10030396

Domínguez, D., López-Almansa, F., & Benavent-Climent, A. (2016). Would RC wide-beam buildings in Spain have survived Lorca earthquake (11-05-2011)? *Engineering Structures*, *108*, 134–154. https://doi.org/10.1016/j.engstruct.2015.11.020

Drake, R. M., & Elkin, S. J. (1999). Beam-column base plate design-LRFD Method. *Engineering Journal*, *36*(Quarter 1), 16–38.

Dumas, M., Beaulieu, D., & Picard, A. (2006). Characterization equations for steel column base connections. *Canadian Journal of Civil Engineering*, *33*(4), 409–420. https://doi.org/10.1139/l05-054

Elkady, A., & Lignos, D. G. (2015). Analytical investigation of the cyclic behavior and plastic hinge formation in deep wide-flange steel beam-columns. *Bulletin of Earthquake Engineering*, *13*(4), 1097–1118. https://doi.org/10.1007/s10518-014-9640-y

Elwood, K. J., & Moehle, J. P. (2008). Dynamic collapse analysis for a reinforced concrete frame sustaining shear and axial failures. *Earthquake Engineering & Structural Dynamics*, *37*(7), 991–1012. https://doi.org/10.1002/eqe.787

EN-1998. (2004). *Eurocode 8: Design of structures for earthquake rsistance-Part 1: General rules, seismic actions and rules for buildings (EN-1998-1)*. European Comitee for Standarization.

Ermopoulos, J. C., & Michaltsos, G. T. (1998). Analytical modelling of stress distribution under column base plates. *Second World Conference on Steel in Construction*, *46*(1), 246. https://doi.org/10.1016/S0143-974X(98)80026-6

Ermopoulos, J. Ch., & Stamatopoulos, G. N. (1996). Mathematical modelling of column base plate connections. *Journal of Constructional Steel Research*, *36*(2), 79–100. https://doi.org/10.1016/0143-974X(95)00011-J

Eröz Murat, White Donald W., & DesRoches Reginald. (2008). Direct analysis and design of steel frames accounting for partially restrained column base conditions. *Journal of Structural Engineering*, *134*(9), 1508–1517. https://doi.org/10.1061/(ASCE)0733-9445(2008)134:9(1508)

Fahmy, M., Stojadinovic, B., & Goel, S. C. (1999). *Analytical and experimental studies on the seismic response of steel column bases*. 245–250.

Fajfar, P., & Fischinger, M. (1988). N2-A method for non-linear seismic analysis of regular buildings. *Proceedings of Nine World Conference on Earthquake Engineering*, *V*.

Falborski, T., Hassan, A. S., & Kanvinde, A. M. (2020). Column base fixity in steel moment frames: Observations from instrumented buildings. *Journal of Constructional Steel Research*, *168*, 105993. https://doi.org/10.1016/j.jcsr.2020.105993

Falcone, R., Carrabs, F., Cerulli, R., Lima, C., & Martinelli, E. (2019). Seismic retrofitting of existing RC buildings: A rational selection procedure based on Genetic Algorithms. *Structures*, *22*, 310–326. https://doi.org/10.1016/j.istruc.2019.08.006

Fasaee, M. A. K., Banan, M. R., & Ghazizadeh, S. (2018). Capacity of exposed column base connections subjected to uniaxial and biaxial bending moments. *Journal of Constructional Steel Research*, *148*, 361–370. https://doi.org/10.1016/j.jcsr.2018.05.025

FEMA 349. (2000). *Action Plan for Performance Based Seismic Design*. FEMA.

FEMA 350. (2013). *Recommended Seismic Design Criteria for New Steel Moment-frame Buildings*. FEMA.

FEMA 356. (2000). *Prestandard and commentary for the seismic rehabilitation of buildings*. FEMA.

FEMA 389. (2004). *Primer for design professionals: Comunicating with owners and managers of new buildings on earthquake risk*.

FEMA 440 (ATC-55). (2005). *Improvement of nonlinear static seismic analysis procedures*. FEMA.

FEMA P58. (2018). *Development of Next Generation Performance-Based Seismic Design Procedures for New and Existing Buildings*. FEMA.

Fisher, J. M., & Kloiber, L. A. (2006). *Design guide 1: Base plate and anchor rod design (second edition)*. https://www.aisc.org/Design-Guide-1-Base-Plate-and-Anchor-Rod-Design-Second-Edition-Print#.XVfizOhKhPY

Freddi, F., Dimopoulos, C. A., & Karavasilis, T. L. (2017). Rocking damage-free steel column base with friction devices: Design procedure and numerical evaluation. *Earthquake Engineering & Structural Dynamics*, *46*(14), 2281–2300. https://doi.org/10.1002/eqe.2904

García Reyes, L. E. (1998). *Dinámica estructural aplicada al diseño sísmico* (First). Universidad de los Andes.

Goel, R. K., & Chopra, A. K. (2005). Modal Pushover Analysis for Unsymmetric Buildings. *Structures Congress 2005*, 1–9. https://doi.org/10.1061/40753(171)185

Gomez, I., & Kanvinde, A. M. (2009). *Shear transfer in exposed column base plates* (Technical Report NSF-CMMI 0421492 Phase 1). American Institute of Steel Construction, AISC.

Gomez, I., Kanvinde, A., & Smith, C. (2010). *Exposed column base connections subjected to axial compression and flexure* (Technical Report NSF-CMMI 0421492 Phase 2). American Institute of Steel Construction, AISC.

González Cuevas, O. M., Guerrero Correa, J. J., Gómez González, B., & Flores Díaz, F. A. (2007). Resistencia a fuerza cortante de columnas de concreto reforzadas con camisas de acero. *Revista de Ingeniería Sísmica*, *77*, 53–70. https://doi.org/10.18867/ris.77.95

Grauvilardell, J. E., Lee, D., Hajjar, J. F., & Dexter, R. J. (2005). *Synthesis of design, testing and analysis research on steel column base plate connections in high-seismic zones*. 181.

Grilli, D. A., & Kanvinde, A. (2015). *Embedded column base connections subjected to flexure and axial load: Test and strength models* (Final Report 3–11; p. 83). Charles Pankow Foundation, American Institute of steel Construction and California University. https://www.aisc.org/globalassets/aisc/research-library/embedded-column-base-connections-grilli-and-kanvinde.pdf

Grilli, D., Jones, R., & Kanvinde, A. (2017). Seismic performance of embedded column base connections subjected to axial and lateral loads. *Journal of Structural Engineering*, *143*(5), 04017010. https://doi.org/10.1061/(ASCE)ST.1943-541X.0001741

Gupta, B., & Kunnath, S. K. (2000). Adaptive Spectra-Based Pushover Procedure for Seismic Evaluation of Structures. *Earthquake Spectra*, *16*(2), 367–391. https://doi.org/10.1193/1.1586117

Gutiérrez-Urzúa, F., Freddi, F., & Di Sarno, L. (2021). Comparative analysis of code-based approaches for seismic assessment of existing steel moment resisting frames. *Journal of Constructional Steel Research*, *181*, 106589. https://doi.org/10.1016/j.jcsr.2021.106589

Guyader, A. C., & Iwan, W. D. (2006). Determining Equivalent Linear Parameters for Use in a Capacity Spectrum Method of Analysis. *Journal of Structural Engineering*, *132*(1), 59–67. https://doi.org/10.1061/(ASCE)0733-9445(2006)132:1(59)

Han, S. W., & Chopra, A. K. (2006). Approximate incremental dynamic analysis using the modal pushover analysis procedure. *Earthquake Engineering & Structural Dynamics*, *35*(15), 1853–1873. https://doi.org/10.1002/eqe.605

Hasegawa, T. (2013). *History of Structural Standards for Buildings in Japan*, *Japan Building Center*. https://www.bcj.or.jp/upload/international/baseline/BSLIntroduction201307_e.pdf

Hassan, A. S., Song, B., Galasso, C., & Kanvinde, A. (2022). Seismic Performance of Exposed Column–Base Plate Connections with Ductile Anchor Rods. *Journal of Structural Engineering*, *148*(5), 04022028. https://doi.org/10.1061/(ASCE)ST.1943-541X.0003298

Hon, K. K., & Melchers, R. E. (1988). Experimental behaviour of steel column bases. *Journal of Constructional Steel Research*, *9*(1), 35–50. https://doi.org/10.1016/0143-974X(88)90055-7

Housner, G. W. (1990). Historical Review of Earthquake Engineering. In *Selected Earthquake Engineering Papers of George W. Housner* (pp. 764–777). American Society of Civil Engineers.

Huang, Z., Liu, H., Li, Z., & Zhang, G. (2019). Plastic limit analysis for eight-bolted base plate based on slip-line field theory. *Journal of Constructional Steel Research*, *162*, 105739. https://doi.org/10.1016/j.jcsr.2019.105739

Ibarra, L. F., & Krawinkler, H. (2005). *Global collapse of frame structures under seismic excitations. Report N° 152*. Standford University.

IBC. (2000). *International Building Code*®. ICC (International Code Council).

Islam, N., & Hoque, M. M. (2015). Strengthening of Reinforced Concrete Columns by Steel Jacketing: A State of Review. *Asian Transactions on Engineering (ATE)*, *05*.

JASP Team. (2023). *JASP (Version 0.17.1) [Computer software]* [Computer software].

Jaspart, J. P., & Vandegans, D. (1998). Application of the component method to column bases. *Journal of Constructional Steel Research*, *48*(2), 89–106. https://doi.org/10.1016/S0143-974X(98)90196-1

Jaspart, J. P., Wald, F., Weynand, K., & Gresnigt, A. M. (2008). Component method for steel column bases. *HERON*, *53*(1/2), 3–20.

Kamperidis, V. C., Karavasilis, T. L., & Vasdravellis, G. (2018). Self-centering steel column base with metallic energy dissipation devices. *Journal of Constructional Steel Research*, *149*, 14–30. https://doi.org/10.1016/j.jcsr.2018.06.027

Kanvinde, A., Grilli, D., & Zareian, F. (2012). Rotational stiffness of exposed column base connections: Experiments and analytical models. *Journal of Structural Engineering*, *138*(5), 549–560. https://doi.org/10.1061/(ASCE)ST.1943-541X.0000495

Kanvinde, A. M., Higgins, P., Cooke, R. J., Perez, J., & Higgins, J. (2015). Column base connections for hollow steel sections: Seismic performance and strength models. *Journal of Structural Engineering*, *141*(7), 04014171. https://doi.org/10.1061/(ASCE)ST.1943-541X.0001136

Kanvinde, A. M., Jordan, S. J., & Cooke, R. J. (2013). Exposed column base plate connections in moment frames—Simulations and behavioral insights. *Journal of Constructional Steel Research*, *84*, 82–93. https://doi.org/10.1016/j.jcsr.2013.02.015

Kavoura, F., Gencturk, B., & Dawood, M. (2017). Reversed cyclic behavior of column-to-foundation connections in low-rise metal buildings. *Journal of Structural Engineering*, *143*(9), 04017095. https://doi.org/10.1061/(ASCE)ST.1943-541X.0001821

Kavoura, F., Gencturk, B., & Dawood, M. (2018a). Evaluation of existing provisions for design of "pinned" column base-plate connections. *Journal of Constructional Steel Research*, *148*, 233–250. https://doi.org/10.1016/j.jcsr.2018.05.030

Kavoura, F., Gencturk, B., & Dawood, M. (2018b). *Evaluation of existing provisions for design of "pinned" column base-plate connections* (Vol. 148). https://doi.org/10.1016/j.jcsr.2018.05.030

Kavoura, F., Gencturk, B., Dawood, M., & Gurbuz, M. (2015). Influence of base-plate connection stiffness on the design of low-rise metal buildings. *Journal of Constructional Steel Research*, *115*, 169–178. https://doi.org/10.1016/j.jcsr.2015.08.005

Kayani, A. W., & W. Tabsh, S. (2012). Experimental and Computational Studies on Steel Base Plates on Leveling Nuts. *Research, Development and Practice in Structural Engineering and Construction*, 335–339. https://doi.org/10.3850/978-981-08-7920-4_St-129-0399

Kharazian, A. (2017). *Analysis of seismic pounding of moderate-height RC buildings with aligned slabs* [Doctoral Thesis]. Universitat Politècnica de Catalunya.

Khodaie, S., Mohamadi-shooreh, M. R., & Mofid, M. (2012). Parametric analyses on the initial stiffness of the SHS column base plate connections using FEM. *Engineering Structures*, *34*, 363–370. https://doi.org/10.1016/j.engstruct.2011.09.026

Kircher, C. A., Nassar, A. A., Kustu, O., & Holmes, W. T. (1997). Development of Building Damage Functions for Earthquake Loss Estimation. *Earthquake Spectra*, *13*(4), 663–682. https://doi.org/10.1193/1.1585974

Krawinkler, H., & Seneviratna, G. D. P. K. (1998). Pros and cons of a pushover analysis of seismic performance evaluation. *Engineering Structures*, *20*(4–6), 452–464. https://doi.org/10.1016/S0141-0296(97)00092-8

Latour, M., Piluso, V., & Rizzano, G. (2014). Rotational behaviour of column base plate connections: Experimental analysis and modelling. *Engineering Structures*, *68*, 14–23. https://doi.org/10.1016/j.engstruct.2014.02.037

Latour, M., & Rizzano, G. (2013). A theoretical model for predicting the rotational capacity of steel base joints. *Journal of Constructional Steel Research*, *91*, 89–99. https://doi.org/10.1016/j.jcsr.2013.08.009

Latour, M., & Rizzano, G. (2019). Mechanical modelling of exposed column base plate joints under cyclic loads. *Journal of Constructional Steel Research*, *162*, 105726. https://doi.org/10.1016/j.jcsr.2019.105726

Latour, M., Rizzano, G., Santiago, A., & Simões da Silva, L. (2019). Experimental response of a low-yielding, self-centering, rocking column base joint with friction dampers. *Soil Dynamics and Earthquake Engineering*, *116*, 580–592. https://doi.org/10.1016/j.soildyn.2018.10.011

Lee, D. Y., Subhash, C. G., & Bozidar, S. (2008). Exposed column-base plate connections bending about weak axis. *International Journal of Steel Structures*, *8*, 29–41.

Lee, D.-Y., Goel, S. C., & Stojadinovic, B. (2008). Exposed column-base plate connections bending about weak axis: I numerical parametric study. *International Journal of Steel Structures*, *8*, 1–27.

Li, Y. J., & Liu, P. (2012). Effect of axial compression ratio on ductility and bearing capacity of specially shaped columns with HRB500 reinforcement. *Applied Mechanics and Materials*, *204–208*, 1066–1069. https://doi.org/10.4028/www.scientific.net/AMM.204-208.1066

Li, Y., & Yang, B. (n.d.). Discussion on limit values of axial compression ratio of steel reinforced concrete columns. In *Civil Engineering and Urban Planning 2012* (pp. 209–213). https://doi.org/10.1061/9780784412435.037

Lignos, D. G., & Hartloper, A. R. (2020). Steel column stability and implications in the seismic assessment of steel structures according to Eurocode 8 Part 3. *Stahlbau*, *89*(1), 16–27. https://doi.org/10.1002/stab.201900108

Lignos, D. G., & Krawinkler, H. (2011). Deterioration modeling of steel components in support of collapse prediction of steel moment frames under earthquake loading. *Journal of Structural Engineering*, *137*(11), 1291–1302. https://doi.org/10.1061/(ASCE)ST.1943-541X.0000376

Lim, W.-Y., Lee, D., & You, Y.-C. (2017). Cyclic loading tests on exposed column-base plate weak-axis connections of small-size steel structures. *Engineering Structures*, *153*, 653–664. https://doi.org/10.1016/j.engstruct.2017.10.066

López-Almansa, F., Domínguez, D., & Benavent-Climent, A. (2013). Vulnerability analysis of RC buildings with wide beams located in moderate seismicity regions. *Engineering Structures*, *46*, 687–702. https://doi.org/10.1016/j.engstruct.2012.08.033

Mander, J., Priestley, M., & Park. (1988). Theoretical stress–strain model for confined concrete. *American Society of Civil Engineers*, *114*(8), 1804–1826.

Mao, J., Zhai, C., & Xie, L. (2008). An improved modal pushover analysis procedure for estimating seismic demands of structures. *Earthquake Engineering and Engineering Vibration*, *7*(1), 25–31. https://doi.org/10.1007/s11803-008-0786-y

Martínez-Rueda, J. E., & Elnashai, A. S. (1997). Confined concrete model under cyclic load. *Materials and Structures*, *30*(3), 139–147. https://doi.org/10.1007/BF02486385

Melchers, R. E. (1992). Column-base response under applied moment. *Journal of Constructional Steel Research*, *23*(1–3), 127–143. https://doi.org/10.1016/0143-974X(92)90040-L

Miano, A., Chiumiento, G., Formisano, A., & Prota, A. (2022). How does the knowledge level affect the seismic retrofit cost? The case study of a RC building. *Structural Engineering and Mechanics*, *82*(5), 557–569. https://doi.org/10.12989/SEM.2022.82.5.557

Mohabeddine, A., Koudri, Y. W., Correia, J. A. F. O., & Castro, J. M. (2021). Rotation capacity of steel members for the seismic assessment of steel buildings. *Engineering Structures*, *244*, 112760. https://doi.org/10.1016/j.engstruct.2021.112760

Nateghi-A, F. (1995). Seismic strengthening of eightstorey RC apartment building using steel braces. *Engineering Structures*, *17*(6), 455–461. https://doi.org/10.1016/0141-0296(95)00071-E

NCSE-02. (2002). *Norma de Construcción Sismorresistente: Parte General y Edificación*. Ministerio de Fomento.

Ohashi, U. (1993). *History of Structural Standards for Buildings in Japan*. Japan Building Centre (in Japanese).

Pampanin, S., & Akguzel, U. (2011). Performance-Based Seismic Retrofit of Existing Reinforced Concrete Frame Buildings using Fibre-Reinforced Polymers: Challenges and Solutions. *Structural Engineering International*, *21*(3), 260–270. https://doi.org/10.2749/101686611X13049248220041

Paret, T., Sasaki, K., Eilbeck, D., & Freeman, S. (1996). Approximate inelastic procedures to identify failure mechanisms from higher mode effects. *Proceedings of Eleven World Conference on Earthquake Engineering*. Eleven World Conference on Earthquake Engineering.

Pertold, J., Xiao, R. Y., & Wald, F. (2000). Embedded steel column bases. *Journal of Constructional Steel Research*, *56*(3), 253–270. https://doi.org/10.1016/S0143-974X(99)00105-4

Piana, I., & F. G. Calenzani, A. (2018). Study of design methodologies of steel column bases. *Ibracon Structures and materials journal*, *11*(7), 203–243. https://doi.org/10.1590/s1983-41952018000100011

Picard, A., & Beaulieu, D. (1985). Behaviour of a simple column base connection. *Canadian Journal of Civil Engineering*, *12*(1), 126–136. https://doi.org/10.1139/l85-013

Pujades, L. G., Barbat, A. H., González-Drigo, R., Avila, J., & Lagomarsino, S. (2012). Seismic performance of a block of buildings representative of the typical construction in the Eixample district in Barcelona (Spain). *Bulletin of Earthquake Engineering*, *10*(1), 331–349. https://doi.org/10.1007/s10518-010-9207-5

Quintana Gallo, P., Akguzel, U., Carr, A. J., & Pampanin, S. (2022). Seismic response of a non-ductile RC frame building subjected to shake-table excitations. *Bulletin of Earthquake Engineering*, *20*(1), 517–545. https://doi.org/10.1007/s10518-021-01228-4

R. Park. (1989). Evaluation of ductility of structures and structural assemblages from laboratory testing. *Bulletin of the New Zealand Society for Earthquake Engineering*, *22*(3). https://doi.org/10.5459/bnzsee.22.3.155-166

Rafaa Mahmood, A., & Akram Gulam, A. (2017). Behavior of reinforced concrete columns subjected to axial load and cyclic lateral load. *University of Baghdad Engineering Journal*, *23*(2), 21–40.

Razzaghi, J., & Khoshbakht, A. (2015). Numerical evaluation of column base rigidity. *International Journal of Steel Structures*, *15*(1), 39–49. https://doi.org/10.1007/s13296-015-3003-7

Requena-Garcia-Cruz, M. V., Morales-Esteban, A., & Durand-Neyra, P. (2022). Assessment of specific structural and ground-improvement seismic retrofitting techniques for a case study RC building by means of a multi-criteria evaluation. *Structures*, *38*, 265–278. https://doi.org/10.1016/j.istruc.2022.02.015

Ricci, P., De Luca, F., & Verderame, G. M. (2011). 6th April 2009 L'Aquila earthquake, Italy: Reinforced concrete building performance. *Bulletin of Earthquake Engineering*, *9*(1), 285–305. https://doi.org/10.1007/s10518-010-9204-8

Rodas, P. T., Zareian, F., & Kanvinde, A. (2017). Rotational stiffness of deeply embedded column–base connections. *Journal of Structural Engineering*, *143*(8), 04017064. https://doi.org/10.1061/(ASCE)ST.1943-541X.0001789

Saborio-Romano, D., O'Reilly, G. J., Welch, D. P., & Landi, L. (2018). Simplified pushover analysis of moment resisting frame structures AU - Sullivan, Timothy J. *Journal of Earthquake Engineering*, 1–28. https://doi.org/10.1080/13632469.2018.1528911

Salmon, C. G., Schenker, L., & Johnston, B. G. (1957). Moment-rotation characteristics of column anchorages. *Transactions of the American Society of Civil Engineers*, *122*(1), 132–154. https://doi.org/10.1061/TACEAT.0007496

Santos, F., & Leitão, C. (2017). Dynamic performance of a superelastic column-base connection. *Journal of Structural Control*. https://doi.org/10.1002/stc.2186

SEAOC. (1995). *VISION 2000: Performance based seismic engineering of buildings*.

Shaheen, M. A., Tsavdaridis, K. D., & Salem, E. (2017). Effect of grout properties on shear strength of column base connections: FEA and analytical approach. *Engineering Structures*, *152*, 307–319. https://doi.org/10.1016/j.engstruct.2017.08.065

Sheth, R., Prajapati, J., & Soni, D. (2018). Comparative study nonlinear static pushover analysis and displacement based adaptive pushover analysis method. *International Journal of Structural Engineering*, *9*(1), 81–90. https://doi.org/10.1504/IJSTRUCTE.2018.090753

Simple Linear Regression. (2006). In S. Chatterjee & A. S. Hadi, *Regression Analysis by Example* (pp. 21–51). John Wiley & Sons, Inc. https://doi.org/10.1002/0470055464.ch2

Singh Rawat, V. (2017, Diciembre). Increasing the strength of existing building using steel jacketing in seismic zone. *International Journal of Civil Engineering*, *4*(12). https://doi.org/10.14445/23488352/IJCE-V4I12P102

Song, B., Galasso, C., & Kanvinde, A. (2021). Reliability analysis and design considerations for exposed column base plate connections subjected to flexure and axial compression. *Journal of Structural Engineering*, *147*(2), 04020328. https://doi.org/10.1061/(ASCE)ST.1943-541X.0002903

Stamatopoulos, G. N., & Ermopoulos, J. Ch. (1997). Interaction curves for column base-plate connections. *Structural Steel Research in Greece*, *44*(1), 69–89. https://doi.org/10.1016/S0143-974X(97)00038-2

Stamatopoulos, G. N., & Ermopoulos, J. Ch. (2011). Experimental and analytical investigation of steel column bases. *Journal of Constructional Steel Research*, *67*(9), 1341–1357. https://doi.org/10.1016/j.jcsr.2011.03.007

Standards New Zealand (SNZ). (1995). *Concrete structure standard-the design of concrete structures (NZS 3101:Part 1:1995)* (NZS 3101:Part 1:1995). SNZ.

Standards New Zealand (SNZ). (2006). *Concrete structure standard-the design of concrete structures incorporating amendment No. 1 & 2 (NZS 3101:Part 1:2006- A1&A2)* (NZS 3101:Part 1:2006-A1 & A2). SNZ.

Su, R. K. L., & Wong, S. M. (2007). Seismic behaviour of slender reinforced concrete shear walls under high axial load ratio. *Engineering Structures*, *29*(8), 1957–1965. https://doi.org/10.1016/j.engstruct.2006.10.020

Sun, H., Burton, H. V., & Huang, H. (2021). Machine learning applications for building structural design and performance assessment: State-of-the-art review. *Journal of Building Engineering*, *33*, 101816. https://doi.org/10.1016/j.jobe.2020.101816

Takamatsu, T., & Tamai, H. (2005). Non-slip-type restoring force characteristics of an exposed-type column base. *Journal of Constructional Steel Research*, *61*(7), 942–961. https://doi.org/10.1016/j.jcsr.2005.01.003

Targowski, R., Lamblin, D., & Guerlement, G. (1993). Baseplate column connection under bending: Experimental and numerical study. *Journal of Constructional Steel Research*, *27*(1–3), 37–54. https://doi.org/10.1016/0143-974X(93)90005-D

Tena-Colunga, A., Godínez-Domínguez, E. A., & Hernández-Ramírez, H. (2022). Seismic retrofit and strengthening of buildings. Observations from the 2017 Puebla-Morelos earthquake in Mexico City. *Journal of Building Engineering*, *47*, 103916. https://doi.org/10.1016/j.jobe.2021.103916

Thambiratnam, D. P., & Paramasivam, P. (1986). Base plates under axial loads and moments. *Journal of Structural Engineering*, *112*(5), 1166–1181. https://doi.org/10.1061/(ASCE)0733-9445(1986)112:5(1166)

Torabi, A., & Maheri, M. R. (2017). Seismic repair and retrofit of RC beam–column joints using stiffened steel plates. *Iranian Journal of Science and Technology, Transactions of Civil Engineering*, *41*(1), 13–26. https://doi.org/10.1007/s40996-016-0027-y

Torres Rodas, P., Farzin, Z., & Amit, K. (2016). Hysteretic model for exposed column–base connections. *Journal of Structural Engineering*, *142*(12), 04016137. https://doi.org/10.1061/(ASCE)ST.1943-541X.0001602

Torres-Rodas, P., Medalla, M., Zareian, F., & Lopez-Garcia, D. (2022). Cyclic behavior and design methodology of exposed base plates with extended anchor bolts. *Engineering Structures*, *260*, 114235. https://doi.org/10.1016/j.engstruct.2022.114235

Trautner, C. A., Hutchinson, T., Grosser, P. R., & Silva, J. F. (2016). Effects of detailing on the cyclic behavior of steel baseplate connections designed to promote anchor yielding. *Journal of Structural Engineering*, *142*(2), 04015117. https://doi.org/10.1061/(ASCE)ST.1943-541X.0001361

Trautner, C. A., Hutchinson, T., Grosser, P. R., & Silva, J. F. (2017). Investigation of steel column–baseplate connection details incorporating ductile anchors. *Journal of Structural Engineering*, *143*(8), 04017074. https://doi.org/10.1061/(ASCE)ST.1943-541X.0001759

Tsavdaridis, K., Shaheen, M., Baniotopoulos, C., & Salem, E. (2015). Analytical Approach of Anchor Rod Stiffness and Steel Base-Plate Calculation under Tension. *Structures*, *5*, 207–218. https://doi.org/10.1016/j.istruc.2015.11.001

Tsompanakis, Y. (2021). Earthquake return period and Its incorporation into seismic actions. In M. Beer, I. A. Kougioumtzoglou, E. Patelli, & I. S.-K. Au (Eds.), *Encyclopedia of Earthquake Engineering* (pp. 1–35). Springer Berlin Heidelberg. https://doi.org/10.1007/978-3-642-36197-5_116-1

Villar-Salinas, S., Guzmán, A., & Carrillo, J. (2021). Performance evaluation of structures with reinforced concrete columns retrofitted with steel jacketing. *Journal of Building Engineering*, *33*, 101510. https://doi.org/10.1016/j.jobe.2020.101510

Villar-Salinas, S., Pacheco, S., Carrillo, J., & López-Almansa, F. (2023). Analysis of the influence of high axial compression ratio in RC columns on the structural response of MRF buildings. *Under Review*.

Wakjira, T. G., Abushanab, A., Ebead, U., & Alnahhal, W. (2022). FAI: Fast, accurate, and intelligent approach and prediction tool for flexural capacity of FRP-RC beams based on super-learner machine learning model. *Materials Today Communications*, *33*, 104461. https://doi.org/10.1016/j.mtcomm.2022.104461

Wald, F., Simek, I., Sokol, Z., & Seifer, J. (1994). The column-base stiffness tests, v semi-rigid behaviour of civil engineering structural connections. *Proceedings of the Second State of the Art Workshop*, 273–282.

Wang, X.-T., Xie, C.-D., Lin, L.-H., & Li, J. (2019). Seismic behavior of self-centering concrete-filled square steel tubular (CFST) Column Base. *Journal of Constructional Steel Research*, *156*, 75–85. https://doi.org/10.1016/j.jcsr.2019.01.025

Wheeler, A. T., Clarke, M. J., Hancock, G. J., & Murray, T. M. (1998). Design model for bolted moment end plate connections joining rectangular hollow sections. *Journal of Structural*

Engineering, *124*(2), 164–173. https://doi.org/10.1061/(ASCE)0733-9445(1998)124:2(164)

Willam, K. J., Citto, C., & Shing, P. B. (2010). Recent results on masonry infill walls. *Advanced Materials Research*, *133–134*, 27–30. https://doi.org/10.4028/www.scientific.net/AMR.133-134.27

Yang, Y., Hao, N., Xue, Y., Feng, S., Yu, Y., & Zhang, S. (2022). Seismic performance of RC columns retrofitted using high-strength steel strips under high axial compression ratios. *Structural Engineering and Mechanics*, *84*(3), 345–360. https://doi.org/10.12989/SEM.2022.84.3.345

Yao, D., Ma, Y., & Jia, J. (2019). The Influence of Axial Compression Ratio on Seismic Behavior of SRUHSC Frame under Cyclic Loading. *KSCE Journal of Civil Engineering*, *23*(2), 587–596. https://doi.org/10.1007/s12205-018-0235-z

Yeow, T. Z., Orumiyehei, A., Sullivan, T. J., MacRae, G. A., Clifton, G. C., & Elwood, K. J. (2018). Seismic performance of steel friction connections considering direct-repair costs. *Bulletin of Earthquake Engineering*, *16*(12), 5963–5993. https://doi.org/10.1007/s10518-018-0421-x

You, Y.-C., & Lee, D. (2020). Development of improved exposed column-base plate strong-axis joints of low-rise steel buildings. *Journal of Constructional Steel Research*, *169*, 106062. https://doi.org/10.1016/j.jcsr.2020.106062

Yu, Q.-S. "Kent," Pugliesi, R., Allen, M., & Bischoff, C. (2004). Assessment of modal pushover analysis procedure and its application to seismic evaluation of existing buildings. *13th World Conference on Earthquake Engineering*, *13th*, Paper No. 1104.

Yuen, T. Y. P., Kuang, J. S., & Ho, D. Y. B. (2016). Ductility design of RC columns. Part 1: Consideration of axial compression ratio. *HKIE Transactions*, *23*(4), 230–244. https://doi.org/10.1080/1023697X.2016.1232179

Zareian, F., & Kanvinde, A. (2013). Effect of column-base flexibility on the seismic response and safety of steel moment-resisting frames. *Earthquake Spectra*, *29*(4), 1537–1559. https://doi.org/10.1193/030512EQS062M

Zhou, F., Suita, K., Matsumiya, T., & Kurata, M. (2004). Tests on Steel Column Bases with T-Stub Connections. *Journal of Structural and Construction Engineering (Transactions of AIJ)*, *69*(581), 117–125. https://doi.org/DOI: 10.3130/aijs.69.117_2

Appendix A PUBLICATIONS GENERATED DURING THIS RESEARCH

This appendix lists the main publications generated during this research.

Publications in Journals indexed by the Journal of Citation Reports (Web of Knowledge, former ISI):

- **S. Villar-Salinas, A. Kanvinde, F. López Almansa**, "*Estimation of model parameters simulation of exposed column base plates*", Journal of Constructional Steel Research (2023) (Under review).

- **S. Villar-Salinas**, **S. Pacheco, J. Carrillo, F. López Almansa**, "*Influence of High Axial Compression Ratios in RC Columns on the Seismic Response of MRF Buildings*", Structural Engineering and Dynamics (2023) (Under the second review).

- **S. Villar-Salinas**, **B. Zuñiga Jurado, C. Graciano, F. López Almansa**, "*Numerical analysis of M-P interaction in exposed column-base plates*", Steel and Composite Structures (2023) (Under the second review).

Other relevant Publications (published during this research, but generated before):

- **S. Villar-Salinas**, **A. Guzmán**, **J. Carrillo**, "*Performance evaluation of structures with reinforced concrete columns retrofitted with steel jacketing*". Journal of Building Engineering (2021) (Published). https://doi.org/10.1016/j.jobe.2020.101510

- **S. Villar-Salinas**, **S. Pacheco**, **A. Guzmán**, **J. Carrillo**. Evaluación del desempeño sísmico de edificios de pórticos en concreto reforzado con columnas que exceden el estado límite de resistencia ante cargas verticales (2020). *XXXV Congreso Nacional de Ingeniería, Sociedad Colombiana de Ingeniería, Cartagena, Colombia*.